

**POLYMER ASSISTED FABRICATION OF NANOPARTICLES ON  
ELECTROSPUN NANOFIBERS**

by  
**BURAK BİRKAN**

**Submitted to the Graduate School of Engineering and Natural Sciences**

**in partial fulfillment**

**of the requirements for the degree of**

**Doctor of Philosophy**

**Sabanci University**

**August 2009**

**POLYMER ASSISTED FABRICATION OF NANOPARTICLES ON  
ELECTROSPUN NANOFIBERS**

APPROVED BY

Prof. Dr. Yusuf Z. Mencelođlu .....

(Thesis Supervisor)

Prof. Dr. Metin H. Acar .....

Assoc. Prof. Dr. Mehmet Ali Glgn .....

Asst. Prof. Dr. Alpay Taralp .....

Asst. Prof. Dr. Bur Mısırlıođlu .....

DATE OF APPROVAL: 11/08/09

©2009 by **BURAK BIRKAN**

ALL RIGHTS RESERVED

# **POLYMER ASSISTED FABRICATION OF NANOPARTICLES ON ELECTROSPUN NANOFIBERS**

**BURAK BİRKAN**

**Materials Science and Engineering, Ph.D. Thesis, 2009**

**Thesis Advisor: Prof. Yusuf Z. Menceloğlu**

**Key words: Nanoparticle, Electrospinning, Nanofiber, Size Control**

## **ABSTRACT**

The viability of nanotechnology strongly depends on its ability to synthesize nanometer-sized building blocks and to position them precisely at a predefined location. In this study, the aim is to control the size and distribution of nanoparticles by polymer assisted fabrication through electrospun nanofibers. Electrospun polymeric nanofibers were chosen as template materials to tune the synthesis of nanoparticles. Synthesis of different polymer structures of block and random copolymers showed that the electrostatic interactions are one of the key parameters for size control. Electrospinning parameters were examined in detail and different reduction agents and heat treatments were applied to investigate the effect of processing conditions on nanoparticle generations. By selectively changing the process conditions, nanoparticles on the order of 2-5 nm at 600°C to 10-17 nm at 1000°C could be generated. The catalytic activities of metal nanoparticles on carbon nanofibers showed an electroactive active surface area of 34.6 m<sup>2</sup>/g for Pt and 22.4 m<sup>2</sup>/g for Pd. These results confirmed the feasibility of the use of metalized nanoparticles on carbonized nanofibers as catalysts for fuel cell applications.

# NANOPARÇACIKLARIN ELEKTRODOKUMA NANO-LİFLER ÜZERİNDE POLİMER DESTEKLİ ÜRETİMİ

**BURAK BİRKAN**

**Malzeme Bilimi ve Mühendisliği, Doktora Tezi, 2009**

**Tez Danışmanı: Prof. Dr. Yusuf Z. Menceloğlu**

**Anahtar kelimeler: Nanoparçacık, Electrodokuma, Nanolif, Boyut Kontrolü**

## ÖZET

Nanoteknolojinin uygulanabilirliği, nanometre boyutundaki yapıların sentezlenebilirliği ve bunların önceden tanımlanmış yerlere doğru olarak yerleştirilebilmesine bağlıdır. Bu çalışmada amaç, elektrodokuma nano-lifler üzerinde polimer destekli olarak üretilen nanoparçacıkların boyut ve dağılımlarını kontrol etmektir. Nanoparçacıkların sentezini düzenlemek için elektrodokuma polimerik nano-lifler kalıp malzemesi olarak kullanılmıştır. Bloksal ve rastgele yapıda sentezlenmiş olan kopolimer yapılar, elektrostatik etkileşimlerin boyut kontrolündeki önemli değişkenlerden biri olduğunu göstermiştir. Elektrodokuma süreç değişkenleri detaylı olarak incelenirken, farklı indirgenler ve ısıl muameleyle süreç değişkenlerinin nanoparçacık üretim metodu üzerindeki etkisi incelenmiştir. Süreç koşullarının seçici olarak belirlenmesiyle, 600°C'de 2-5 nm'den, 1000°C'de 10-17 nm'ye kadar farklı boyutta nanoparçacıklar üretilmiştir. Karbon nanolifler üzerinde üretilmiş olan metal nanoparçacıklar Pt için 34,6 m<sup>2</sup>/g ve Pd için 22,4 m<sup>2</sup>/g elektroaktif katalitik aktivite göstermiştir. Bu sonuçlar karbonize nanolifler üzerinde sentezlenmiş olan metal nanoparçacıkların yakıt pili uygulamalarında kullanabileceğini göstermiştir.

TO MY WIFE, TUĞBA  
MY DOUGHTER, ASLI CEREN  
& ALL MY BELOVED ONES

## ACKNOWLEDGEMENT

I would like to express my deepest gratitude to my thesis supervisor Prof. Dr. Yusuf Z. Mencelođlu. His endless patience, encouragement and support during the last seven years put this thesis into a reality. He has been an example to me of an excellent scientist, a perfect advisor, the hardest worker of a family, a father. I learned from him that no any obstacle should stop me on the way of my goals. I will never forget his invaluable guidance on my researches, on my job and at home, by my family.

Assoc. Prof. Dr. Mehmet Ali Glgn was the person who taught me that the discipline, orientation and willpower should be the three most important skills that every scientist must possess on the first moment.

Asst. Prof. Dr. Alpay Taralp showed me that not every crazy idea was actually creative, but every good scientist should think sometimes outside the box, if he wants to reach the reality.

Prof. Dr. Metin H. Acar taught me that the polymer synthesis and food cooking were extremely similar but also way apart things from each other. The enjoyable part of polymer science might lie on the characterization, but the important thing is how you ‘‘cook’’ it.

I would like to thank Asst. Prof. Dr. Bur Mısırlıođlu and all my other jury members for giving their valuable time and suggestions for the improvement on the context of this thesis.

I would like to express my gratitude to Sabancı University and all the faculty members. It was a privilege of being a researcher here with all these distinguished people and excellent academic environment. The financial support of this thesis was granted by TUBITAK-MAG (Project code: 103M059).

There are many friends of mine to thank on the way of the start till the end, all whom helped me on my years at Sabancı. Dr. Kazım Acatay was the person who shared his deep knowledge with me on laboratory skills. Besides every other members of the faculty he had been a second teacher to me. Albert and Cenk were the two partners who sweat with me on the table on the lab part of this thesis. zge was the light of our days

who cherish the boring atmosphere of our lab. I also would like to thank to all my friends, Haluk, Çınar, Mustafa, Eren, Deniz, Sinan, Kerem, İbrahim, Irmak, Burcu Saner, Aslı, Özlem and Şebnem from ITU, for helping me and all the fun we had. There are many other friends I cannot remember by now. I think I had been acknowledged by many of them on their thesis work, since I have been always trying to teach them what I have in my hand. But as I look behind, actually they were the people who made the person who I am today. So it was a cooperative process of learning.

DemirDöküm A.Ş family should also be acknowledged for their helps during the last 2 years of my professional life. It was my other school of learning to put through what I have learned so far. Sait Korkmaz, Technical Assistant General Manager of DemirDöküm and Dr. Metin Kaya, my supervisor, always showed their confidence on me and encouraged me also in my academic life. Our R&D team members, Sinan and Osman, Özgür and Bervan shared the burden of the work with me.

Bülent Köroğlu, my friend, he had been one of my family on my days in Sabancı. Whenever I needed him, he was just there to help me. He is the person I can always trust blindly.

And the other parts of my life, my wife Tuğba, my daughter Aslı Ceren and my family. Your support and endless love gave me the power to stand on my feet. Lastly, my father, as time goes by, now I started to understand you better. Growing is a different thing, but being a father is the hardest things of all.

## TABLE OF CONTENTS

1	INTRODUCTION.....	1
1.1	Nanotechnology .....	2
1.1.1	Definition of Nanotechnology .....	2
1.1.2	Classification of Nanomaterials .....	3
1.1.3	Properties of Nanomaterials .....	4
1.1.4	Applications of Nanotechnology .....	5
1.1.5	Nanoparticle Production Methods .....	6
1.1.5.1	Top-down approaches .....	7
1.1.5.2	Bottom-up approaches .....	7
1.1.6	Stabilization of nanoparticles .....	7
1.2	Solution Polymerization .....	10
1.3	Copolymerization .....	12
1.4	Electrospinning .....	14
1.4.1	Fundamental Aspects of Electrospinning .....	15
1.4.2	Parameters of the Electrospinning Process .....	16
1.4.2.1	Polymer Solution Parameters .....	16
1.4.2.1.1	Polymer-solvent relationship: .....	17
1.4.2.1.2	Viscosity .....	18
1.4.2.1.3	Surface tension.....	19
1.4.2.2	Processing Conditions .....	20
1.4.2.2.1	Voltage: .....	20

1.4.2.2.2	Capillary tip to collector distance .....	20
1.4.2.2.3	Polymer flow rate .....	21
1.4.2.2.4	Temperature .....	21
1.4.3	Applications of Electrospinning .....	22
1.4.4	Literature review of electrospun metal-polymer nanocomposites .....	24
1.5	Use of metal nanoparticles/CNF for Fuel Cell application .....	30
1.6	Motivation .....	32
2	EXPERIMENTAL .....	33
2.1	Materials .....	33
2.2	Polymer Synthesis .....	34
2.3	Polymer Characterization .....	36
2.3.1	Fourier Transform Infrared Spectroscopy (FT-IR) .....	36
2.3.2	Nuclear Magnetic Resonance .....	36
2.3.3	Differential Scanning Calorimetry (DSC) .....	36
2.3.4	Thermogravimetric Analysis .....	37
2.4	Electrospinning .....	37
2.5	Reduction of metal salt .....	38
2.6	Carbonization Cycle .....	39
2.7	Nanoparticle Characterization .....	40
2.7.1	X-ray Diffraction (XRD) .....	40
2.7.2	Optical Characterization .....	41
2.7.2.1	Optical microscopy .....	41

2.7.2.2	Scanning Electron Microscopy (SEM) and Energy Dispersive X-ray Spectroscopy (EDXS) .....	41
2.7.2.3	Transmission Electron Microscopy (TEM) .....	42
3	RESULTS & DISCUSSION.....	43
3.1	Poly(acrylonitrile-co-acrylic acid), P(AN-co-AA) .....	44
3.1.1	Polymer Characterization .....	44
3.1.1.1	FT-IR characterization .....	45
3.1.1.2	NMR characterization .....	46
3.1.1.3	Thermal characterization .....	46
3.1.2	Electrospinning characterization .....	48
3.2	Poly(acrylonitrile-co-vinyl phosphonic acid), P(AN-co-VPA) .....	50
3.2.1	Polymer Characterization .....	50
3.2.1.1	FT-IR characterization .....	50
3.2.1.2	NMR characterization .....	52
3.2.1.3	Thermal characterization .....	53
3.2.2	Electrospinning characterization .....	54
3.3	Poly(acrylonitrile-co-2-acrylamido-2-methylpropane sulfonic acid), P(AN-co-AMPS) .....	57
3.3.1	Polymer Characterization .....	57
3.3.1.1	FT-IR characterization .....	57
3.3.1.2	NMR characterization .....	59
3.3.1.3	Thermal Characterization .....	60
3.3.2	Electrospinning characterization .....	61
3.4	Poly(acrylonitrile-co-n-vinyl pyrrolidinone), P(AN-co-VPYR) .....	67

3.4.1	Polymer Characterization .....	68
3.4.1.1	FT-IR characterization .....	68
3.4.1.2	NMR characterization .....	70
3.4.1.3	Thermal Characterization .....	71
3.4.2	Electrospinning .....	75
3.4.3	Reduction of metal salts .....	78
3.4.4	Nanoparticle characterization .....	79
3.4.5	Proof of concept: Catalyst nanoparticles for Fuel Cell Applications .....	92
3.4.5.1	Electrochemical Analysis of Pt including fibers .....	92
3.4.5.2	Electrochemical Analysis of Pd including fibers .....	96
4	CONCLUSION and FUTURE WORK .....	100
5	FUTURE PLANS and SUGGESTED ACTIONS .....	102
6	REFERENCES .....	103

## LIST OF FIGURES

Figure 1.4-1 Schematic of an electrospinning setup.....	15
Figure 1.4-2. TEM images of and thermally treated carbon nanofibers at 300°C.....	27
Figure 1.4-3. TEM images of Pd-NP/CENFs.....	28
Figure 1.4-4. TEM pictures of Pd nanoparticles.....	28
Figure 1.4-5. TEM images of Pd nanoparticles of varying size in/on the carbonized electrospun nanofibers with the process temperature: (A) 400°C, (B) 600 °C, (C) 800 °C and (D) 1100 °C .....	29
Figure 1.4-6 TEM image of Pd/CNF nanocomposites .....	30
Figure 2.2-1. Synthesized polymers chemical structures .....	35
Figure 2.5-1. Reduction reaction: The change of the color of polymeric fiber mat and evolution of N <sub>2</sub> (g), before and after.....	38
Figure 2.6-1. Heat treatment cycle, 40K/min heating rate for carbonization cycle.....	39
Figure 3.1-1 FT-IR spectrum of P(AN-co-10%AA) and P(AN-co-10%AA)-5%Pd.....	45
Figure 3.1-2. <sup>1</sup> H NMR spectrums of P(AN-co-AA) at different AA concentrations from 5%, 10% and 20% from top to bottom respectively .....	46
Figure 3.1-3 DSC analysis of P(AN-co-AA) at different AA concentrations.....	47
Figure 3.1-4 TGA analysis of P(AN-co-AA) at different AA concentrations.....	47
Figure 3.1-5. SEM pictures for P(AN-co-5%AA) at different Pd loadings a)0.5% b)1% c)5% respectively.....	49
Figure 3.1-6. SEM pictures for P(AN-co-AA)-5%Pd at different AA concentrations a)10%, b)20% respectively .....	49
Figure 3.2-1. FT-IR spectrum of P(AN-co-5%VPA) electrospun fibers at different Pd metal content, 0.5%, 1% and 5% from top to bottom.....	51

Figure 3.2-2 <sup>1</sup> H NMR spectrums of P(AN-co-VPA) at different VPA concentrations from 5%, 10% and 20% from top to bottom respectively .....	52
Figure 3.2-3 DSC analysis of P(AN-co-VPA) at different VPA concentrations from 5%, 10% and 20% from top to bottom respectively. ....	53
Figure 3.2-4 STA analysis of P(AN-co-VPA), 5%, 10% and 20% respectively.....	54
Figure 3.2-5. SEM pictures for P(AN-co-5%VPA) at different Pd loadings a)0.5% b)1% c)5%.....	55
Figure 3.2-6 SEM pictures for P(AN-co-VPA)-5%Pd at different VPA concentrations a)5% b)10% and c)20% respectively.....	56
Figure 3.2-7. SEM pictures for P(AN-co-5%VPA) fibers before and after heat treatment at 200°C.....	56
Figure 3.3-1 FT-IR spectrum of P(AN-co-AMPS) electrospun fibers at different Pd metal content, 0,5%, 1% and 5% from top to bottom.....	58
Figure 3.3-2 <sup>1</sup> H NMR spectrums of P(AN-co-AMPS) at different AMPS concentrations from 5%, 10% and 20% from top to bottom respectively .....	59
Figure 3.3-3 DSC analysis of P(AN-co-AMPS) at different AMPS concentrations.....	60
Figure 3.3-4 TGA analysis of P(AN-co-AMPS) at different AMPS concentrations from 5%, 10% and 20% from top to bottom respectively .....	61
Figure 3.3-5 SEM pictures for P(AN-co-5%AMPS) at different Pd loadings a)0.5% b)1% c)5% .....	62
Figure 3.3-6 SEM pictures Electrospun P(AN-co-5%AMPS)-5%Pd, reduced nanoparticles .....	63
Figure 3.3-7 TEM pictures of P(AN-co-5%AMPS) at different Pd loadings a)0.5% b)1% c)5% .....	64
Figure 3.3-8 SEM pictures for Carbonized P(AN-co-5%AMPS)-5%Pd electrospun fibers at 600°C, different magnifications.....	65

Figure 3.4-1. FT-IR spectrums of P(AN-co-10%VPYR)-5%Pd, before and after reduction of PdCl <sub>2</sub> .....	69
Figure 3.4-2 FT-IR spectrums of P(AN-co-10%VPYR)-Pt, increasing Pt concentration .....	69
Figure 3.4-3. <sup>1</sup> H NMR spectrums of P(AN-co-VPYR) at different VPYR concentrations from 5%, 10% and 20% from top to bottom respectively .....	70
Figure 3.4-4 DSC analysis of P(AN-co-VPYR) at different VPYR concentrations .....	71
Figure 3.4-5. TGA analysis of P(AN-co-VPYR) at different VPYR concentrations from 5%, 10% and 20% from top to bottom respectively .....	73
Figure 3.4-6. Diagram of the molecular changes occurring during the chemical process of stabilization and carbonization of PAN.....	74
Figure 3.4-7. SEM pictures for P(AN-co-5%VPYR), different solution concentrations, 20%, 15% and 12% respectively. ....	77
Figure 3.4-8 XRD analysis for P(AN-co-5%VPYR)-5%Pd, different reducing agents. 78	
Figure 3.4-9. Two conceptual models for crystallite growth due to sintering by A) atomic migration or B) crystallite migration .....	80
Figure 3.4-10 P(AN-co-5%VPYR)-5%Pd-heating treatment effects-TEM analyses a) 600°C-0,1°C/min-30min (5.1 nm average particle size) b) 600°C -1°C /min-30min (4.8 nm average particle size) c) 600°C -1°C /min (4.7 nm average particle size).....	81
Figure 3.4-11. SEM pictures of P(AN-co-5%VPYR)-5%Pd, carbonized at a)600°C -1°C /min b) 600°C -1°C /min-30min .....	81
Figure 3.4-12 SEM pictures of P(AN-co-5%VPYR)-5%Pd, carbonized at a) 600°C -5°C /min b)1200°C -1°C /min c) 1200°C -1°C /min-30min d) 1200°C -10°C /min .....	82
Figure 3.4-13 XRD spectrum of P(AN-co-VPYR)-5%Pt, different Pd content.....	85
Figure 3.4-14 XRD spectrum of P(AN-co-20%VPYR)-20%Pd-effect of different carbonization cycles on crystalline size.....	86

Figure 3.4-15 XRD spectrum of P(AN-co-10%VPYR)-20%Pt-effect of different carbonization cycles on crystalline size.....	86
Figure 3.4-16 A schematic of nanoparticle synthesis on random and blocky copolymers .....	88
Figure 3.4-17 <sup>13</sup> C-NMR spectrums of P(AN-co-5%VPYR), copolymer, after e-spinning and carbonization at 600°C and 1000°C .....	89
Figure 3.4-18. Cyclic voltammogram of P(AN-co-5%VPYR)-10%Pt-1000°C-40°C....	93
Figure 3.4-19 Cyclic voltammogram of P(AN-co-5%VPYR)-20%Pt-600°C-5°C.....	95
Figure 3.4-20. Cyclic voltammogram of P(AN-co-5%VPYR)-5%Pd-1200°C-5°C.....	97
Figure 3.4-21 Cyclic voltammogram of P(AN-co-5%VPYR), different Pd% concentration.....	98
Figure 3.4-22 Cyclic voltammogram of P(AN-co-5%VPYR)-5%Pd, different heating rates.....	99

## LIST OF TABLES

Table 1.1-1. Classification of nanomaterials with regard to different materials .....	3
Table 1.1-2. Adjustable properties of nanomaterials.....	4
Table 1.1-3. Nanotechnology-Innovative products in materials.....	6
Table 1.2-1 Typical Solution polymerization processes.....	12
Table 1.4-1: Summary of polymers and solvents used to produce electrospun fibers in the solution form.....	17
Table 1.4-2 Summary of polymers electrospun in the melt form.....	18
Table 1.4-3. Foresights on the broad applications of electrospinning .....	22
Table 1.4-4. Electrospun metal composite nanofibers and usage areas.....	26
Table 2.4-1. Summary of the electrospinning working condition .....	37
Table 3.1-1. Synthesis of Poly(AN-co-AA) .....	44
Table 3.1-2. Electrospun P(AN-co-AA) polymer fiber diameter. ....	48
Table 3.2-1 Synthesis of Poly(AN-co-VPA) .....	50
Table 3.2-2 Electrospun P(AN-co-VPA) polymer fiber diameter.....	54
Table 3.3-1 Synthesis of Poly(AN-co-AMPS) .....	57
Table 3.3-2 Electrospun P(AN-co-AMPS) polymer fiber diameter. ....	61
Table 3.4-1 Synthesis of Poly(AN-co-AMPS) .....	68
Table 3.4-2 Glass transition temperature analyses for VPYR copolymers .....	72
Table 3.4-3 Electrospun P(AN-co-VPYR) polymer fiber diameter. ....	76
Table 3.4-4. XRD spectrum analyses for different reducing agents.....	79
Table 3.4-5 Heat treatment effect on particle size for P(AN-co-5-VPYR), 5%Pd .....	79

Table 3.4-6. SEM analysis results for P(AN-co-VPYR) electrospun nanoparticles .....	83
Table 3.4-7 XRD analysis results for heat treated VPYR copolymer .....	84
Table 3.4-8 Literature examples for supported metal nanoparticles .....	91
Table 3.4-9 Summary of electrochemical results for Pt including fibers .....	95
Table 3.4-10 Summary of electrochemical results for Pd including fibers .....	99

## LIST OF ABBREVIATIONS

AA	Acrylic acid
AIBN	2,2'-azo-bis(isobutyronitrile)
AMPS	2-2-acrylamido-2-methylpropane sulfonic acid
AN	Acrylonitrile
CA	Cellulose acetate
CNF	Carbon nanofiber
CNT	Carbon nanotube
CVD	Chemical Vapor Deposition
DMF	Dimethylformamide
DSC	Differential Scanning Calorimetry
FT-IR	Fourier Transform Infrared
NP	Nanoparticle
PAN	Polyacrylonitrile
PVA	poly(vinyl alcohol)
PVP	poly(vinyl pyrrolidinone)
SCE	Standard Calomel Electrode
SEM	Scanning Electron Microscope
TGA	Thermogravimetric Analysis
TEM	Tunneling Electron Microscope
VPA	Vinyl phosphonic acid
VPYR	vinyl pyrrolidinone

## **CHAPTER 1**

### **1 INTRODUCTION**

The viability of nanotechnology strongly depends on its ability to synthesize nanometer-sized building blocks and to position them precisely at a predefined location. Up to now, various attempts to prepare metal nanoparticles on carbon-based materials have been reported in reference to their size dependent catalytic, optical, electronic and magnetic properties compared to those of bulk metals<sup>1-5</sup>. Among many types of metals, palladium and platinum nanoparticles have attracted lots of attention due to their unique catalytic activity<sup>6-9</sup> and high hydrogen sensing and storing ability<sup>10-12</sup>. Previous reports have usually generated a wide size distribution of metal particles and weak binding strength with supporting materials because metal particles were attached (or grown) on chemically active sites based on heterogeneous nucleation and growth mechanisms<sup>13, 14</sup>.

This introductory chapter will lead the reader to gather the basic knowledge starting from the aspects of nanotechnology to the methodology that will be used in the thesis. Polymerization methods and electrospinning sections will elucidate the basic key points and literature review on past studies of electrospun metal-polymer nanocomposites will detail the up to day knowledge. The motivation section will enlighten the reader for the upcoming chapters for better understanding of the unique ideology of this research.

## 1.1 Nanotechnology

### 1.1.1 Definition of Nanotechnology

*"The principles of physics, as far as I can see, do not speak against the possibility of maneuvering things atom by atom. It is not an attempt to violate any laws; it is something, in principle, that can be done; but in practice, it has not been done because we are too big".*

*Richard Feynman, Nobel Prize winner*

The idea of nanotechnology, the study of the control of matter on an atomic and molecular scale was expressed for the first time in the famous known speech of Richard Feynman at an American Physical Society meeting at Caltech on December 29, 1959<sup>15</sup>. Nearly two decades later, at 1974 at the Tokyo Science University, Professor Norio Taniguchi came up with the term nanotechnology<sup>16</sup>. When K. Eric Drexler popularized the word 'nanotechnology' in the 1980's, he was talking specifically about building machines on the scale of molecules, a few nanometers wide motors, robot arms, and even whole computers, far smaller than a cell<sup>17</sup>. As nanotechnology became an accepted concept, the meaning of the word shifted to encompass the simpler kinds of nanometer-scale technology. The U.S. National Nanotechnology Initiative (NNI) was created to fund this kind of nanotech: their definition includes anything smaller than 100 nanometers with novel properties. NNI says that nanotechnology must involve all of the following:

1. Research and technology development at the atomic, molecular or macromolecular levels, in the length scale of approximately 1 to 100 nm range
2. Creation and use of structures, devices, and systems that have novel properties and functions because of their small and/or intermediate size
3. Ability to control or manipulate on the atomic scale.

### 1.1.2 Classification of Nanomaterials

All conventional materials such as metals, semiconductors, glass, ceramic or polymers can in principle be obtained with a nanoscale dimension. The spectrum of nanomaterials ranges from inorganic or organic, crystalline or amorphous particles, which can be found as single particles, aggregates, powders or dispersed in a matrix, over colloids, suspensions and emulsions, nanolayers and films, up to the class of fullerenes and their derivatives. Also supramolecular structures such as dendrimers, micelles or liposomes belong to the field of nanomaterials. Generally there are different approaches for a classification of nanomaterials, some of which are summarized in Table 1.1-1.

CLASSIFICATION	EXAMPLES
Dimension <ul style="list-style-type: none"> <li>• 3 dimensions &lt;100 nm</li> <li>• 2 dimensions &lt;100 nm</li> <li>• 1 dimension &lt;100 nm</li> </ul>	Particles, quantum dots, hollow spheres Tubes, filters, wires, platelets Films, coatings, multilayer
Phase composition <ul style="list-style-type: none"> <li>• Single-phase solids</li> <li>• Multi-phase solids</li> <li>• Multi-phase systems</li> </ul>	Crystalline, amorphous particles and layers Matrix composites, coated particles Colloids, aerogels, ferrofluids
Manufacturing process <ul style="list-style-type: none"> <li>• Gas phase reaction</li> <li>• Liquid phase reaction</li> <li>• Mechanical procedures</li> </ul>	Flame synthesis, condensation, CVD Sol-gel, precipitation, hydrothermal processing Ball milling, plastic deformation

Table 1.1-1. Classification of nanomaterials with regard to different materials

### 1.1.3 Properties of Nanomaterials

The physical and chemical properties of nanostructured materials (such as optical absorption and fluorescence, melting point, catalytic activity, magnetism, electric and thermal conductivity, etc) typically differ significantly from those of the properties corresponding to bulk materials. A broad range of material properties can be selectively adjusted by structuring at the nanoscale (Table 1.1-2).

Properties	Examples
Catalytic	Better catalytic efficiency through higher surface-to-volume ratio
Electrical	Increased electrical conductivity in ceramics and magnetic nanocomposites, increased electric resistance in metals
Magnetic	Increased magnetic coercivity up to a critical grain size, superparamagnetic behavior
Mechanical	Improved hardness and toughness of metals and alloys, ductility and superplasticity of ceramic
Optical	Spectral shift of optical absorption and fluorescence properties, increased quantum efficiency of semiconductor crystals
Sterical	Increased selectivity, hollow spheres for specific drug transportation and controlled release
Biological	Increased permeability through biological barriers (membranes, blood-brain barrier, etc.), improved biocompatibility

Table 1.1-2. Adjustable properties of nanomaterials

These special properties of nanomaterials are mainly due to quantum size confinement in nanoclusters and an extremely large surface-to-volume ratio to bulk materials and therefore a high percentage of atoms/molecules lying at reactive boundary surfaces. The increase in the surface to volume ratio results in the increase of particle surface energy, which leads to e.g. a decrease in melting point or an increased sintering activity. It is stated that a large specific surface area of particles may significantly raise the level of otherwise kinetically or thermodynamically unfavorable reactions<sup>18</sup>. Even

gold, which is a very stable material, becomes reactive when the particle size is small enough<sup>19</sup>.

#### **1.1.4 Applications of Nanotechnology**

Despite the term of nanotechnology is first oriented in the second half of the 1900's, the use of nanoparticles dates back to ancient times. A famous artifact from Roman Period (30BC-640AD) called Lycurgus cup resides in the British Museum at London which is made from glass and dates from the fourth century AD. What makes this cup unique is that its color changes from green to red. Transmission electron microscopy reveals that the glass contains nanoparticles of gold and silver. Surprisingly, the ruby color of some stained glass in churches build at medieval times (500-1450) is due to gold nanoparticles trapped in glass matrix, while the deep yellow color is due to silver nanoparticles. The size of metal nanoparticles produces these color variations. This example of the change in material properties at the nanoscale is a key component of nanotechnology.

The range of applications is broad and growing with the current main uses as functional additives or precursors for emulsions, composites and coatings. While still only scratching the surface of their considerable commercial potential, nanomaterials have established an appreciable market presence -- \$1 billion -- mainly in the United States, Western Europe and Japan. By 2011, world demand for nanomaterials is forecasted to reach \$4.2 billion. In the longer term, the global market is projected to swell to \$100 billion in 2025. The polymer properties that show substantial performance improvements include: mechanical properties (e.g., strength, modulus and dimensional stability), decrease in the permeability (to gases, water and hydrocarbons), thermal and UV stability and heat distortion temperature, flame retardancy and reduced smoke emissions, chemical resistance, surface appearance, electrical conductivity and optical clarity and increased resistance to solar degradation in comparison to conveniently filled polymers.

A current status overview of a selection of recent uses of nanoparticles in various industrial sectors is presented in Table 1.1-3.

<b>Industry sector</b>	<b>Features added through Nanotechnology</b>	<b>Innovative product</b>
Plastics Industry	Nano powder. Surface improvement, dispersion technology	Thermal insulation, anti-UV, antibacterial, high fade resistant materials
Man Made Fiber Industry	Nano-function formulation technology	High strength, anti-bacteria, abrasion resisting, electric conducting, low gas permeation, environmentally friendly packing materials
Coating Industry	Nano porous structure technology	Abrasion resistant, antibacterial/UV, high temperature stable, flame retarding, nano-color paste/ink, high thermal conducting material
Paper Production Industry	Self-assembly process technology	Food preservation bag, high quality printing paper, high-stiffness film
Construction Industry	Nano Interface processing technology	Self-cleaning, thermal insulation, antifog
Metal Industry	Nanocrystal lattice control technology	High strength steel aluminum alloy, abrasion resisting surface treatment
Chemical Industry	Nano-catalysts, sensor, high thermal; conducting materials, glass coating	

Table 1.1-3. Nanotechnology-Innovative products in materials

### 1.1.5 Nanoparticle Production Methods

The themes underlying nanoscience and nanotechnology are twofold: one is the top-down approach that is generation of nanoparticles from the size reduction of bulk materials, as articulated by Feynman. These approaches generally rely on physical processes, the combination of physical and chemical, electrical or thermal processes for their production. Bottom up approaches, where nanoparticles are generated from the atomic or molecular level, are predominantly chemical processes.

### **1.1.5.1 Top-down approaches**

There are a range of top-down processes that can be used to produce nanoparticles. The most significant of these physical methods are high energy milling, the combination of physical and chemical methods (chemical-mechanical milling) and vapor phase condensation (using laser ablation, electro-explosion, sputtering and vapor condensation using thermal methods).

### **1.1.5.2 Bottom-up approaches**

Bottom up processes produce nanoparticles by combination to generate material from the atomic or the molecular level. The most common are chemical vapor deposition (CVD), sol-gel, and atomic or molecular condensation. These chemical processes rely on the availability of appropriate “metal-organic” molecules as precursors.

Because sol-gel processing differs from other chemical processes due to its relatively low processing temperature, sol-gel process is cost-effective and versatile. In spraying processes, the flow of reactants (gas, liquid in form of aerosols or mixtures of both) is introduced to a high-energy flame produced for example by plasma spraying equipment or carbon dioxide laser. The reactants decompose and particles are formed in a flame by homogeneous nucleation and growth. Rapid cooling results in the formation of nanoscale particles.

### **1.1.6 Stabilization of nanoparticles**

With precise control of the size of particles, their characteristics can be controlled within certain limits. It is usually difficult to maintain the desired characteristics,

beyond the different manufacturing processes to the final product, because loose nanopowders tend to grow to larger particles already at room temperature and thus lose their nanospecific characteristics. Therefore it is necessary to select or develop suitable production processes and further refining/treatment processes to prevent or attenuate agglomeration and grain growth during generation, processing and during the use of nanomaterials.

Scientists and engineers have spent much effort to overcome these difficulties. Analysis of the results of the numerous investigations published in thousands of papers, hundreds of review articles and tens of monographs have led to the conclusion that the most efficient and universal way to overcome these problems is to use polymer-assisted fabrication of inorganic nanoparticles and hybrid polymer–inorganic nanocomposites.

Over the last two decades, polymer science has made much progress in developing novel methodologies of synthesis of a great variety of polymers with controlled macromolecular architecture and well defined morphology. Among these, first of all, it is important to note that controlled living ionic and radical polymerization and copolymerization<sup>20-23</sup> stand forward. Today it seems possible to prepare copolymers of various architectures from virtually all kinds of vinyl monomers by ionic and free-radical mechanisms by bulk, solution, suspension or emulsion processes. The ease of manipulating the fundamental characteristics of polymers (molecular weight, molecular weight distribution, chain topology, chain architecture and composition) by using different methods makes this approach attractive for nanoparticle engineering.

These developments in polymer science, together with the latest achievements of inorganic chemistry, create a base from which to address the fundamental problem of increasing the sensitivity of nanoparticles to their environment, and to work out pathways for nanoparticle synthesis with controlled size, shape and other properties, and, as a result, to elaborate new advanced areas of application.

Many different methods are used for the production of inorganic nanoparticles<sup>24-27</sup>. For further manipulations, nanoparticles, usually existing as aggregates, are dispersed in a liquid or solid medium. Different mechanochemical approaches including sonication by ultrasound can be used for this purpose. However, the scope of such approaches for dispersing the nanoparticles is limited by re-aggregation of the individual nanoparticles and the establishment of an equilibrium state under definite

conditions, which determines the size distribution of the agglomerate of dispersed nanoparticles. Other limitations are related to temperature conditions and the limited stability of some types of inorganic nanoparticles to mechanical impacts.

Particles coated by a polymer shell are considerably more stable against aggregation because of a large decrease of their surface energy in comparison with bare particles. Such a polymer shell can be obtained by first synthesizing the inorganic nanoparticles in one way or another, and then dispersing them in a polymer solution. Finally the polymer coated inorganic nanoparticles are precipitated into a non-solvating phase. This is the so-called *ex situ* approach. Such a process of polymer shell formation on preformed inorganic cores can also be realized by polymerization of the desired monomer with organic nanoparticles dispersed in it. Finally a nanocomposite material is formed. The *ex situ* approach is the most general one because there are no limitations on the kinds of nanoparticles and polymers that can be used. The presence of such a shell increases the compatibility of the particles in the polymer matrix and makes it easier to disperse them.

In some cases, the process of protective polymer coating formation and nanoparticles preparation can be combined into one process or performed as a series of consecutive processes in one reactor (the *in situ* approach). This approach can be used also for the preparation of nanocomposites. In the *in situ* methods, nanocomposites are generated inside a polymer matrix by precursors, which are transformed into the desirable nanoparticles by appropriate reactions. *In situ* approaches are currently getting much attention because of their obvious technological advantages over *ex situ* methods.

Traditionally polymer-nanocomposites have been prepared by *in situ* generation. The polymer matrix not only acts as a template for their synthesis but also imparts the necessary stability by providing a barrier against agglomeration of the metallic nanoparticles formed during and after the reduction process. A variety of different polymers (homopolymers, block copolymers and dendrimers) have been used to create ordered nanocomposites materials for various applications.

Polymers provide stabilization for metal nanoparticles through the steric bulk of their framework, but also bind weakly to the NP surface through heteroatom that play the role of ligand. Poly(ethylene oxide)<sup>28, 29</sup> and poly(vinyl pyrrolidone) (PVP)<sup>30-34</sup>

have been mostly used for nanoparticle stabilization and catalysis, because they fulfill both steric and ligand requirements.

The use of polymers to prevent particle aggregation during the reduction of the nanoparticles led Chen et al.<sup>35</sup> to use PVP as a polymer template. It is found that Pt nanoparticles mediated by PVP were smaller than those obtained without PVP and had a narrower size distribution. The catalysts prepared with PVP mediation generally showed larger active specific areas than those prepared without PVP.

Well dispersed silver nanoparticles are prepared by a chemical reduction method with PVP as a dispersing and reducing agent<sup>36</sup>. Silver particles with diameter shorter than 50 nm are protected by the coordination between silver and N in PVP, and for the bigger particles, with the diameter of 0,5-1 $\mu$  , both N and O coordinated with the silver.

Narayanan et al.<sup>37</sup> used PVP with the same proposed aim for the Suzuki reaction between phenylboronic acid and iodobenzene catalyzed by PVP-Pd nanoparticle. He stated that the addition of excess PVP stabilizer to the reaction mixture seem to lead to the stability of the nanoparticle surface and size, due to the inhibition of the Ostwald ripening process.

## **1.2 Solution Polymerization**

In solution polymerization, the monomer, the initiator, and the resulting polymer are all soluble in the solvent. Solution polymerization may involve a simple process in which a monomer, catalyst and solvent are stirred together to form a solution that reacts without the need for heating or cooling or any special handling. On the other hand, elaborate equipment may be required.

Polymerization is performed in solution either batch wise or continuously. Batch reaction takes place in a variety of ways. The batch may be mixed and held at a constant temperature while running for a given time, or for a time dictated by tests made during the progress of the run. Alternatively, termination is dictated by a predetermined decrease in pressures following monomer consumption. A continuous reaction train, on

the other hand, consists of a number of reactors, usually up to about ten, with the earlier overflowing into the next and the later ones on control level, with transfer from one to the next by pump.

As the reaction progresses, solution polymerization generally involves a pronounced increase in viscosity and evolution of heat. The viscosity increase demands higher power and stronger design for pumps and agitators. The reactor design depends largely on how the heat evolved is dissipated. A typical reactor has agitation, cooling and heating facilities, relief, temperature level, and pressure connections; and frequently, cleanout connections in addition to inlet and outlet fittings.

Solution polymerization has certain advantages over bulk, emulsion, and suspension polymerization techniques. The catalyst is not coated by polymer so that efficiency is sustained and removal of catalyst residues from the polymer, when required, is simplified. Solution polymerization is one way of reducing the heat transfer problems encountered in bulk polymerization. The solvent acts as inert diluents, increasing overall heat capacity without contributing to heat generation by conducting the polymerization at the reflux temperature of the reaction mass, the heat of polymerization can be conveniently and efficiently removed. Furthermore, relative to the bulk polymerization, mixing is facilitated because the presence of the solvent reduces the rate of increase of reaction medium viscosity as the reaction progresses.

Solution polymerization, however, has a number of drawbacks. The solubility of polymers is generally limited, particularly at higher molecular weights. Lower solubility requires that vessels be larger for a given production capacity. The use of an inert solvent not only lowers the yield per reactor volume but also reduces the reaction rate and average chain length since these quantities are proportional to monomer concentration. Another disadvantage of solution polymerization is the necessity of selecting an inert solvent to eliminate the possibility of chain transfer to the solvent. The solvent frequently presents hazards of toxicity, fire and other problems not associated with the product itself. Also, solvent handling and recovery and separation of the polymer involve additional costs, and removal of unreacted monomer can be difficult. Complete removal of the solvent is difficult in some cases. With certain monomers, solution polymerization leads to a relatively low reaction rate and low-molecular-weight polymers as compared with aqueous emulsion or suspension polymerization.

Solution polymerization has limited commercial utility in free-radical polymerization but finds ready applications when the end of the polymer requires a solution, as uncertain adhesives and coating processes. Solution polymerization is used widely in ionic and coordination polymerization. High density polyethylene, polybutadiene, and butyl rubber are produced this way. Table 1.2-1 shows the diversity of polymers produced by solution polymerization.

Monomer	Product	Solvent	Catalyst	Temperature (°F)
Conjugated diene	Synthetic rubber	Hexane, heptanes, benzene etc.	Coordination, or alkyllithium	50
Isobutylene+ isoprene	Butyl rubber	Methyl chloride	AlCl <sub>3</sub>	-140
Ethylene	Polyethylene	Ethylene	Peroxygenic	210-48
Propylene	Polypropylene	Hexane	Anionic type	-60 to 160
Vinyl acetate	Polyvinyl acetate	Alcohol, ester, or aromatic	Peroxygenic	Precipitation
Bisphenol A+ phosgene	Polycarbonate resin			To 104
Acrylamide+acrylonitrile	Resin	Water	Ammonium persulfate	165-175
Acrylate	Adhesive coating	Ethyl acrylate	Free-radical initiator	Refluxing temp.
Ethylene + propylene + diene	EPT rubber	Hydrocarbon	Coordination	100

Table 1.2-1 Typical Solution polymerization processes

### 1.3 Copolymerization

The polymerization of organic compounds was first reported about the mid-19<sup>th</sup> century. However, it was not until about 1910 that the simultaneous polymerization of two or more monomers (or copolymerization) was investigated when it was discovered that copolymers of olefins and dienes produced better elastomers than either polyolefins or polydienes alone. The pioneering work of Staudinger in the 1930s and the

development of synthetic rubber to meet wartime needs opened the field of copolymerization.

Copolymers constitute the vast majority of commercially important polymers. Compositions of copolymers may vary from only a small percentage of one component to comparable proportions of both monomers. Such a wide variation in composition permits the production of polymer products with vastly different properties for a variety of the end uses.

The general copolymerization equation is:

$$\text{Equation 1.3-1} \quad F_1 = \frac{r_1 f_1^2 + f_1 f_2}{r_1 f_1^2 + 2 f_1 f_2 + r_{21} f_2^2}$$

Where,  $r_1$  and  $r_2$  are monomer reactivity ratios and are defined by

$$\text{Equation 1.3-2} \quad r_1 = \frac{k_{11}}{k_{12}} \text{ and } r_2 = \frac{k_{22}}{k_{21}}$$

and  $F_1$  represents the mole fractions monomers  $M_1$  and  $M_2$  in the monomer feed by  $f_1$  and  $f_2$ .

By definition,  $r_1$  and  $r_2$  represent the relative preference of a given radical that is adding its own monomer to the other monomer. The physical significance Equation 1.3-1 can be illustrated by considering the product of the reactivity ratios,

$$\text{Equation 1.3-3} \quad r_1 r_2 = \frac{k_{11} k_{22}}{k_{12} k_{21}}$$

The quantity  $r_1 r_2$  represents the ratio of the product of the rate constants for the reaction of a radical with its own kind monomer to the product of the rate constants for the cross sections. Copolymerization may therefore be classified into three categories depending on whether the quantity  $r_1 r_2$  is unity, less than unity, or greater than unity.

- a)  $r_1 r_2 = 1$ ; it is the case for ideal copolymerization, where each radical displays the same preference for adding one monomer over the other. Therefore, the sequence of monomer units in an ideal copolymer is random.
- b)  $r_1 = r_2 = 0$ ; perfect alternation occurs when both  $r_1$  and  $r_2$  are zero. As the quantity  $r_1 r_2$  approaches zero, there is an increasing tendency toward alternation.

c)  $r_1 > 0$ ,  $r_2 > 0$ ; if  $r_1$  and  $r_2$  are both greater than unity, then each radical would prefer adding its own monomer. The addition of the same type of monomer would continue successfully until there is a chance addition of the other type of monomer and the sequence of this monomer is repeatedly added. Thus the resulting polymer is a block copolymer.

## 1.4 Electrospinning

As the broad field of nanotechnology gained widespread recognition in the 1990s, electrospinning has been extensively used as a powerful technique which provides a route to the creation of sub-micron to nano-scale fibers through an electrically charged jet of polymer solution/melt.

The term “electrospinning” is technically derived from “electrostatic spinning”, in which electrical charges are employed in the process to produce filaments. Although the term “electro-spinning”, was used recently in 1990s, its fundamental idea dates back more than 70 years earlier. From 1934 to 1944, Formhals<sup>38-41</sup> obtained a series of patents, for a process capable of producing micron level monofilament fibers using the electrostatic forces generated in an electrical field for a variety of polymer solutions.

In 1969, Taylor<sup>42</sup> fundamentally studied the shape of the polymer droplet at the tip of the needle and demonstrated that it is a cone and the jet is ejected from the vertex of the cone, referred as the “Taylor Cone”. Baumgarten<sup>43</sup>, in 1971, produced electrospun acrylic fibers with diameters in the range of 500-1100 nm. He reported that the diameter of fibers was dependent on the viscosity of polyacrylonitrile /dimethylformamide (PAN/DMF) solution, and the diameter of the jet became larger with increasing electric fields as well. Larrondo and Manley<sup>44-46</sup> studied the relationships between the fiber diameter and melt temperature of polyethylene (PE) and polypropylene (PP) in the melt state. They found that the diameter decreases with increasing melt temperature and showed that the fiber diameter was reduced by 50% when the applied voltage was increased two-fold.

In the early 1990s, several research groups demonstrated that many organic polymers could be electrospun into nanofibers. Since then, the number of publications about electrospinning has been increasing exponentially every year<sup>47, 48</sup>. The very basic nature of the nanofibers such as very large surface area to volume ratio, flexibility in surface functionality, and superior mechanical performance compared with any other known form of the material, excites researchers' interests.

### 1.4.1 Fundamental Aspects of Electrospinning

Electrospinning is recognized as a fast and simple process for making continuous submicron to nano size fibers, when compared with other conventional methods such as drawing, template synthesis, phase separation, and self-assembly. The drawing process requires a viscoelastic material that is suitable for high stresses and deformations during pulling into a single strand of very long nanofiber. In the template synthesis, a nanoporous metal oxide membrane is utilized as a template to make nanofibers either in tubular (hollow) or fibril (solid) form. However, this fabrication method cannot produce continuous fibers in single-strand form. The phase separation takes a long period of time to obtain the nano-porous fibers since it involves many steps like dissolution, gelation, extraction, freezing, and drying to complete the process. Similarly, the self-assembly, a technique in which pre-existing chemicals rearrange themselves into desired patterns and functions, although it is easy to obtain smaller nanofibers, the complexity of the process limits the use.

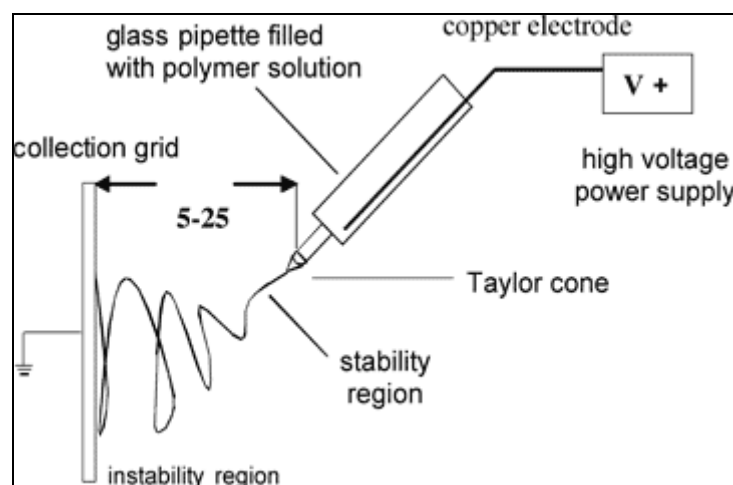


Figure 1.4-1 Schematic of an electrospinning setup, courtesy of NovaComp INC

The basic feature of an electrospinning process is depicted in Figure 1.4-1. Typically, one electrode is inserted into the polymer solution/melt and the other attached to a grounded collector. As high voltage is applied, the charge repulsion on the surface of the fluid causes a force directly opposite to the surface tension of the fluid itself. When the electric field is increased, the hemispherical surface of the fluid at the tip of the pipette deforms into the conical shape named as “Taylor cone”. When the electric field strength at the tip of this cone exceeds a critical value, a jet of fluid will erupt from the apex of the Taylor cone and proceeds to the collection plate. A whipping characteristic of the discharged polymer jet is observed during the spinning process. Solvent evaporation takes place from the charged polymer fibers on the way to the collector, leaving behind a non-woven fiber mat.

#### **1.4.2 Parameters of the Electrospinning Process**

While the electrospinning setup and process itself may be relatively simple, the variables involved in producing a nano-sized diameter, fiber mesh with relative uniformity are numerous. Mainly electrospinning depends on the complex interplay of surfaces, shapes, rheology, and electrical charge, so both solution and process parameters must be considered.

Solution parameters<sup>49, 50</sup> include choosing the best solvent for a polymer, viscosity, and conductivity. Process parameters<sup>51, 52</sup> include electric field strength, flow rate, distance from the capillary to the collector, shape and movement of the collector, room temperature, and humidity.

##### **1.4.2.1 Polymer Solution Parameters**

The properties of the polymer solution have the most significant influence in the electrospinning process and the resultant fiber morphology. The surface tension has a part to play in the formation of beads along the fiber length. The viscosity of the solution and its electrical properties will determine the extent of elongation of the

solution. This will in turn have an effect on the diameter of the resultant electrospun fibers.

#### 1.4.2.1.1 Polymer-solvent relationship:

Numerous polymers have been electrospun by an increasing number of researchers around the world. Examples of some of the polymers that have been successfully spun are shown in Table 1.4-1 and Table 1.4-2. Solvents of varying pH, polymers with molecular weights ranging from 10,000 to 300,000 and higher have been electrospun.

No	Polymer	Solvent
1	Cellulose acetate	Acetone
2	Polyacrylic acid, PAA	Ethanol
3	Polyacrylonitrile, PAN	DMF
4	Polyamide-6	85% v/v formic acid
5	Poly(benzimidazol), PBI	N,N-Dimethyl acetamide (DMAC)
6	Polycarbonate	Dichloromethane, Chloroform, DMF, THF
7	Poly( $\epsilon$ -caprolactone)	85% DMF: 15% Methylene Chloride
8	Poly(ethylene oxide), PEO	Water
9	Poly(ethylene terephthalate), PET	Trifluoroacetic acid
10	Polyether urethane	DMAc
11	Poly (2-hydroxy ethyl methacrylate)	Formic acid and ethanol
12	Poly lactic acid, PLA	Chloroform
13	Poly-L-lactide, PLLA	Dichloromethane
14	Poly (methyl methacrylate)	Toluene and DMF
15	Polystyrene, PS	Chlorobenzene, Chloroform, DMF, THF
16	Styrene-Butadiene-Styrene (SBS),	75% THF : 25% DMF
17	Polysulfone, Bisphenol A	90% DMAC : 10% acetone
18	Polyurethane, PU	DMF and THF
19	Polyvinyl alcohol, PVA	Water
20	Polyvinyl chloride, PVC	60% THF : 40% DMF
21	Poly(vinyl pyrrolidone), PVP	65% Ethanol : 35% DMF
22	Poly(vinylidene fluoride), PVDF	DMAC, DMF, acetone

Table 1.4-1: Summary of polymers and solvents used to produce electrospun fibers in the solution form

No	Polymer	Material details	Processing temperature (°C)
1	Polyethylene (PE)	HDPE, $M_w = 1.35 \times 10^5$	200-220
2	Polypropylene (PP)	Isotactic-PP, MI = 0.5	220-240
3	Nylon 12 (PA-12)	$M_w = 3.5 \times 10^4$	220
4	Polyethylene terephthalate (PET)	$M_w = 4.6 \times 10^4$	270
5	Polyethylene naphthalate (PEN)	$M_w = 4.8 \times 10^4$	290
6	PET-PEN blends	75/25, 25/75 (wt%)	290

Table 1.4-2 Summary of polymers electrospun in the melt form

#### 1.4.2.1.2 Viscosity

The viscosity of the solution has a profound effect on electrospinning and the resultant fiber morphology. Since the polymer length will determine the amount of entanglements of the polymer chains in solvent, the molecular weight of the polymer is directly related to the viscosity of the solution and hence on the resultant fiber morphology.

At lower viscosity where generally the polymer chain entanglements are lower, polymer jet breaks up into small droplets and results in beads formation. When the polymer concentration increases, thus the viscosity, there is a gradual change in the shape of the beads from spherical to spindle like until a smooth fiber is obtained<sup>53</sup>. With increased viscosity, the diameter of the fiber also increases.

Gupta et al.<sup>54</sup> found that, for Simultaneous electrospinning of two polymer solutions poly (vinyl chloride)/segmented polyurethane (PVC/Estane(R)) and poly(vinyl chloride)/poly(vinylidene fluoride) (PVC/PVDF), the fiber diameter was directly proportional to the polymer concentration. Deitzel et al.<sup>55</sup> showed that, the solution concentration has been found to most strongly affect fiber size, and fiber diameter had a power law relationship with increasing solution concentration according. As Demir et al<sup>56</sup> stated a cubic relationship for polyurethaneurea copolymer , Hsu et al<sup>57</sup> found a parabolic relation between the fiber diameter and polymer concentration for poly(epsilon-caprolactone) case.

#### 1.4.2.1.3 Surface tension:

Surface tension is another important solution parameter that determines the resulting electrospun fiber morphology. Surface tension is the intermolecular attraction of solution molecules that causes the surface solution to behave as an elastic sheet. In order to initiate electrospinning, the force of the surface tension must be overcome to form the polymer jet. Likewise, solution viscosity plays an important role in determining the effects of surface tension. If a particular solution has a high viscosity, then solvent molecules spread more evenly over the entangled polymer. This in turn reduces the probability of solvent molecules to merge together, thus reducing surface tension. Therefore, a reduction in surface tension reduces the beading of an electrospun fiber<sup>58</sup>. Solvents such as ethanol has a lower surface tension thus they can be added to enhance the formation of smooth fibers<sup>53</sup>.

Since the electrospinning involves stretching of the solution caused by repulsion of the charges at its surface, if the conductivity of the solution will increase, more charges could be carried by polymer jet. Therefore when a small amount of salt or polyelectrolyte is added to the solution, the increased charges carried by the solution will increase the stretching of the solution. As a result, smooth fibers with smaller diameters will yield<sup>59</sup>. Addition of 1 wt% salt addition in biodegradable poly-L-lactic acid polymer solution, nanofibers become bead-free, with relatively smaller diameters in the range of 200-1000 nm. Seo et al<sup>60</sup> showed that addition of additives increased the conductivity which in turn the fiber diameter decreased.

Kim<sup>61</sup> examined the fabrication of gelatin nanofibers by electrospinning using the TFEA/W co-solvent system. They found that no beads-on-string structure was formed for the solution containing ionic salts. Fallahi et al<sup>62</sup> discovered that, adding 0.1% surfactant reduced the solution surface tension and resulted in smaller beads and higher fiber diameters. By increasing the amount of surfactant to 0.3%, big beads and thinner fibers were produced.

### **1.4.2.2 Processing Conditions**

Another important parameter that affects the electrospinning process is the various external factors exerting on the electrospinning jet. This includes the voltage supplied, distance between the needle tip and the feedrate. These parameters have a certain influence in the fiber morphology although they are less significant than the solution parameters.

#### **1.4.2.2.1 Voltage:**

Voltage in the electrospinning process can be compared to the effect that gravity has on a waterfall. High voltage contributes to the electrospinning process by creating the necessary electrostatic force in conjunction with the electric field to overcome solution surface tension. The higher the applied voltage, the more the columbic repulsive force will be present within the polymer jet causing greater stretching and enhance fiber formation<sup>63</sup>.

For the polyethylene oxide-water system, it was observed that the fiber morphology changed from a defect free fiber at an electrical potential of 5.5 kV to a highly beaded structure at 9.0 kV<sup>55</sup>. Megelski et al. determined the dependence of the fiber diameter of polystyrene fibers on voltage, and showed that the fiber size decreased more or less from 20 nm to 10 nm without a dramatic change in the pore size distribution when the voltage was increased from 5 kV to 12 kV<sup>64</sup>.

#### **1.4.2.2.2 Capillary tip to collector distance**

The gap distance between the capillary tip and the collector influences the fiber deposition time, the evaporation rate, and the whipping or instability interval, which subsequently affect the fiber characteristics. When the distance between the tip and the collector is reduced, the jet will have a shorter distance to travel before it reaches the

collector plate. Since the electric field strength will also increase at the same time, it will increase the acceleration of the jet to the collector. As a result, there may not have enough time for the solvents to evaporate when it hits the collector. Gupta and Wilkes found an inverse relationship between applied voltage and fiber diameter but they also stated that bead formation density decreases with increasing distance<sup>54</sup>.

However, there are also cases where at a longer distance, the fiber diameter increases. This increase is due to the decrease in the electrostatic field strength resulting in less stretching of the fibers<sup>65, 66</sup>. When the distance is too large, no fibers are deposited on the collector. Therefore, it seems that there is an optimal electrostatic field strength below which the stretching of the solution will decrease resulting in increased fiber diameters.

#### **1.4.2.2.3 Polymer flow rate**

The flow rate of the polymer from the syringe is an important process parameter as it influences the jet velocity and the material transfer rate. In the case of PS fiber, Megelski et al.<sup>64</sup> observed that the fiber diameter and the pore diameter increased with a boost in the polymer flow rate. As the flow rate increased, fiber had pronounced beaded morphologies and the mean pore size increased from 90 to 150 nm.

#### **1.4.2.2.4 Temperature**

The research indicates that two major parameters depend on temperature and have their influence on the average fiber diameter. A first parameter is the solvent evaporation rate that increases with increasing temperature. The second parameter is the viscosity of the polymer solution that decreases with increasing temperature<sup>67</sup>. When polyurethane is electrospun at a higher temperature, the viscosity of the solution decreases and the produced fibers have a more uniform diameter showing less beading behavior<sup>56</sup>.

### 1.4.3 Applications of Electrospinning

Nanomaterials have been attracting the attention of global materials research these days primarily due to their enhanced properties required for application in specific areas like catalysis, filtration, NEMS, nanocomposites, nanofibrous structures, tissue scaffolds, drug delivery systems, protective textiles, storage cells for hydrogen fuel cells, etc. The broad applications of electrospinning technology are summarized in Table 1.4-3. A quick analysis of nanofibers use for advanced functional applications over the past 10 years indicates that their impact is substantial. A brief discussion on some of the applications of nanofibers and related nanomaterials is given in this section.

Sector	Holy Grail	Applications
Electronics		Super capacitors
Biological and healthcare	Precise positioning & control of nanofibers geometry  Production of quantum wires  Nanofibers mediated functions of cells and tissues	<ul style="list-style-type: none"> <li>• Biosensors</li> <li>• Tissue engineering</li> <li>• Medical devices</li> <li>• Wound dressing</li> <li>• Cables for implantable</li> <li>• Neutral prostheses</li> <li>• Drug coated stents</li> <li>• Artificial heart valve</li> </ul>
Energy	Increase in electron conduction property	<ul style="list-style-type: none"> <li>• Photovoltaics</li> <li>• Fuel cells</li> <li>• Battery separator</li> <li>• Printable electronics</li> <li>• Hydrogen storage</li> </ul>
Biotechnology and Environment	Functionalization of organic molecules onto inorganic fibers	<ul style="list-style-type: none"> <li>• Separation membranes</li> <li>• Affinity membranes</li> <li>• Water filters</li> <li>• Air filters</li> </ul>
Others	Green electrospinning  Industrial scalability, mass production	<ul style="list-style-type: none"> <li>• Gas turbine filter</li> <li>• Engine filter</li> <li>• Personal protective mask</li> </ul>

Table 1.4-3. Foresights on the broad applications of electrospinning

With their outstanding properties such as large surface to volume ratio, high density of pores and excellent surface adhesion, electrospun nanofibers are suitable to be made into filtering media, and also can be used as protective clothing because the highly porous membrane surfaces help in moisture vapor transmission, increase fabric breathability and enhance toxic chemical resistance, all of which are essential properties of protective clothing<sup>68-70</sup>.

Electrospun nanofiber membranes have great potential for applications in supercapacitors, lithium cell, transistors and so on. A non-woven web obtained from electrospinning is used to produce activated carbon nanofibers which possess a high specific surface area and a low electrical resistivity through stabilization, carbonization-activation processes<sup>71</sup>. These webs are particularly useful for supercapacitor electrodes without the addition of binders which normally degrades the performance of supercapacitors<sup>72</sup>. Kim and co-workers<sup>73</sup> demonstrated the potentiality of PAN-based activated carbon nanofiber web as a novel electrode material for an electric double-layer supercapacitor.

For fuel cell applications Pt nanoparticles are dispersed on to the polyaniline (PANI) nanofibers, which will enhance the stability and uniformity. The large surface area in the nanofiber mat has enabled the dispersion of catalyst particles with less time for the deposition of Pt particles<sup>74</sup>. The electrocatalytic performance of methanol oxidation for PANI nanowires supported Pt composite has been found to be much higher than at bulk Pt electrodes. Electrospinning also breakthroughs a major wall on the idealization of fuel cell technology, hydrogen storage problem. Since the hydrogen uptake is proportional to surface area, pore volume nanostructured carbon materials such as carbon nanotubes and carbon nanofibers can device different alternatives for high hydrogen storage capacity<sup>74, 75</sup>.

Nanostructured polymer systems of natural or synthetic origin—in the form of nanofibers, hollow nanofibers, core– shell nanofibers, nanotubes, or nanorods—have a multitude of possible applications in medicine and pharmacy. Electrospun polymer nanofibers have potential application in medical prostheses, orthopedics, plastic surgery, drug delivery, wound dressing and bone repair, etc.

Kim et al. developed a biomimetic nanocomposite with a novel nanofibrous structure by employing electrospinning<sup>76</sup>. These nanocomposite fibers improved the bone-derived cellular activity significantly compared to the pure gelatin equivalent. This method of generating a nanofiber of the biomimetic nanocomposite was effective in producing a biomedical membrane with a composition gradient, which will have potential application in the field of guided tissue regeneration. Khil et al. prepared a

strands of electrospun PCL porous filaments with diameters ranging from 0.5 to 12  $\mu\text{m}$  and used the three-dimensional fabrics as scaffold matrices<sup>77</sup>.

Fine fibers of biodegradable polymers can be directly sprayed/spun onto the injured location of skin to form a fibrous mat dressing, which can make wounds heal by encouraging the formation of normal skin growth and eliminate the formation of scar tissue which would occur in a traditional treatment. Katti et al. also reported that poly(lactide-co-glycolide) (PLGA) nanofibers showed potential as antibiotic delivery systems for the treatment of wounds<sup>78</sup>.

#### **1.4.4 Literature review of electrospun metal-polymer nanocomposites**

After Doshi and Reneker<sup>79</sup> re-highlighted the use of electrospinning as a conventional method for the production of nanocomposite materials, the burgeoning interest of researchers lead the scientific focus to this technique.

Drew et al.<sup>80</sup> is one of the first pioneers that use the synergy of metals nanoparticles with electrospinning. They fabricated of novel metal oxide-coated polymeric nanofibers using the electrospinning technique. The electrospun PAN nanofibers of 100 nm were immersed in an aqueous solution of metal halide salts and halogen scavengers at room temperature to apply the metal oxide coating. An 80-200 nm thick coating of tin dioxide and titanium dioxide were both successfully applied by this method.

At year 2003, Yang<sup>81</sup> et al. prepared PAN nanofibers containing Ag nanoparticles by electrospinning form an Ag-Sol/PAN solution, which was obtained through an in-situ synthetic method. They found that the conductivity of Ag/PAN nanofiber is raised from  $10^{-14}$  S/cm to  $10^{-7}$  S/cm.

Reneker and Hou<sup>82</sup> produced electrospun nanofibers of polyacrylonitrile, containing an iron compound, and converted to carbon nanofibers, with iron particles on their surfaces. The iron particles catalyzed the growth of carbon nanotubes with iron tips. A mechanically strong and electrically conducting path existed between each metal

particle and the supporting nanofiber network, which extended to macroscopic dimensions.

The use of nanocomposite materials for antimicrobial purposes is very diverse. Silver as the most prominent, had been used extensively in literature. Melaiye et al<sup>83</sup>. used electrospinning to enhance the antimicrobial activity of a silver complex which encapsulated into a Tecophilic polymer fiber mat. The fiber mats released nanosilver particles, which in turn sustained the antimicrobial activity of the mats over a long period of time.

Demir et al.<sup>84</sup>, worked on catalytic palladium (Pd) nanoparticles on electrospun copolymers of acrylonitrile and acrylic acid (PAN-AA) mats which were produced via reduction of PdCl<sub>2</sub> with hydrazine. He investigated the effects of copolymer composition and amount of PdCl<sub>2</sub> on particle size. The results showed that, Pd particle size mainly depended on the amount of acrylic acid functional groups and PdCl<sub>2</sub> concentration in the spinning solution. Increasing acrylic acid concentration on polymer chains led to larger Pd nanoparticles. In addition, Pd particle size became larger with increasing PdCl<sub>2</sub> concentration in the spinning solution.

As Demir et al. showed, the increase in metal concentration led to change in fiber diameters. Li et al<sup>85</sup>. demonstrated that by varying the molar ratio of silver nitrate to PAN, the diameters of the monodisperse single-crystal Ag NPs could be adjusted from 3.5 to 10 nm. Similarly, Zhang et al<sup>86</sup>. showed, the average diameters of the ultra-fine PI fibers with different amounts of AgTFA decreased with respect to metal concentration. Besides they found that the number of Ag nanoparticles in the ultra-fine PI fibers increased as the amount of AgTFA increased. Xiongli also came up with the same results. It is observed that the silver nanoparticles with 9-20 nm average diameters were generated on the surface of the gelatin nanofibers. The size of the silver particles could be adjusted by changing the content of AgNO<sub>3</sub>. With increasing the amount of AgNO<sub>3</sub>, the average diameters of fibers decreased. Roso's work also showed that spraying TiO<sub>2</sub> nanoparticle suspension at higher concentrations from 0.5% (w/v) to 1.25% (w/v), 2% (w/v) and 5% (w/v) resulted in an increase of cluster number and dimensions<sup>87</sup>.

The literature work on different applications depending on the used metal precursors, size dimensions and used nanoparticle generation technique is summed up in Table 1.4-4.

Metal	Polymer	Reducing agent	Size (nm)	Use	Reference
Ag	Cellulose acetate (CA)	NaBH <sub>4</sub>	2.8	Antimicrobial	Luong, N. D. <sup>88</sup>
Ag	CA	UV-irradiation	21	Antimicrobial	Son, W. K. <sup>89</sup>
Ag	Gelatin fiber	UV-irradiation	9-20	Antimicrobial	Xu, X. L. <sup>90</sup>
Ag	Polyacrylonitrile (PAN)	DMF	5.8	Catalysis	Lee, H. K. <sup>91</sup>
Ag	PAN	Hydrazine	10		Wang, Y.Z. <sup>92</sup>
Ag	Poly(L-lactide)	H <sub>2</sub>	30	Antimicrobial	Xu, X. <sup>93</sup>
Ag	PVA	UV-irradiation	11	Wound dressing	Hong, K. H. <sup>94</sup>
Ag	Silica	Heat	73	Antimicrobial	Min, K. D. <sup>95</sup>
Fe	PAN	Heat+H <sub>2</sub>	10-20	Carbon fiber production	Hou, H. Q. <sup>82</sup>
Gold	Polyoxyethylene	NaBH <sub>4</sub>	4		Kim, G. M. <sup>96</sup>
Magnetite nP	Polystyrene-b-polyisoprene		4.1	Super paramagnetic	Kalra, V. <sup>97</sup>
MgO	Polysulfone	Aero gel method	2.7-3.3	Warfare agent	Sundarrajan <sup>98</sup>
MnO <sub>2</sub>	PAN	Heat	>50	Catalysis	Oh, G. Y. <sup>99</sup>
MnO <sub>2</sub>	PAN	Heat	10	Lithium-ion batteries	Ji, L. W. <sup>100</sup>
PbS	PVPYR	H <sub>2</sub> S	5		Lu, X. F. <sup>101</sup>
Pd	Chitosan	H <sub>2</sub>	2-3	Catalysis	Peirano, F. <sup>102</sup>
Pd	PAN	Heat	5-40	Catalysis	Chen, L. P. <sup>103</sup>
Pd	PAN-co-styrene	DMF	30-35	Catalysis	Yu, J. X. <sup>104</sup>
Pd	P-EDOT	Electro-chemical	5-10	Biosensor	Santhosh, P. <sup>105</sup>
Pd	Poly(vinyl Alcohol (PVA)	Citrate reduction	8-23	Catalysis	Roy, P. S. <sup>106</sup>
Pt	Polyimidazole	Heat	3	Catalysis	Xuyen, N. T. <sup>107</sup>
Pt	PVPYR	Polyol reduction	2-5	Catalysis	Formo, E. <sup>108</sup>
ZnS:Cu	PVA	H <sub>2</sub> S	3.4	Semiconductor	Wang, H. Y. <sup>109</sup>

Table 1.4-4. Electrospun metal composite nanofibers and usage areas

Table 1.4-4 shows us that there are multiple ways for nanoparticle synthesis for ex-situ or in-situ approaches. The ex-situ approaches produce nanoparticles in narrower

and smaller dimensions<sup>88, 98, 106, 108</sup>, but with applied heat generation or repeated use of the synthesized structure, particles tend to aggregate<sup>82, 99, 100, 107</sup>. The reduction method had a direct influence on the particle sizes. As uv-induced<sup>89, 90, 94</sup> and reductive gas<sup>93, 101, 102, 109</sup> involved in-situ methods produce smaller particles, depending on the generation technique and temperature, particle size may agglomerate several times of its initial dimensions<sup>95, 99, 103, 104</sup>.

Literature studies on thermally treated nanoparticles show a wide distribution of particles sizes. Kim et al.<sup>110</sup> prepared carbon nanofibers containing palladium nanoparticles by electrospinning a polymer solution containing palladium chloride and the subsequent thermal treatment in argon. In the air-stabilization step, palladium cations entrapped in the electrospun PAN based nanofibers surely acted as a stabilization accelerator and they were converted to palladium oxide nanoparticles below 10 nm (Figure 1.4-2).

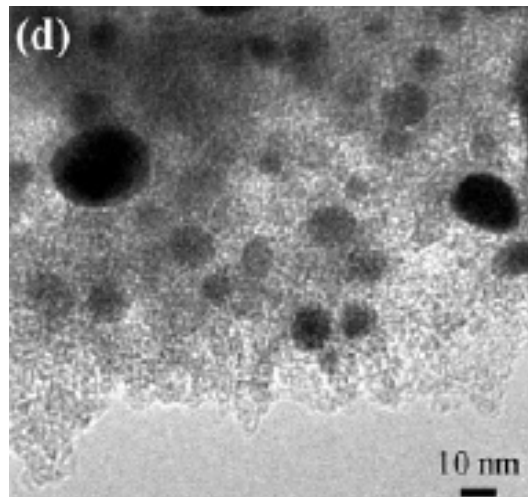


Figure 1.4-2. TEM images of and thermally treated carbon nanofibers at 300°C, courtesy of Kim et al.<sup>110</sup>

Chen et.al. prepared Pd-carrying composite carbon nanofibers based on polyacrylonitrile by electrospinning and carbonization process<sup>103</sup>. Heat treated PAN nanofibers even at 550°C showed an average particle size of 40 nm (Figure 1.4-3).

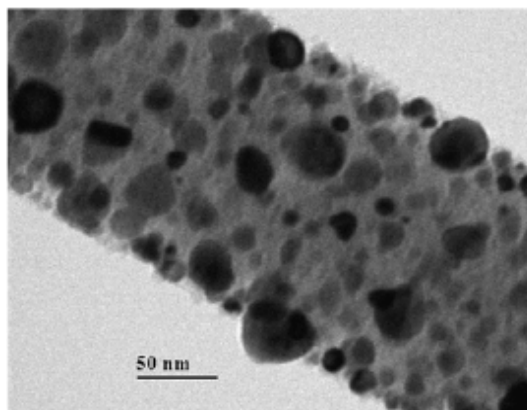


Figure 1.4-3. TEM images of Pd-NP/CENFs, courtesy of Chen et al.<sup>103</sup>.

Yu et al.<sup>104</sup> produced a fibrous catalyst containing palladium nanoparticles via electrospinning of poly(styrene-co-acrylonitrile) (Figure 1.4-4). The fibrous catalyst was characterized by scanning electron microscopy and transmission electron microscopy respectively. The results showed that the diameter of fiber was about 200 nm and the palladium (Pd) nanoparticles were in the range of 30-40 nm in size at room temperature (RT).

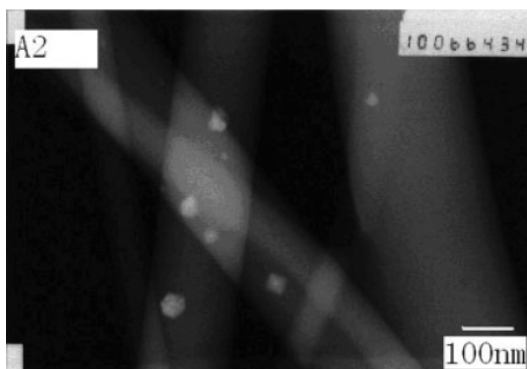


Figure 1.4-4. TEM pictures of Pd nanoparticles, courtesy of Yu et al.<sup>104</sup>.

Zhang et al., synthesized Carbon-supported Pd-Co alloy electrocatalysts for the purpose of the fuel cell cathode oxygen reduction reaction (ORR) in which sodium borohydride is used as a reducing agent. Heat treatment of synthesized catalysts showed an increase in particle size with a rise in temperature<sup>111</sup>. 8.9 nm diametric nanoparticles synthesized at 300°C agglomerated to 13.8 nm at 700°C.

Lai et al.<sup>112</sup> produced carbon nanofibers with Pd nanoparticles by carbonizing electrospun polyacrylonitrile (PAN) nanofibers including Pd(Ac)<sub>2</sub>. Heat treatments showed the reduction of Pd and aggregation into tiny particles inside the nanofibers. The diameter of the Pd particles was less than 5 nm, as shown in the TEM image (Figure 1.4-5-a). Following further heating and annealing at 600°C, the Pd nanoparticles grew to a size of ~15 nm. Some particles were found to aggregate on the nanofiber surfaces (Figure 1.4-5 (b)). At the 800°C stage, the Pd particles grew to a size of ~30 nm and almost all the particles aggregated onto the fiber surfaces. When heated to 1100°C and annealed at this temperature for 1 h, the Pd particles continued to grow on the fiber surfaces. The final diameter of the Pd particles was between 50 and 350 nm. In this case, the diameters of most Pd particles were larger than that of the carbon nanofibers (Figure 1.4-5 (d)).

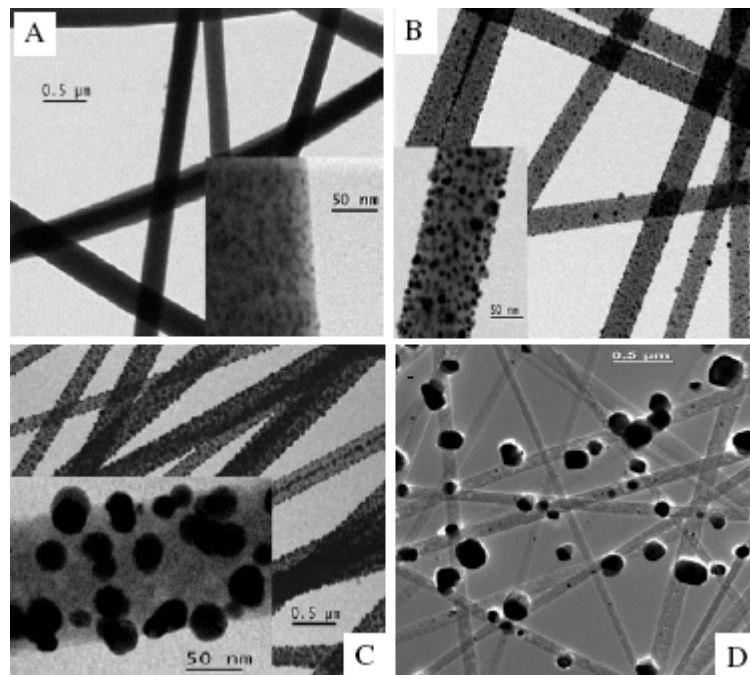


Figure 1.4-5. TEM images of Pd nanoparticles of varying size in/on the carbonized electrospun nanofibers with the process temperature: (A) 400°C, (B) 600 °C, (C) 800 °C and (D) 1100 °C, courtesy of Lai et al.<sup>112</sup>

Huang et al.<sup>113</sup> synthesized palladium nanoparticle-loaded carbon nanofibers (Pd/CNFs) by the combination of electrospinning and thermal treatment processes.

During the reduction treatment and carbonization process, Pd<sup>2+</sup> in the polymer nanofibers was reduced to Pd<sup>0</sup> and aggregates into Pd NPs. Pd NPs were deposited on the surface of CNFs or completely embedded in CNFs. Transmission electron microscopy (TEM) image (Figure 1.4-6) showed that spherical Pd NPs with a mean diameter of about 73 nm were well-dispersed on the CNFs.

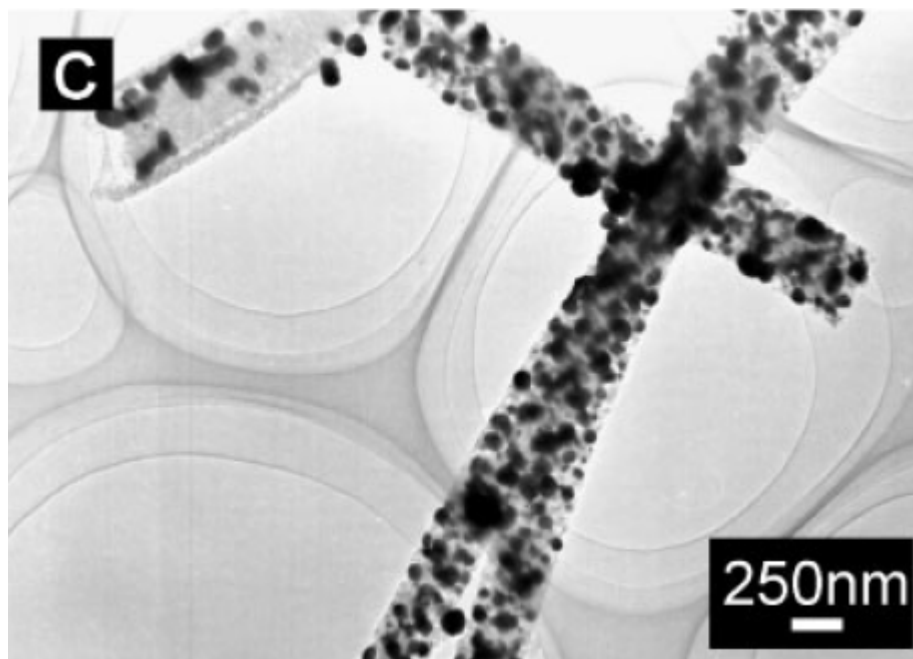


Figure 1.4-6 TEM image of Pd/CNF nanocomposites, courtesy of Huang et al.<sup>113</sup>

### 1.5 Use of metal nanoparticles/CNF for Fuel Cell application

Among the various types of fuel cells, Proton Exchange Membrane Fuel Cells (PEMFCs) possess a series of highly advantageous features such as a low-operating temperature, sustained operation at high-current density, low weight, compactness, potential for low cost and volume, long stack life, fast start-ups and suitability for discontinuous operation<sup>114-116</sup>. These features have elevated PEMFCs as the most promising and attractive candidate for a wide variety of power applications ranging from portable and stationary power supplies to transportation. Therefore, fuel cell and

automotive companies over the past few years have announced several new technologies or prototype vehicles adopting PEMFC's<sup>117-123</sup>.

In conventional fuel cells, electrodes are typically constructed by binding catalyst-loaded carbon particles (e.g., Vulcan XC-72 carbon black- supported Pt) with Nafion®, in which carbon particles facilitate electron transport. A high catalyst loading in these electrodes is typically required because they cannot ensure a simultaneous access of the catalyst to the fuel, electron-conducting diffusion layer and proton-conducting electrolyte. As a result, the cost of precious metallic or alloyed catalysts will be a significant barrier to widespread commercial use of fuel cells.

The limited supply and high cost of the Pt used in PEMFC electrocatalysts necessitate a reduction in the Pt level<sup>124, 125</sup>. In addition, the U.S. Department of Energy has set long-term goals for PEMFC performance in a 50 kW stack that includes operation with cathode loadings of 0.05 mg/cm<sup>2</sup> or less<sup>126, 127</sup>.

Replacing carbon particles with one-dimensional carbon nanomaterials, such as carbon nanotubes (CNTs) and carbon nanofibers (CNFs) can provide effective long range electron transfer in electrodes, thereby resulting in improved catalyst utilization and lower catalyst loading. Researches is being conducted on the deposition of noble metal such as Pt nanoparticles onto CNTs<sup>128-130</sup>, but little has been done on CNFs. Due to the fascinating structure and thermal/electrical/mechanical properties, CNFs are of special interest recently because they can be synthesized in different graphene sheets by cheap and readily available methods<sup>131</sup>.

Li et al. used the cyclic voltammogram method to deposit Pt particles onto CNFs, but the diameters of deposited Pt nanoclusters were too large (50–200 nm) for practical fuel cell applications<sup>132</sup>. Lin et al. reported on the preparation and characterization of Pt/carbon composite nanofibers (Pt/CNFs) by the electrodeposition of smaller Pt nanoparticles ( $\leq 55$  nm) onto electrospun CNFs under different potentials<sup>133</sup>.

It is important to obtain catalysts with smaller particle sizes evenly distributed on CNF surface, which can exhibit increased catalytic activities concomitant with a lower necessary loading.

## 1.6 Motivation

The need for novel nanoparticles is a wide concern of scientific community. But the ways of producing of these extraordinary properties is another concern. Different methodologies and processing techniques are used for manipulating the properties of nanoparticles in atomic dimensions. Most of them came with the same conclusion:

*“It is obligatory to prevent the agglomeration of nanoparticles for size control and distribution.”*

The most efficient and universal way to overcome these problems is to use polymer-assisted fabrication of inorganic nanoparticles and hybrid polymer–inorganic nanocomposites. Electrospinning is a versatile method that will satisfy the primary needs for the in situ synthesis of nanoparticles within a polymer matrix. The very basic nature of the nanofibers produced by electrospinning i.e. very large surface area to volume ratio, flexibility in surface functionality, and superior mechanical performance compared with any other known form of the materials makes it the best choice for maneuvering nanoparticle properties.

In this study, the aim is to control the size and distribution of nanoparticles by polymer assisted fabrication through electrospun nanofibers.

Electrospun polymeric nanofibers are chosen as template materials to tune the synthesis of nanoparticles. Polymer chemistry will mediate to understand the interaction between metal atoms and assisting polymers. Alternatively selected monomer couples will guide for the best the choice of polymer as the template material.

Electrospinning parameters will be examined in detail and different reduction agents and heat treatments will be applied to investigate the effect of processing conditions on nanoparticles generations.

The viability of nanoparticle processing technique will be proved by cyclic voltammetry analysis by evaluating the performance of nanoparticles as catalyst species for fuel cell applications aiming the improvement of catalyst utilization and lowering catalyst loading by uniformly distribution of metal nanoparticles on carbonized nanofibers.

## CHAPTER 2

### 2 EXPERIMENTAL

This chapter details the experimental methodology for the synthesis of nanoparticles supported on carbonized electrospun nanofibers. Polymer synthesis and characterization, electrospinning, reduction of metal salt, carbonization cycle and nanoparticle characterization methods will be thoroughly discussed in this section.

#### 2.1 Materials

Acrylonitrile (AN, MW = 53.1 g/mol) was kindly supplied by Aksa Akrilik Kimya Sanayi A.Ş (Yalova). It was purified first by washing with dilute H<sub>2</sub>SO<sub>4</sub> (Riedel-de-Haen), than dilute Na<sub>2</sub>CO<sub>3</sub> (Fluka), and distilled water. These followed by drying with anhydrous Na<sub>2</sub>SO<sub>4</sub> (Merck), and finally fractional distillation over CaH<sub>2</sub> (Merck) under nitrogen atmosphere. The purified AN was kept at 2 °C in refrigerator. 2-acrylamido-2-methylpropane sulfonic acid (AMPS, MW=207,244 g/mol) was kindly supplied from Lubrizol and used after recrystallization in acetone. Vinyl phosphonic acid (VPA, MW= 108,03 g/mol) was supplied from Clariant, GMBH and used after passing through a

silica column and acrylic acid (AA, MW = 72.06 g/mol) and n-vinyl pyrrolidinone (VPYR, MW=111,14 g/mol), which were supplied from Sigma-Aldrich.

Azobisisobutyronitrile (AIBN, Fluka) was used as addition polymerization initiator after crystallization in acetone. HPLC-grade N,N-dimethylformamide (DMF, Aldrich) was used as solvent during the reactions and electrospinning processes. Palladium (II) chloride (PdCl<sub>2</sub>, MW = 177.33 g/mol, 99.9 % metal basis) and platinum (II) chloride (PtCl<sub>2</sub>, MW = 265.99 g/mol, 99.9 % metal basis) were obtained from Alfa Caesar. Sodium borohydride (NaBH<sub>4</sub>, MW = 37.83 g/mol) was purchased by Alfa Chemicals, while hydrazine (N<sub>2</sub>H<sub>4</sub>, MW = 32.05 g/mol) was taken from Merck.

## 2.2 Polymer Synthesis

The solution copolymerization of acrylonitrile (AN) with different monomers was accomplished in N,N-dimethylformamide (DMF) at 80<sup>0</sup>C for 24 hours. Monomer feed ratios at the solutions were selected according to the reactivity's of monomers to achieve the intended composition in the final polymer backbone. 2,2'-azobis(isobutyronitrile) (AIBN) was used as a radical initiator in 1 ‰ mol ratio with respect to the total monomer moles. The resulting product was precipitated in an appropriate solvent and dried in vacuum oven at 60<sup>0</sup>C until stationary weight. Polymer structures are given at Figure 2.2-1.

Copolymer	Chemical Structure
P(AN-co-AA) Poly(acrylonitrile- co-acrylic acid)	$* \left[ \left( \begin{array}{c} \text{H}_2 \\   \\ \text{C} \\   \\ \text{H} \\   \\ \text{CN} \end{array} \right)_x \left( \begin{array}{c} \text{H}_2 \\   \\ \text{C} \\   \\ \text{H} \\   \\ \text{CO}_2\text{H} \end{array} \right)_y \right]^*$
P(AN-co-VPA) Poly(acrylonitrile - co-vinyl phosphonic acid)	$* \left[ \left( \begin{array}{c} \text{H}_2 \\   \\ \text{C} \\   \\ \text{H} \\   \\ \text{CN} \end{array} \right)_x \left( \begin{array}{c} \text{H}_2 \\   \\ \text{C} \\   \\ \text{H} \\   \\ \text{PO}_3\text{H}_2 \end{array} \right)_y \right]^*$
P(AN-co-AMPS) Poly(acrylonitrile -co-2-acrylamido- 2-methylpropane sulfonic acid)	$* \left[ \left( \begin{array}{c} \text{H}_2 \\   \\ \text{C} \\   \\ \text{H} \\   \\ \text{CN} \end{array} \right)_x \left( \begin{array}{c} \text{H}_2 \\   \\ \text{C} \\   \\ \text{H} \\   \\ \text{C} \\   \\ \text{N} \\   \\ \text{H} \\   \\ \text{C} \\   \\ \text{CH}_3 \\   \\ \text{CH}_3 \\   \\ \text{SO}_3\text{H} \end{array} \right)_y \right]^*$
P(AN-co-VPYR) Poly(acrylonitrile - co- n-vinyl pyrrolidinone)	$* \left[ \left( \begin{array}{c} \text{H}_2 \\   \\ \text{C} \\   \\ \text{H} \\   \\ \text{CN} \end{array} \right)_x \left( \begin{array}{c} \text{H}_2 \\   \\ \text{C} \\   \\ \text{H} \\   \\ \text{N} \\   \\ \text{C} \\   \\ \text{O} \end{array} \right)_y \right]^*$

Figure 2.2-1. Synthesized polymers chemical structures

## **2.3 Polymer Characterization**

### **2.3.1 Fourier Transform Infrared Spectroscopy (FT-IR)**

Fourier Transform Infrared (FT-IR) studies were carried by using Bruker Equinox 55 instrument with Attenuated Total Reflectance (ATR) attachment. Samples were analyzed between  $4000\text{ cm}^{-1}$  and  $600\text{ cm}^{-1}$ . OPUS<sup>TM</sup> software was used for the evaluation of resulting spectrums.

### **2.3.2 Nuclear Magnetic Resonance**

Structural characterization of the materials was carried out with  $^1\text{H}$ ,  $^{13}\text{C}$ -NMR spectroscopy utilizing Unity Inova 500 spectrophotometer (Varian). Deuterated dimethylformamide (DMF-d6), or dimethylsulfoxide (DMSO-d6) were used as locking solvent.

### **2.3.3 Differential Scanning Calorimetry (DSC)**

The thermal properties of copolymers and electrospun films were carried out using a Netzsch Phoenix DSC 204 differential scanning calorimeter (DSC) with aluminum sample pans. Samples were heated at a rate of  $10^\circ\text{K}/\text{min}$  at  $\text{LN}_2/\text{N}_2$  atmosphere. Initial heating cycles were carried out from RT to  $200^\circ\text{C}$ , and then a cooling step is introduced. These thermal cycles were repeated twice. Isothermal steps were included between the heating-cooling sequences, in order to ensure stabilization. The first heating was performed to eliminate the thermal history of the samples.

### 2.3.4 Thermogravimetric Analysis

Thermogravimetric analyses of the samples were carried out using a Netzsch STA 449 C Jupiter Simultaneous thermal analyzer. Samples were heated up to 1200°C at 10°K/min at N<sub>2</sub> atmosphere using Al<sub>2</sub>O<sub>3</sub> crucibles.

## 2.4 Electrospinning

There are multiple parameters affecting the process electrospinning. Polymer concentration, weight percentage of metal salt in the solution, applied voltage and tip to collector distance are directly influencing fiber morphology and dimensions including nanoparticles distribution within the fibers.

Firstly a polymer sample was dissolved in DMF and then metal salt was added at a predetermined ratio by weight with respect to the polymer. Solutions were continuously stirred until the metal salt completely dissolves.

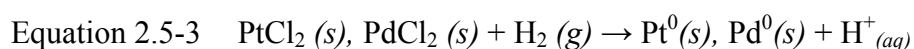
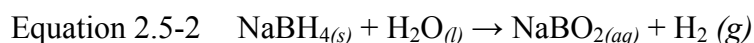
At a typical electrospinning experiment, 10kV DC voltage was applied to grounding collector which was 10 cm apart from the tip of glass pipette. The electrospun fibers were collected on a 10 cm x10 cm aluminum mesh. A summary of the electrospinning conditions are illustrated in Table 2.4-1.

Parameters	Range
Applied voltage	10-25 kV
Tip to collector distance	10-20 cm
Concentration of polymer	8-20% by weight
Concentration of metal	0.5-20% by weight wrt. polymer weight

Table 2.4-1. Summary of the electrospinning working condition

## 2.5 Reduction of metal salt

In order to zero valent metal particles, electrospun metal salts within the polymeric fibers were reduced using strong reducing agents (aqueous hydrazine solution or sodium borohydride). The preferably used one was hydrazine. Previous studies reveal that hydrazine can work as a reducing agent even if attached covalently to the fiber surface<sup>84</sup>.



Oxidation of hydrazine reduced the metal nanoparticles on the surface of polymer fibers (Equation 2.5-1, Equation 2.5-2 and Equation 2.7-1). Electrospun fibers were put on diluted or concentrate reducing agents for predetermined times. Metallic nanoparticles appeared after several hours of reaction time in the immersed state. The change of the color of the film to dark gray indicated that the  $\text{Pd}^{2+}$  ions are reduced to  $\text{Pd}^0$  metal particles (Figure 2.5-1). The intensity of the color depended on the amount of metal used. When the metallization process was completed, electrospun mat was treated with distilled water for the removal of excess reducing agent. After the washing process fiber mats were dried at vacuum oven at  $50^\circ\text{C}$  for 24h.

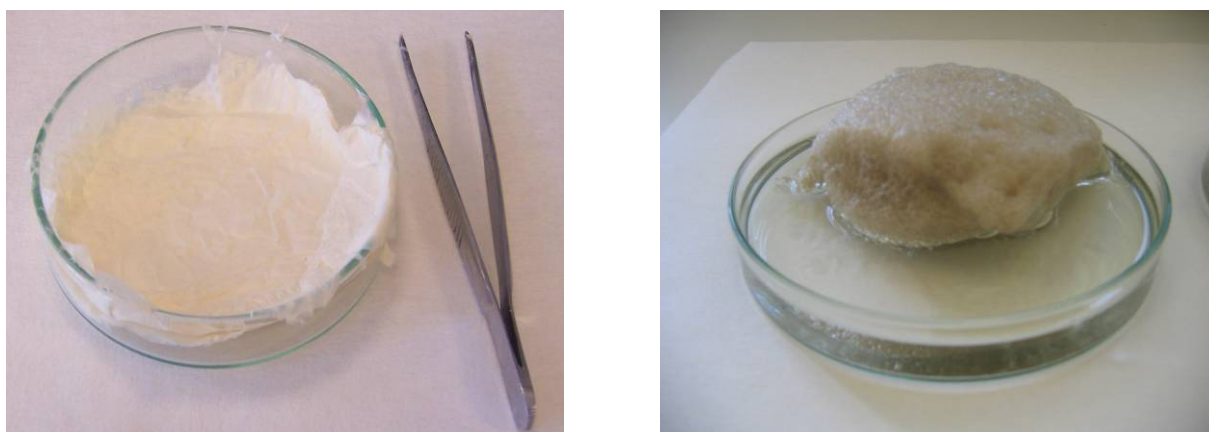


Figure 2.5-1. Reduction reaction: The change of the color of polymeric fiber mat and evolution of  $\text{N}_2(\text{g})$ , before and after.

## 2.6 Carbonization Cycle

After the reduction process electrospun nanofiber mats were heat treated on 2 different cycles (Figure 2.6-1). First heating cycle involves the oxidation and stabilization of the polymeric fibers by heating at 5°C/min from RT to 200°C at O<sub>2</sub>(g) atmosphere and a 30 min isotherm at that temperature. Second heating cycle started with a 10 min isothermal step at 200°C at N<sub>2</sub>(g). The carbonization process began from 200°C to 600°C, 800°C, 1000°C and 1200°C with various heating rates at, 5, 20 and 40°C per minute. Heat treatments were conducted by Netzsch 449C Jupiter TGA instrument, which had 0.1°C sensitivity.

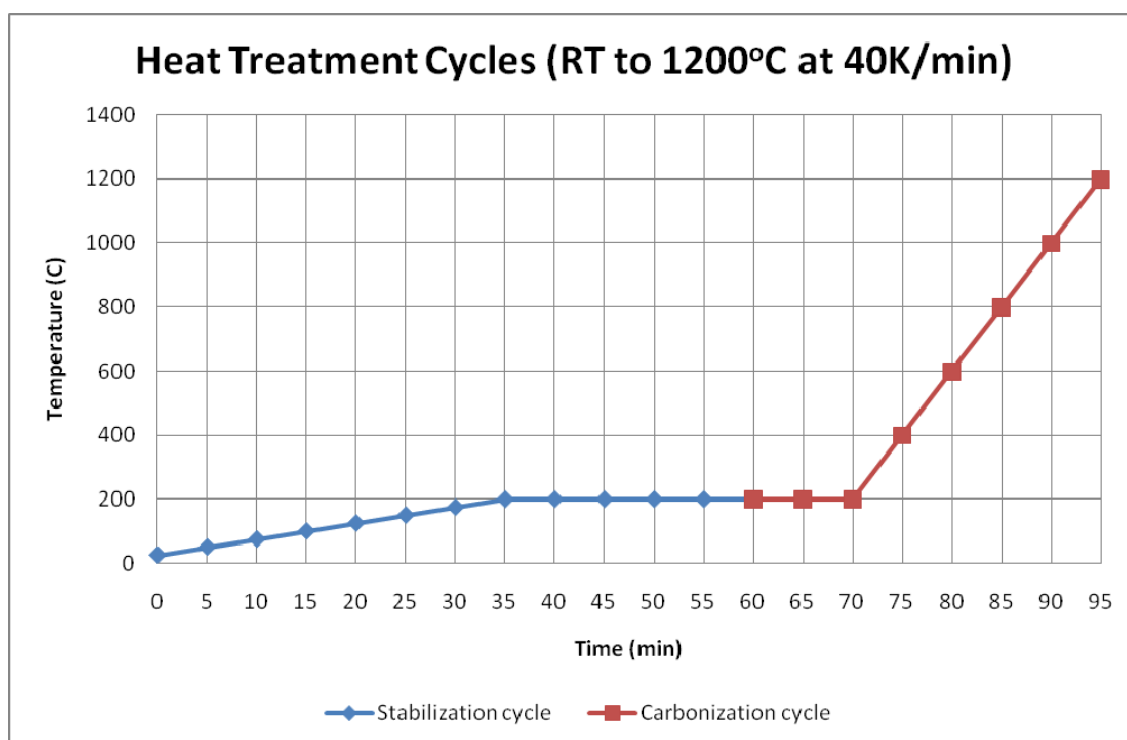


Figure 2.6-1. Heat treatment cycle, 40K/min heating rate for carbonization cycle

## 2.7 Nanoparticle Characterization

### 2.7.1 X-ray Diffraction (XRD)

XRD was a non-destructive tool to characterize the samples by determining the material's crystal structure and the various phases. XRD patterns of scattered x-ray photons showed peaks as specific angles for crystalline materials. Peak patterns were specific to individual materials. Peaks could be analyzed to determine average crystal size using the Debye-Scherrer equation:

$$\text{Equation 2.7-1} \quad L = \frac{0,9 \times \lambda_{K\alpha}}{B_{(2\theta)} \cos \theta_B}$$

where L was the average crystal size, B was the full width half maximum (FWHM) of the peak,  $\theta$  was the diffraction angle and  $\lambda$  was the wavelength of the x-rays, that was fixed at 1.5406 Å for Cu-K $\alpha$ .

Crystal structure and size of the nano metal particles were studied with X-ray powder diffractometer (Bruker AXS-D8, Karlsruhe, Germany). The measurements were performed in the  $2\theta$  range of  $30^\circ$ - $90^\circ$  at 40kV and 40 mA. The step size was  $0.04^\circ$  and step time was adjusted to 20 sec in each step. A typical measurement for the main crystalline (111) peak was adjusted from  $35^\circ$  to  $45^\circ$ .

Peak analysis was performed with the help of Diffrac Plus EVA software. Analysis of the (111) peak scans allowed for curve fitting and background noise subtraction. With a curve fit, the software could calculate the FWHM of the peak, and state the error of the fit. This was then put into the Scherrer formula (Equation 2.7-1) to calculate average crystal size.

## **2.7.2 Optical Characterization**

The electrospun fiber morphologies and nanoparticle dimension were examined via optical characterization techniques.

### **2.7.2.1 Optical microscopy**

During electrospinning, optical microscopy (Nikon Eclipse ME600) was used as the first step for the control of fiber morphology and dimensions according to tip to collector distance and applied voltage.

### **2.7.2.2 Scanning Electron Microscopy (SEM) and Energy Dispersive X-ray Spectroscopy (EDXS)**

The electrospun fibers were investigated using scanning electron microscope (Supra Gemini 35 VP Field Emission SEM, Leo). Fiber diameters and nanoparticle size dimensions are measured from the TIF images captured during investigation of samples. For a representative measurement, an average of 100 counts per sample was taken using image processing programs (IMAGE J version 1.36b and Image-Pro Plus version 4.5.0.29).

Elemental analysis of samples was performed using the Energy Dispersive X-ray detector (XFlash Silicon Drift Detector) attached to SEM instrument by Quantax software. An extracting voltage of 20kV used for analyzing the samples.

### **2.7.2.3 Transmission Electron Microscopy (TEM)**

The size of the nanoparticles could be analyzed via TEM that allowed much higher resolution than the SEM. Jeol 2100 and FEI Super Twin FE-TEM Transmission Electron Microscopy was used (TEM) for particles that was less than 10 nanometers.

## **CHAPTER 3**

### **3 RESULTS & DISCUSSION**

This chapter of the thesis illustrated the results obtained throughout the research. Characterization of synthesized polymers was discussed in detail to better understand the polymer morphology and to guide to explain the electrostatic interaction between the polymer and metal couple. NMR, FT-IR and thermal characterizations were used for polymer characterizations.

Electrospinning processing conditions and solution parameters showed different nanofiber morphologies. Appropriate choice of reduction agents was discussed.

Characterizations of nanoparticles were performed via SEM, TEM and XRD techniques. The effect of heat treatment, the type of copolymer with changing comonomer concentration and the effect of increasing concentration of metal precursor were investigated.

Cyclic voltammetry showed the feasibility of the use of nanoparticles on fuel cell applications. Cyclic voltammetry experiment results supported the aim of the improvement of catalyst utilization and lowering catalyst loading by uniformly distribution of metal nanoparticles on carbonized nanofibers.

### 3.1 Poly(acrylonitrile-co-acrylic acid), P(AN-co-AA)

#### 3.1.1 Polymer Characterization

Poly(AN-co-AA) copolymer was synthesized by solution polymerization of AN with AA in DMF solvent at 80°C for 24h. 5, 10 and 20 mole % AA containing reactions were run. AIBN was used as addition polymerization initiator at a concentration of 0.1 mol % relative to total mol number of AN and AA (Table 3.1-1).

Copolymer	Comonomer in feed (% mol)	Comonomer in polymer backbone (% mol)	Reactivity ratio ( $r_1/r_2$ )	Yield (%)
P(AN-co-AA)	2.5	5	AN/AA	45.8
	5.2	10	=	24.5
	10.8	20	0.51/3.84	36.2

Table 3.1-1. Synthesis of Poly(AN-co-AA)

The product was precipitated at acetone and the yield changed from 24.5% to 45.8%. The monomer feed in AA is selected according to the reactivity ratios calculated from NMR characterization results of the prior syntheses. The results obtained were in accordance with the results at Moghadam's<sup>134</sup> work obtained by Kelen-Tudos method.

### 3.1.1.1 FT-IR characterization

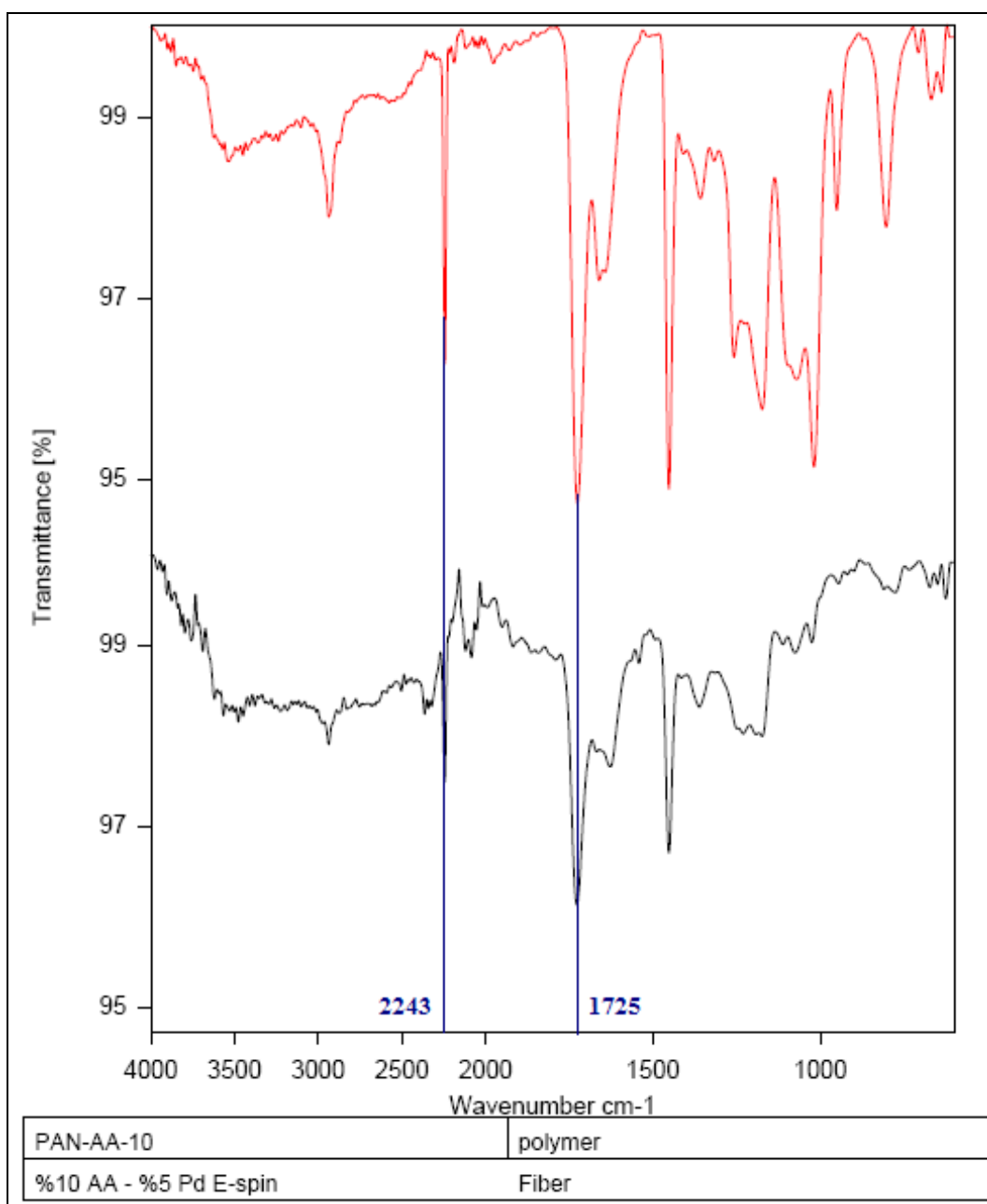


Figure 3.1-1 FT-IR spectrum of P(AN-co-10%AA) and P(AN-co-10%AA)-5%Pd

FT-IR spectrum (Figure 3.1-1) analysis showed the characteristic vibration of  $-\text{CN}$  at  $2243\text{ cm}^{-1}$ . Carbonyl  $-\text{C}=\text{O}$  vibration at  $1725\text{ cm}^{-1}$  showed that AA moiety was inserted into the backbone of AN.

### 3.1.1.2 NMR characterization

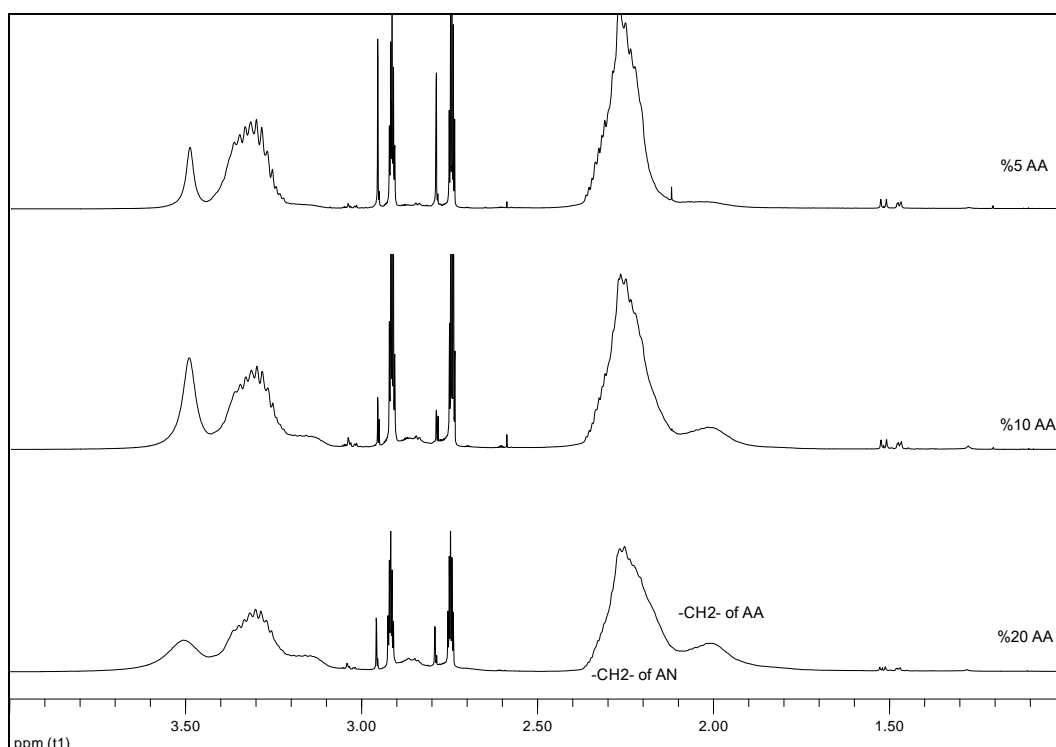


Figure 3.1-2. <sup>1</sup>H NMR spectrums of P(AN-co-AA) at different AA concentrations from 5%, 10% and 20% from top to bottom respectively

<sup>1</sup>H NMR spectrums (Figure 3.1-2) were the second steps for the verification of polymer structure. The shifts at 2.01 ppm represented the methylene group of AA in the polymer backbone, whereas the peak at 2.23 ppm represents AN. The strong absorption at 2.91 ppm and 2.73 ppm were the d6-peaks for DMSO. The revealed integration data from <sup>1</sup>H NMR spectrums helped to calculate the ratio of AA to AN in the polymer backbone. The calculated reactivity ratios (0.51/3.84; AN/AA-Table 3.1-1) showed that the polymer structure was mainly a blocky-copolymer.

### 3.1.1.3 Thermal characterization

Thermal investigations of P(AN-co-AA) showed the glass transition of polymer shifts from 97.3°C to 116.9°C as the AA concentration increased within the polymer backbone (Figure 3.1-3). Thermogravimetric analysis of P(AN-co-AA) showed that as the AA content in backbone increased, polymer lost the high temperature stability

(Figure 3.1-4). The start of the degradation process shifted from 349°C to 157°C, suggesting that the cyclization process for the nitrile side chain in AN backbone was catalyzed by the loss of acidic group in AA structure. Early decomposition of polymeric integrity hardened the use of P(AN-co-AA) nanofibers for CNF applications.

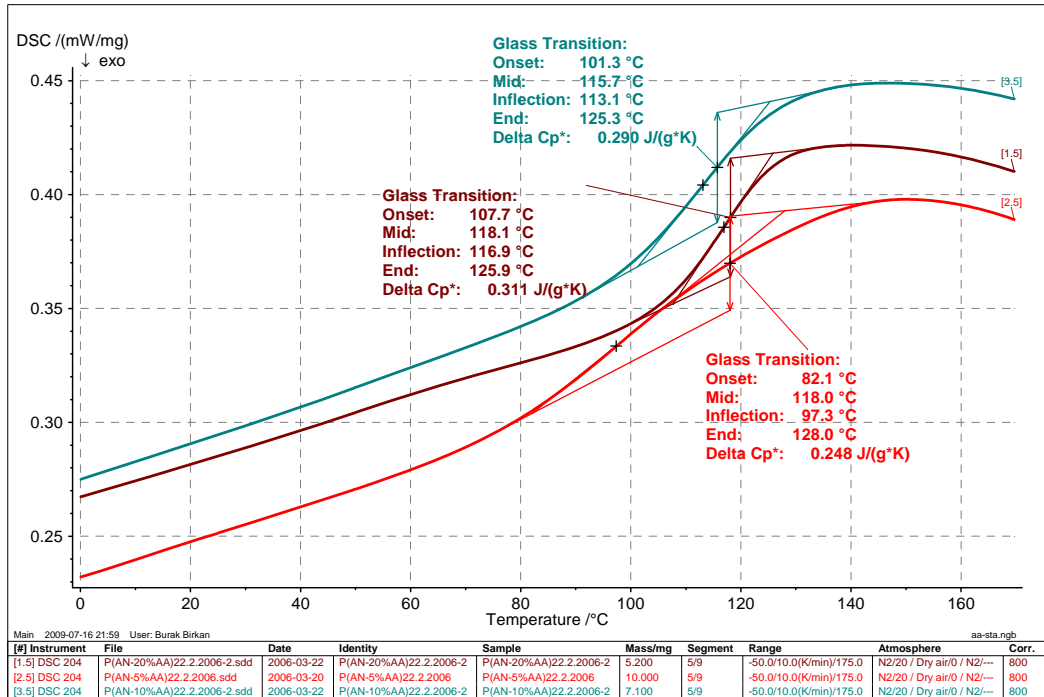


Figure 3.1-3 DSC analysis of P(AN-co-AA) at different AA concentrations.

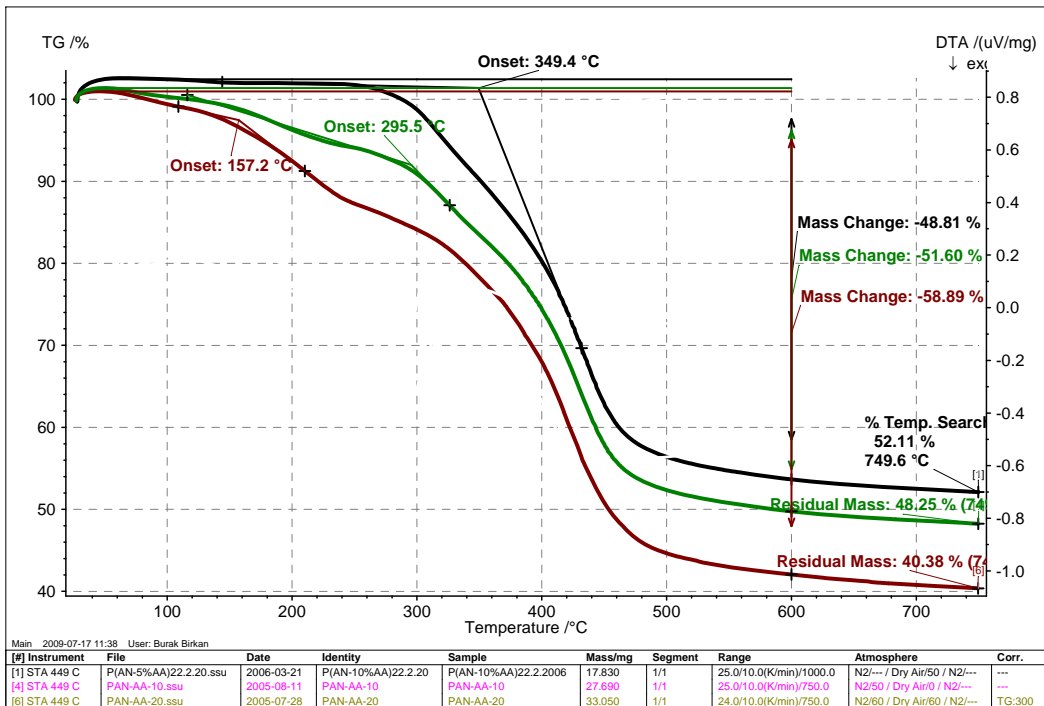


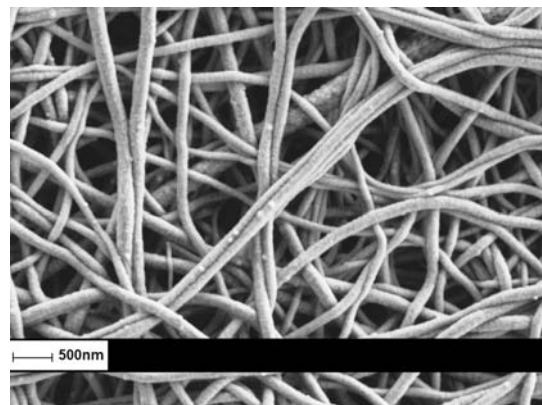
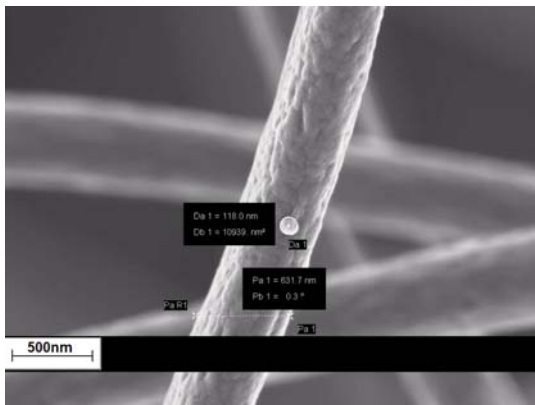
Figure 3.1-4 TGA analysis of P(AN-co-AA) at different AA concentrations.

### 3.1.2 Electrospinning characterization

Copolymer	Functional monomer % <sup>1</sup>	Metal	Metal % <sup>2</sup>	Polymer % <sup>3</sup>	Fiber diameter (nm)
P(AN-co-AA)	5	Pd	0.5	19.8	867±71
			1	19.8	548±52
			5	19.8	440±56
	12.5			153±23	
	20		12.7	214±18	

Table 3.1-2. Electrospun P(AN-co-AA) polymer fiber diameter. 1: Functional monomer in polymer backbone 2: Metal weight percentage with respect to polymer weight in electrospinning solution 3: Polymer weight percentage in electrospinning solution

P(AN-co-AA) copolymer samples were electrospun at 10kV voltage difference between the tip and the collector which were 15 cm apart from each other. Table 3.1-2 showed that as the metal concentration in the electrospun solution increases, an increase in fiber diameters is observed for P(AN-co-5%AA). Since the viscosity of the solution was high enough to overcome the surface tension to form a stable fiber jet, the increased conductivity of the solution led to the formation of more uniform and thinner fibers.



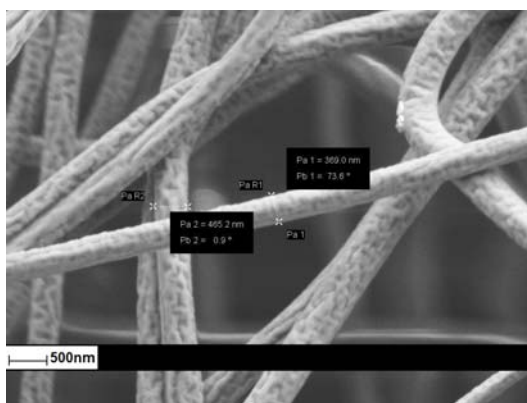


Figure 3.1-5. SEM pictures for P(AN-co-5%AA) at different Pd loadings a)0.5% b)1% c)5% respectively

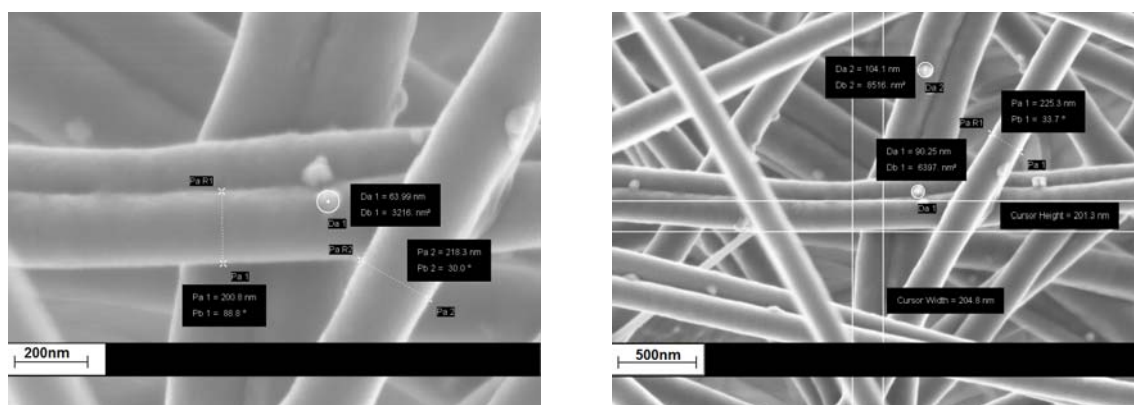


Figure 3.1-6. SEM pictures for P(AN-co-AA)-5%Pd at different AA concentrations a)10%, b)20% respectively

The electrospun polymeric fiber mats were metalized after reduction of Pd metal into its zero valent in dilute hydrazine solution in 1h reaction. SEM analyses of fibers showed metal nanoparticles were formed within the fiber surface. The sizes of the metal nanoparticles were found to be on the order of couple 10 nm's. The change in the acrylic acid content within the polymer backbone from 10% to 20% increased the particle size from  $65 \pm 6.4$  nm to  $96 \pm 8.3$  nm, as the AA content in the polymer (Figure 3.1-6). This result was in accordance with Demir's<sup>84</sup> work. The electrostatic interaction between Pd cation and the acrylic acid carboxylic group might have affected the size and the distribution of the metal within the polymeric fiber. The increase in particle size might be attributed due the effect of the blocky nature of the copolymer, where the nucleation of metal particles took within the size domain of AA groups in the reduction reaction.

## 3.2 Poly(acrylonitrile-co-vinyl phosphonic acid), P(AN-co-VPA)

### 3.2.1 Polymer Characterization

Copolymer	Comonomer in feed (% mol)	Comonomer in polymer backbone (% mol)	Reactivity ratio ( $r_1/r_2$ )	Yield (%)
P(AN-co-VPA)	2.8	5	AN/VPA	33.3
	5.5	10	=	33.7
	9.6	20	0.49/2.55	38.5

Table 3.2-1 Synthesis of Poly(AN-co-VPA)

Poly(AN-co-VPA) copolymer was synthesized by solution polymerization of AN with VPA in DMF solvent at 80°C for 24h. 5, 10 and 20 mole % VPA containing reactions were run. AIBN was used as addition polymerization initiator at a concentration 0.1 mol % relative to total mol number of AN and VPA. The product was precipitated at acetone and the yield changed from 33.3% to 38.5% (Table 3.2-1). The monomer feed in VPA was selected according to the reactivity ratios calculated from NMR characterization results of the prior syntheses.

#### 3.2.1.1 FT-IR characterization

FT-IR spectrum (Figure 3.2-1) analysis showed the characteristic vibration of -CN at 2243  $\text{cm}^{-1}$ . The bands at around 1200  $\text{cm}^{-1}$  were developed from -P=O symmetric and antisymmetric stretching vibrations. Also, the P-O-(H) stretching vibrations can be found at 1053  $\text{cm}^{-1}$ . As the Pd concentration in the polymer fiber

increased from 0.5% to 5%, the intensity of the 1174  $\text{cm}^{-1}$  peak shifted to 1220  $\text{cm}^{-1}$ . The shift in the group stretching frequency of the  $-\text{P}=\text{O}$  group suggested an electrostatic interaction between Pd metal with the phosphonic side chain.

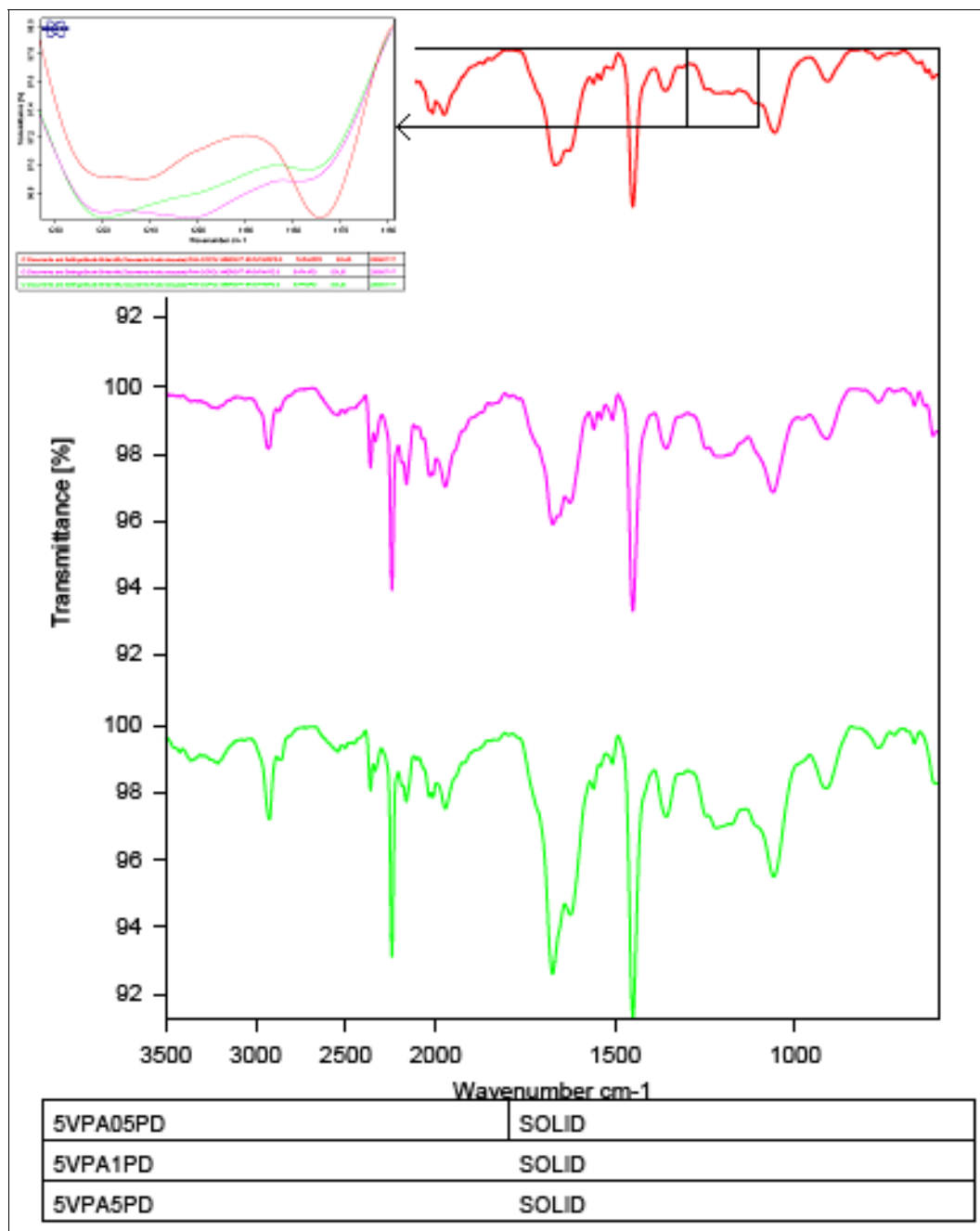


Figure 3.2-1. FT-IR spectrum of P(AN-co-5%VPA) electrospun fibers at different Pd metal content, 0.5%, 1% and 5% from top to bottom.

### 3.2.1.2 NMR characterization

Figure 3.2-2 showed the  $^1\text{H}$  NMR spectrums for P(AN-co-VPA) at different VPA content in polymer backbone from 5% to 20% from top to bottom respectively. The base peak at 2.03 ppm and 2.1 ppm represented the methylene group of AN and VPA in the polymer backbone. The strong absorption at 2.91 ppm and 2.73 ppm were the d6-peaks for DMSO. Since the integration was hardly difficult due to the overlap of two methylene groups, the phosphonic acid hydrogen's were used to calculate the ratio of AN to VPA in the polymer backbone. The calculated reactivity ratios (0.49/2.55; AN/VPA-Table 3.2-1) showed that the polymer structure was mainly a blocky-copolymer.

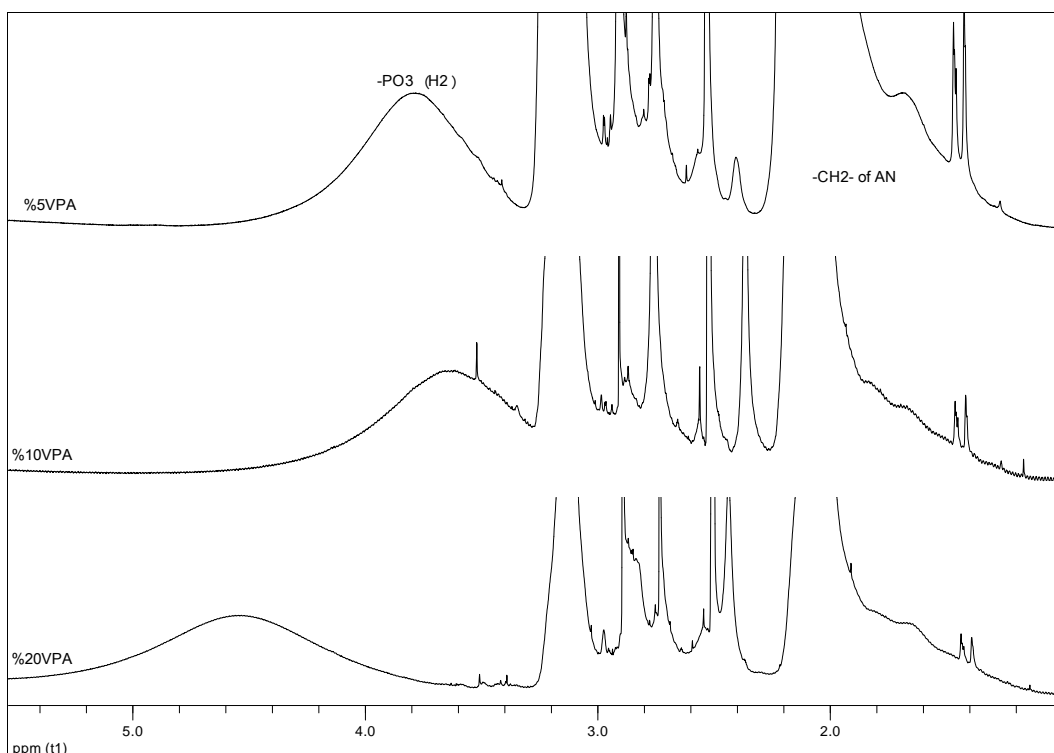


Figure 3.2-2  $^1\text{H}$  NMR spectrums of P(AN-co-VPA) at different VPA concentrations from 5%, 10% and 20% from top to bottom respectively

### 3.2.1.3 Thermal characterization

DSC analysis of P(AN-co-VPA) copolymers showed a decrease in glass transition with respect to increased VPA content in the polymer backbone from 5% to 20%.  $T_g$  values changed from 122.5°C to 99.9°C (Figure 3.2-3). The degradation mechanism for copolymers showed a delayed degradation temperature for the polymer backbone from 381°C to 392°C which was associated with the cyclization of nitrile chain in the polymer backbone (Figure 3.2-4). The flame retardancy properties of phosphonic acid groups within the polymer chain retarded the cyclization reaction. The increased thermal properties of the polymer showed a residual mass of 54.4% for 20%VPA in copolymer which was considered to be almost 1.5 times for P(AN-co-20%AA). But the increased rate of decomposition at the early stages of decomposition mechanism prevented the stabilization reactions for further carbonization reactions.

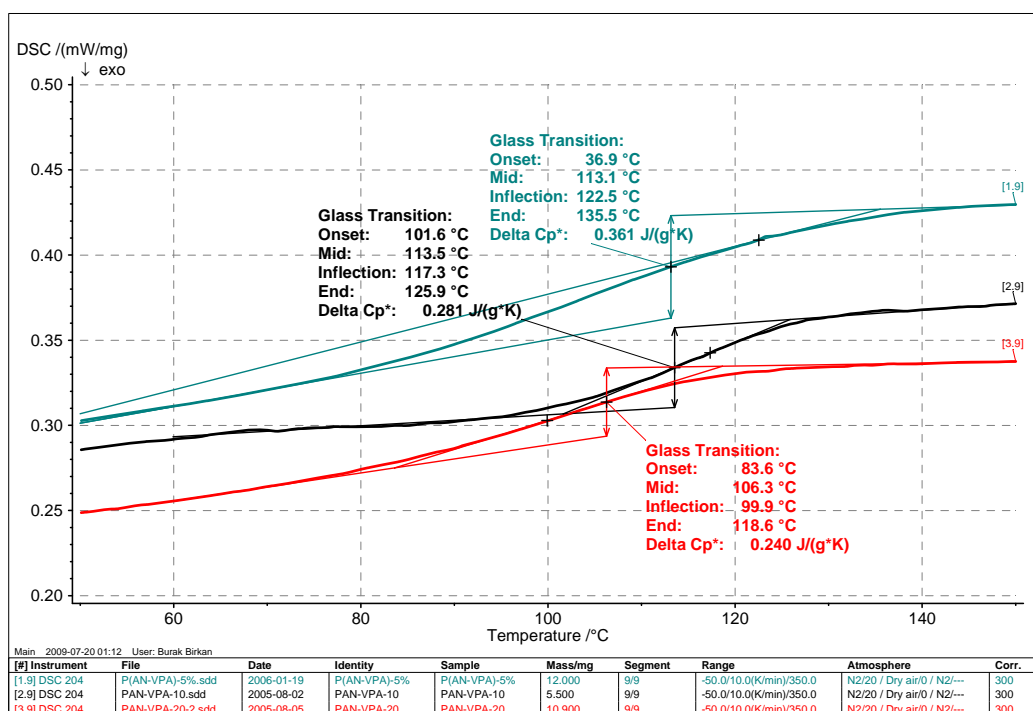


Figure 3.2-3 DSC analysis of P(AN-co-VPA) at different VPA concentrations from 5%, 10% and 20% from top to bottom respectively.

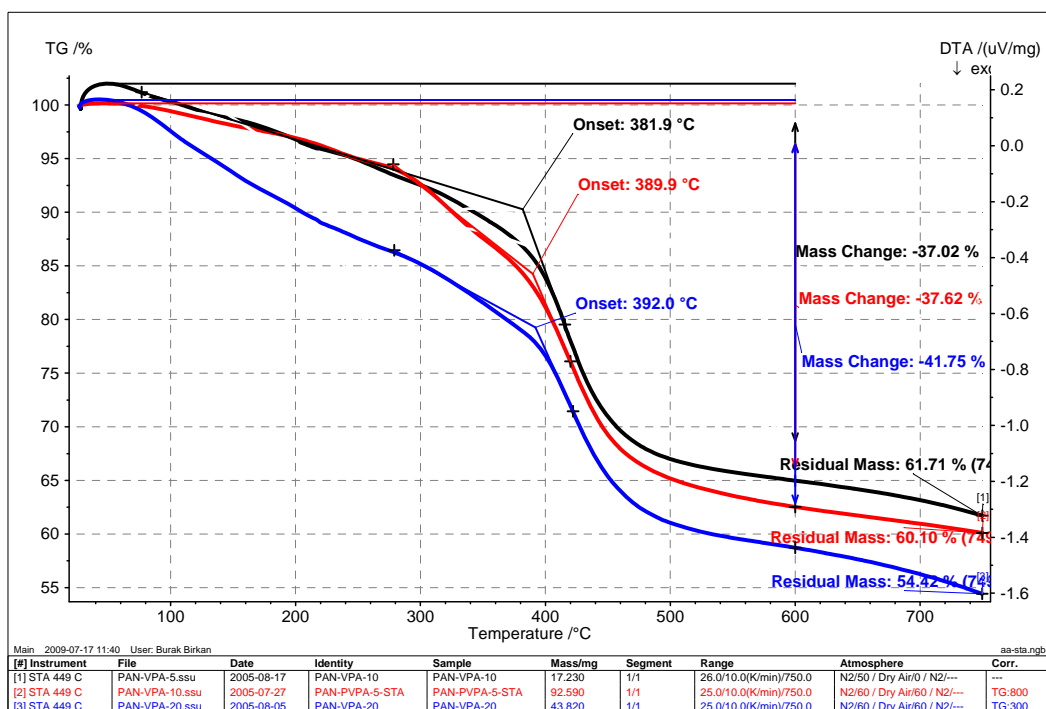


Figure 3.2-4 STA analysis of P(AN-co-VPA), 5%, 10% and 20% respectively

### 3.2.2 Electrospinning characterization

Copolymer	Functional monomer % <sup>1</sup>	Metal	Metal % <sup>2</sup>	Polymer % <sup>3</sup>	Fiber diameter (nm)
P(AN-co-VPA)	5	Pd	0.5	20	289±36
			1	20	255±40
			5	20	230±26
	10		17.9	321±56	
	20		13.7	290±35	

Table 3.2-2 Electrospun P(AN-co-VPA) polymer fiber diameter. 1: Functional monomer in polymer backbone 2: Metal weight percentage with respect to polymer weight in electrospinning solution 3: Polymer weight percentage in electrospinning solution

The beaded structure of the electrospun P(AN-co-5%VPA)-0.5%Pd was enhanced by adding up to 5% Pd in the electrospinning solution where more uniform and thinner

fibers could be obtained (Table 3.2-2). Average fiber diameters reduced from 289 nm to 230 nm and finer fibers were obtained (Figure 3.2-5).

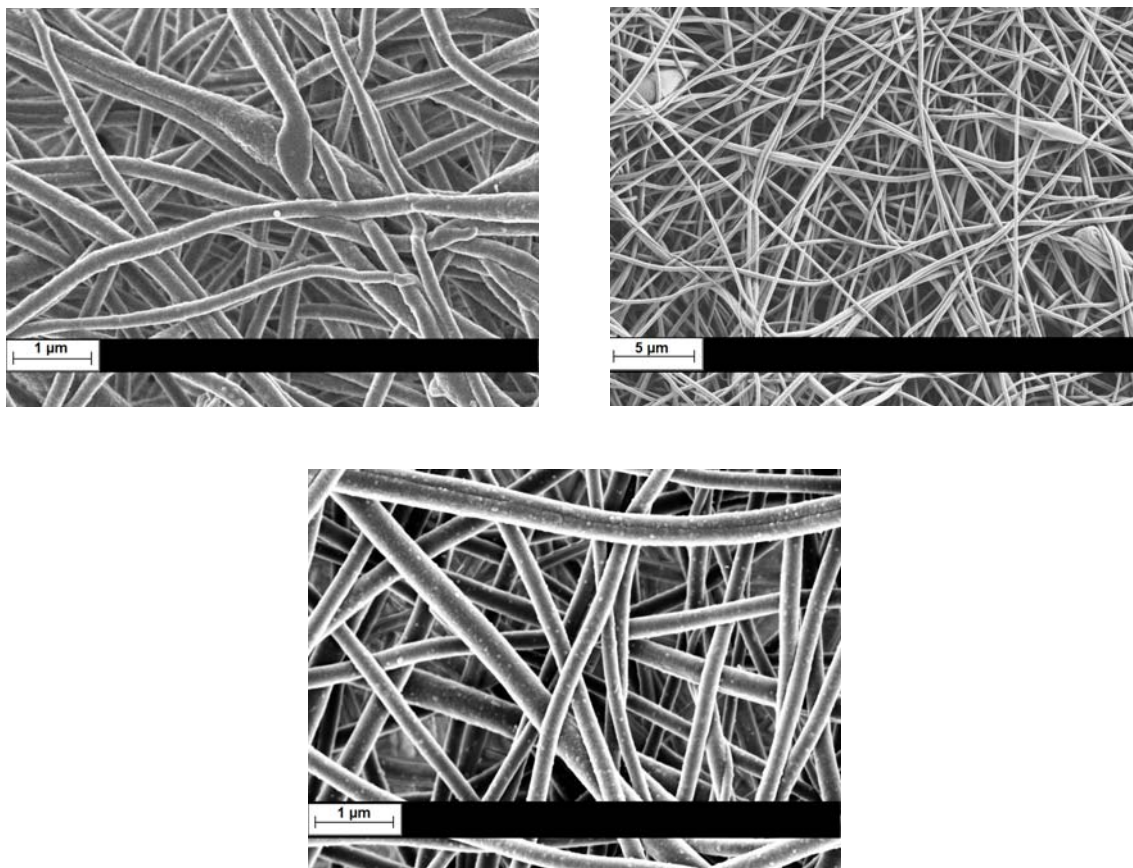


Figure 3.2-5. SEM pictures for P(AN-co-5%VPA) at different Pd loadings a)0.5% b)1% c)5%

As VPA content in polymer was increasing the fibers become thicker and although dilute solutions were used, after metallization of fibers via reducing the salt, porous fiber structure and the texture deformed from uniformity and fibers merged together (Figure 3.2-6). The same problem was encountered again during the heat stabilization of fibers (Figure 3.2-7). The melting of fibers at 200°C changed the morphology and rather than a fiber net, a film of fibers was obtained.

Average particle size of metal nanoparticles also tended to increase within the increasing VPA content of the polymers. Particle size rose from  $62\pm 7.9$  nm to  $75\pm 8.6$  nm and  $87\pm 9.4$  nm as the VPA concentration increased from 5% to 20%. Metal nanoparticles seemed to agglomerate and cluster of nanoparticles rather than single crystals were obtained. The conclusion for AA case could also be thought for VPA case.

The electrostatic interaction of the phosphonic acid moiety within the block copolymer nature of the polymeric fiber with the Pd atom might have centralized the nanoparticle formation on the VPA domain.

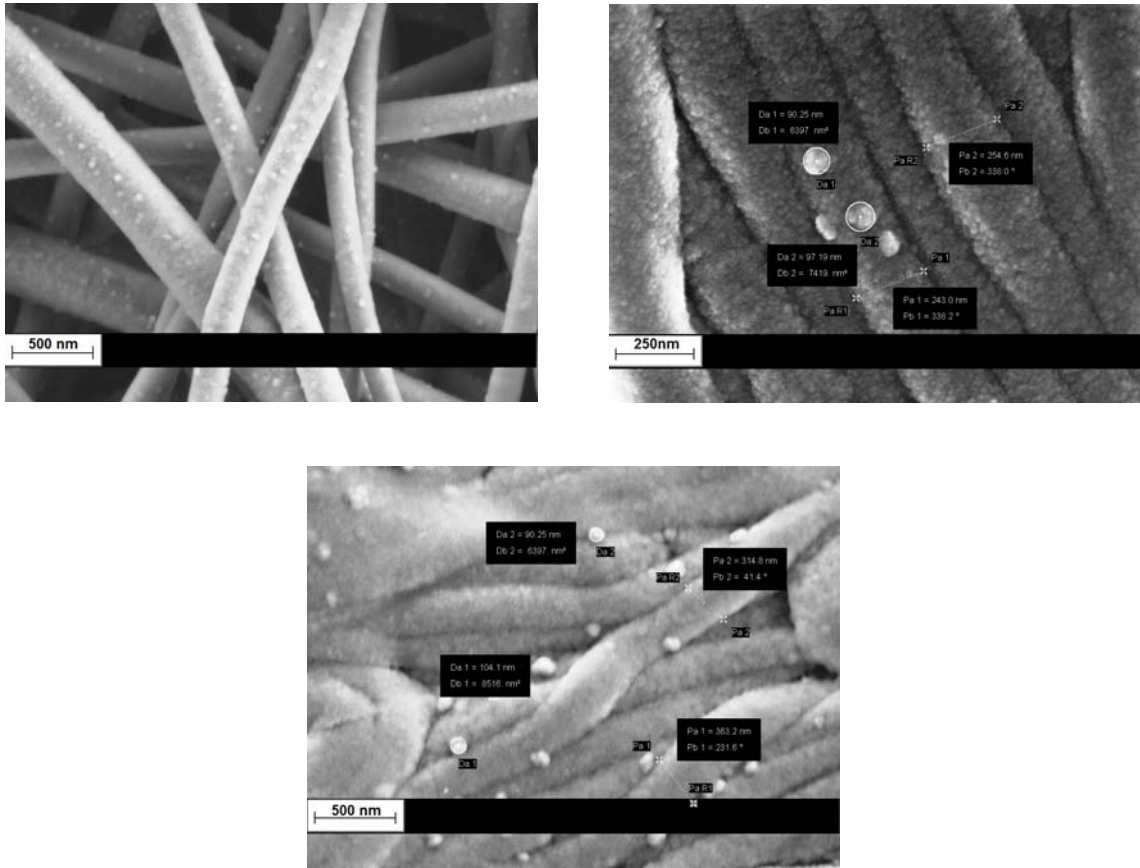


Figure 3.2-6 SEM pictures for P(AN-co-VPA)-5%Pd at different VPA concentrations a)5% b)10% and c)20% respectively

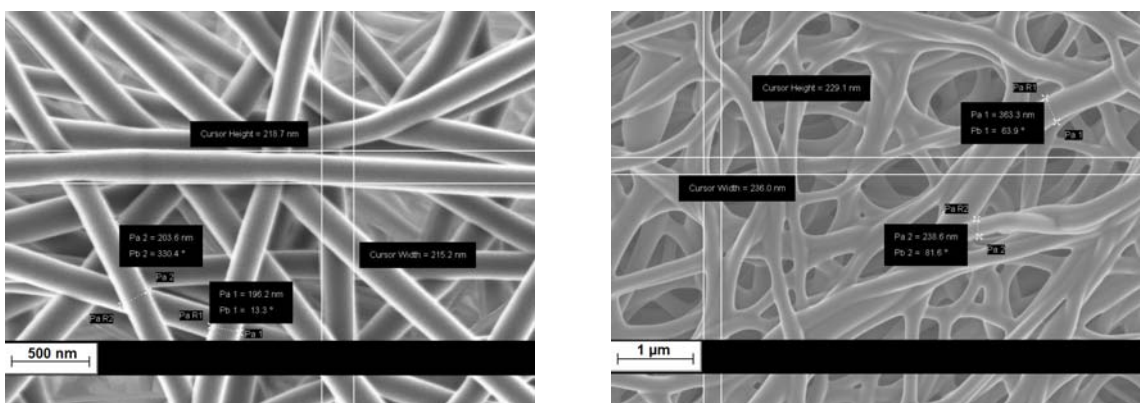


Figure 3.2-7. SEM pictures for P(AN-co-5%VPA) fibers before and after heat treatment at 200°C

### 3.3 Poly(acrylonitrile-co-2-acrylamido-2-methylpropane sulfonic acid), P(AN-co-AMPS)

#### 3.3.1 Polymer Characterization

Copolymer	Comonomer in feed (% mol)	Comonomer in polymer backbone (% mol)	Reactivity ratio ( $r_1/r_2$ )	Yield (%)
P(AN-co-AMPS)	3.5	5	AN/AMPS	78.2
	7.0	10	=	80.6
	12.0	20	0.88/5.96	70.4

Table 3.3-1 Synthesis of Poly(AN-co-AMPS)

Poly(AN-co-AMPS) copolymer was synthesized by solution polymerization of AN with AMPS in DMF solvent at 80°C for 24h. 5, 10 and 20 mole % AMPS containing reactions were run. AIBN was used as addition polymerization initiator at a concentration of 0.1 mol % relative to total mol number of AN and AA. The product was precipitated at methanol and the yield changed from 70.4% to 80.6% (Table 3.3-1). The monomer feed in AMPS was selected according to the reactivity ratios calculated from NMR characterization results of the prior syntheses.

##### 3.3.1.1 FT-IR characterization

FT-IR spectrum (Figure 3.3-1) analysis showed the characteristic vibration of -CN at 2243  $\text{cm}^{-1}$ . The strong absorption bands at round 1540  $\text{cm}^{-1}$  and 1659  $\text{cm}^{-1}$  confirmed the amide groups of the AMPS unit in the host polymer. In addition, two

sharp peaks at  $1109\text{ cm}^{-1}$  and  $1209\text{ cm}^{-1}$  verifying the S-O stretching typical of the sulfonate groups were clearly observed.  $1610\text{ cm}^{-1}$  and  $1420\text{ cm}^{-1}$  bands were due to  $-\text{NH}_2$  stretching and deformations bands associated to AMPS side chain.

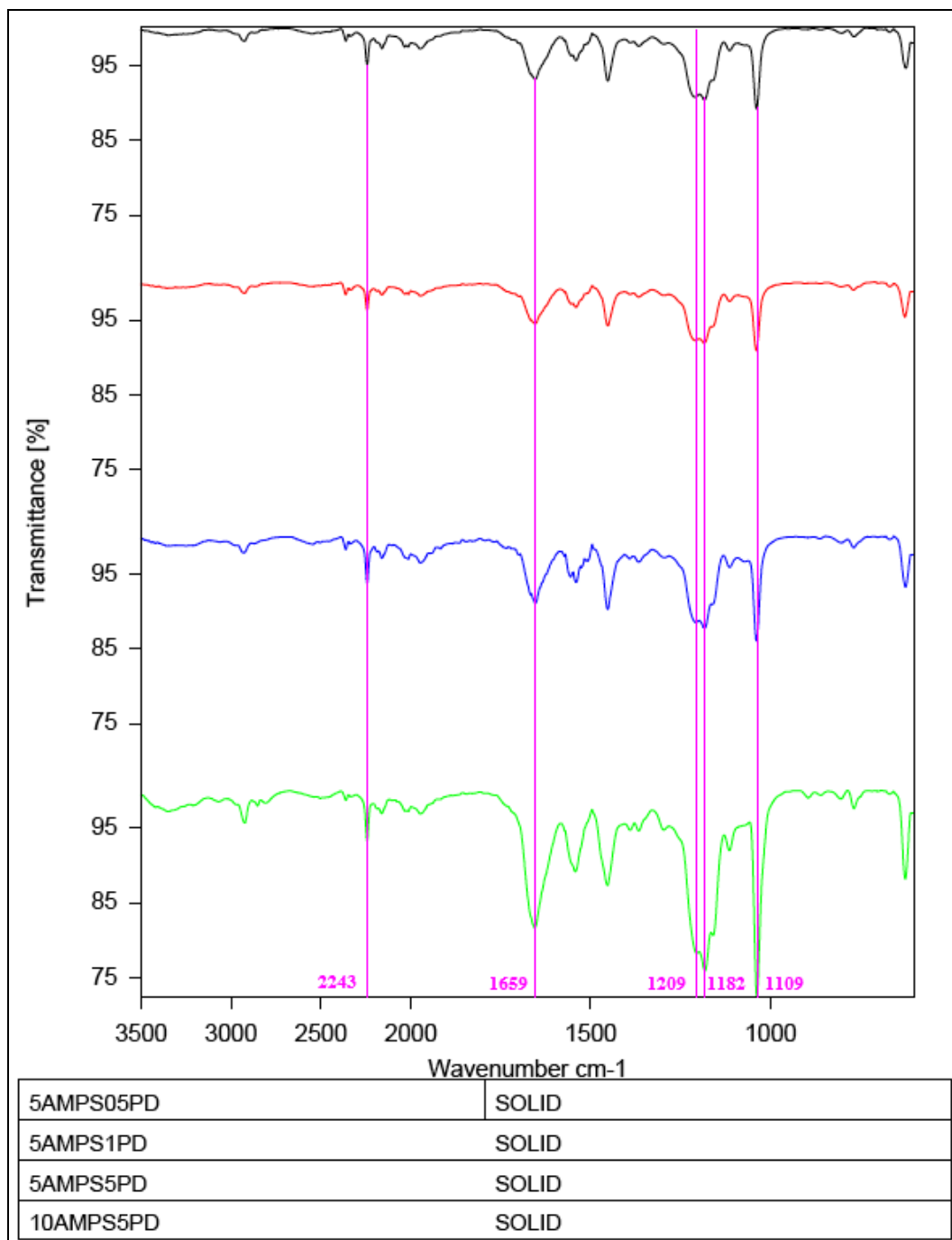


Figure 3.3-1 FT-IR spectrum of P(AN-co-AMPS) electrospun fibers at different Pd metal content, 0,5%, 1% and 5% from top to bottom

### 3.3.1.2 NMR characterization

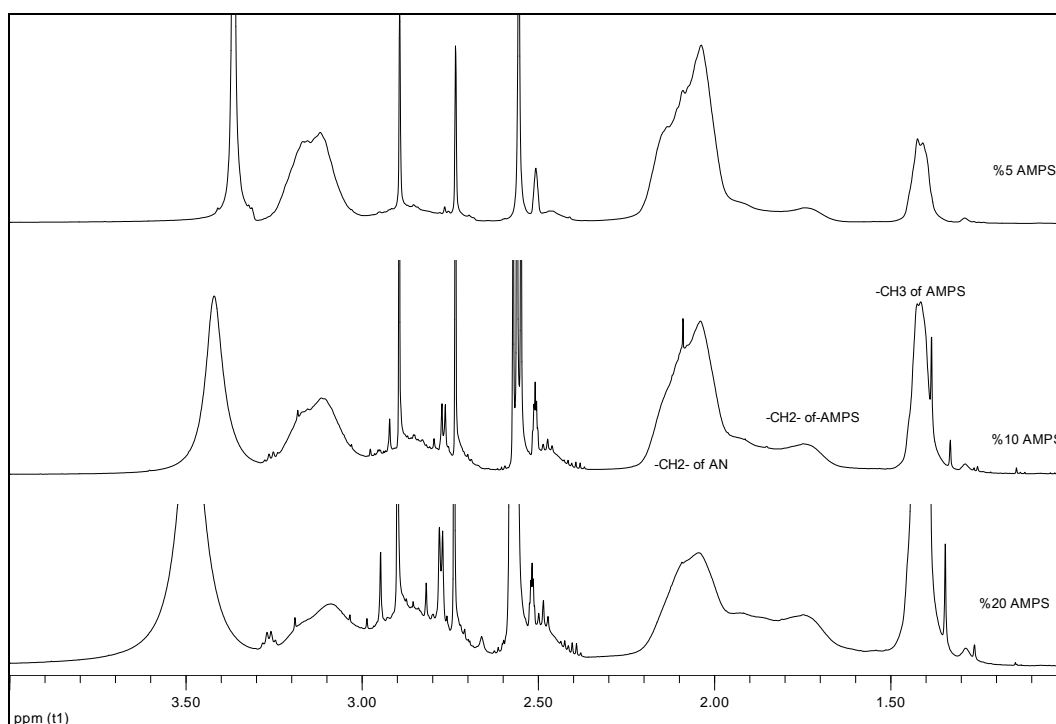


Figure 3.3-2  $^1\text{H}$  NMR spectrums of P(AN-co-AMPS) at different AMPS concentrations from 5%, 10% and 20% from top to bottom respectively

The  $^1\text{H}$ -NMR spectrum (Figure 3.3-2) analysis of P(AN-co-AMPS) showed methine protons of AN and AMPS at around 3.00 to 3.50 ppm and methylene protons of AN at the backbone at 2.04 ppm and 1.72 ppm for AMPS at the backbone. The methyl groups of AMPS at the side chain were shown at 1.43 ppm. The integral of the methyl groups with respect to AN methylene groups was used to calculate the content of AMPS within the polymer. The calculated reactivity ratios (0.88/5.96; AN/AMPS-Table 3.3-1) showed that the polymer structure was mainly a blocky-copolymer.

### 3.3.1.3 Thermal Characterization

Thermal analysis (Figure 3.3-3 and Figure 3.3-4) of the polymer showed a broad glass transition around 89.3°C and shifting to 100.1°C as AMPS content in the polymer was increasing. Fast decomposition of AMPS side chain began after losing of water in sulfonic acid which followed by the cyclization of nitrile chain and breakage of amide linkage in AMPS side chain led to a fast decomposition up to 270°C from 312°C as AMPS content in the polymer is increasing. It continued sharply to about 560°C by the loss of up to 57% of total mass to that temperature. The residual mass was decreasing to 40% at 750°C with P(AN-co-20%AMPS). This early decomposition of copolymer nature lacks the suitability for the formation of stable CNF's.

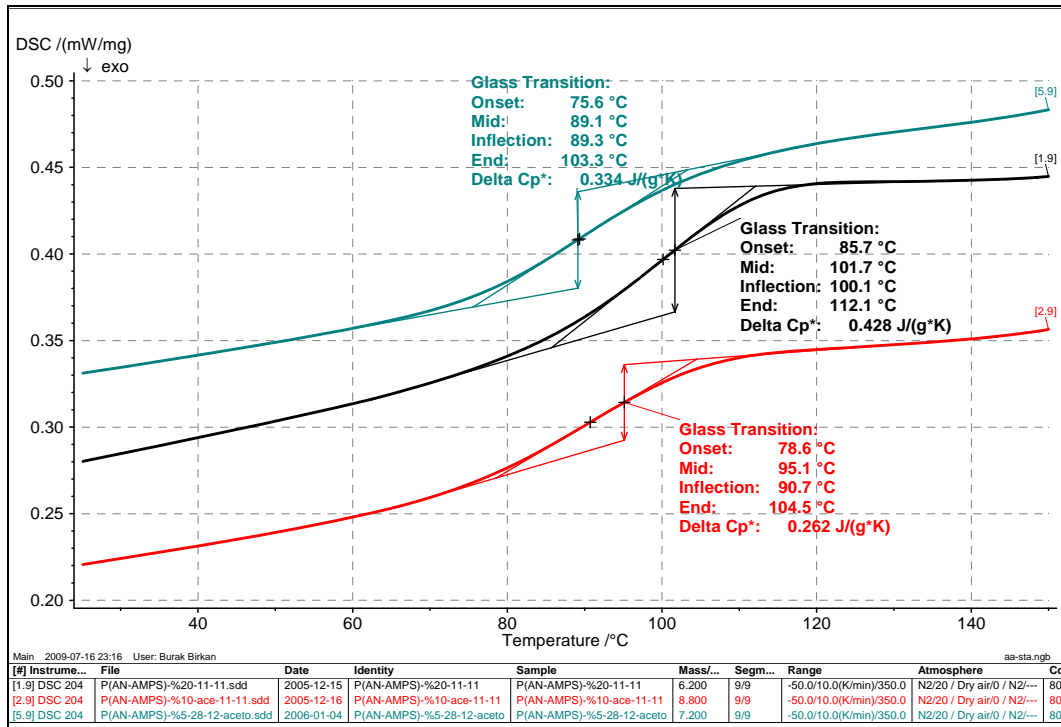


Figure 3.3-3 DSC analysis of P(AN-co-AMPS) at different AMPS concentrations

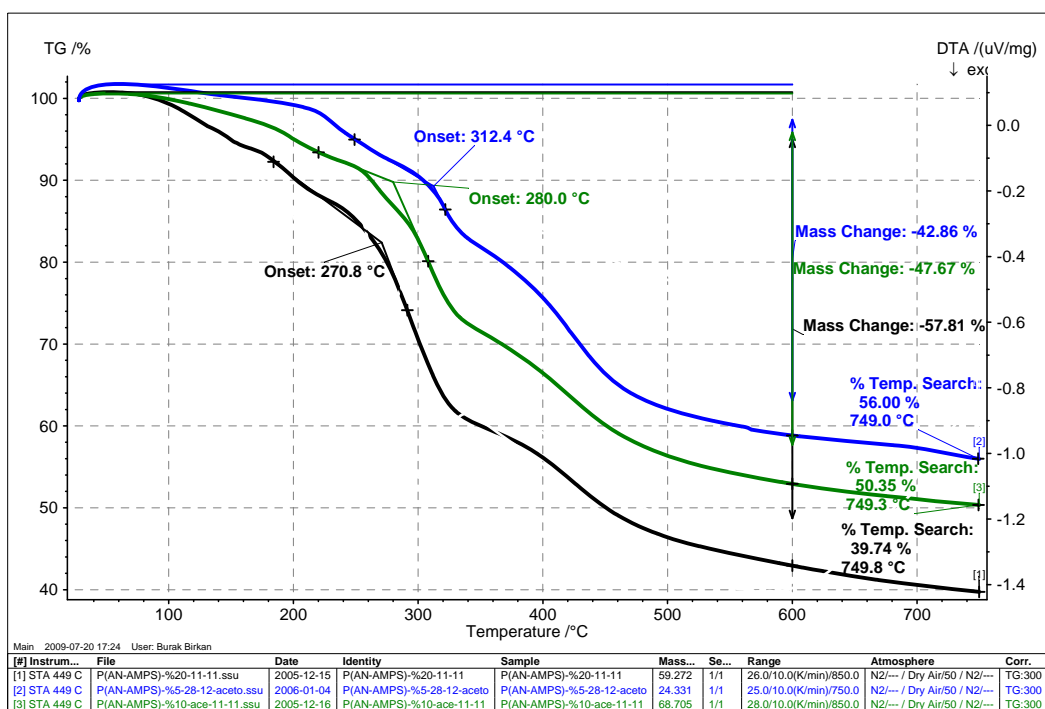


Figure 3.3-4 TGA analysis of P(AN-co-AMPS) at different AMPS concentrations from 5%, 10% and 20% from top to bottom respectively

### 3.3.2 Electrospinning characterization

Copolymer	%Functional monomer <sup>1</sup>	Metal	Metal % <sup>2</sup>	Polymer % <sup>3</sup>	Fiber diameter (nm)
P(AN-co-AMPS)	5	Pd	0.5	19.5	457±27
			1	18.7	445±72
			5	15.5	423±52
	10		16.3	170±27	
	20		17.8	233±32	

Table 3.3-2 Electrospun P(AN-co-AMPS) polymer fiber diameter. 1: Functional monomer in polymer backbone 2: Metal weight percentage with respect to polymer weight in electrospinning solution 3: Polymer weight percentage in electrospinning solution

Electrospinning of P(AN-co-AMPS) polymer solutions produced fibers of different diameters. As the fiber diameter was reduced with the increasing metal in the solution, thinner fibers were obtained (Figure 3.3-5). With increasing AMPS concentration it was also possible to handle thinner fibers (Table 3.3-2).

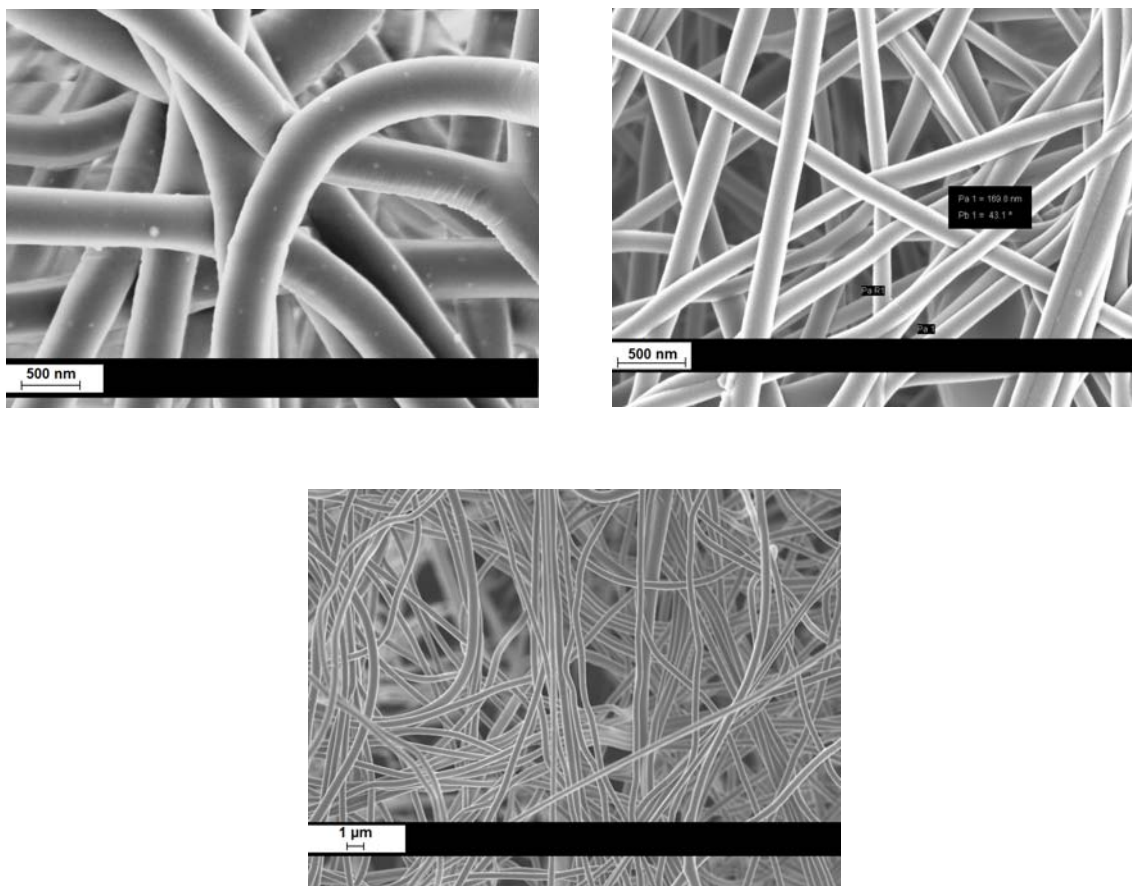


Figure 3.3-5 SEM pictures for P(AN-co-5%AMPS) at different Pd loadings a)0.5% b)1% c)5%

The surprising nature of P(AN-co-AMPS) electrospun mats was revealed during the detailed SEM analysis of fibers. Previous electrospun copolymer yielded nanoparticles on few tens of nanometers. But the nanoparticles produced on the surface of AMPS copolymers showed a distinct different behavior where particles on 5nm dimensions were observable (Figure 3.3-6).

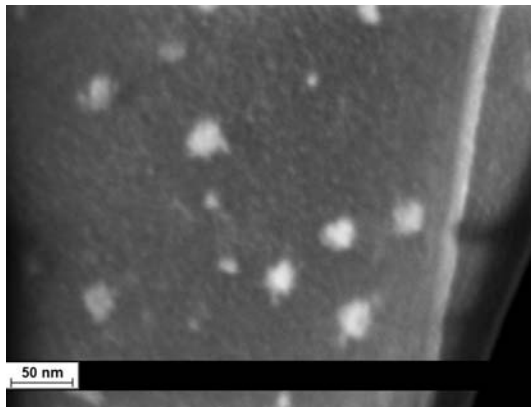
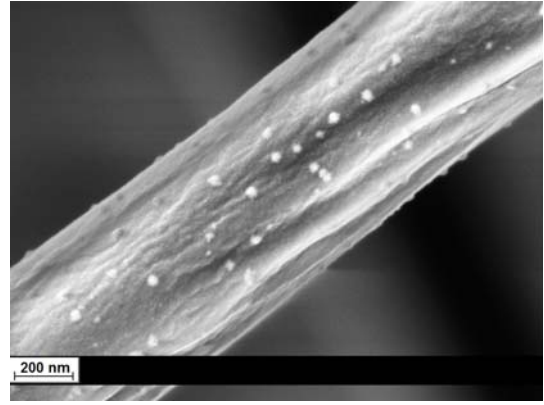
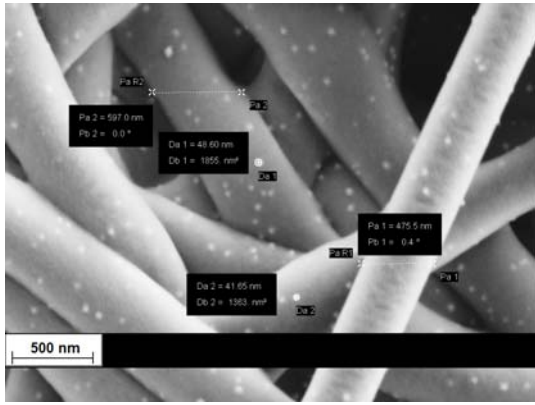
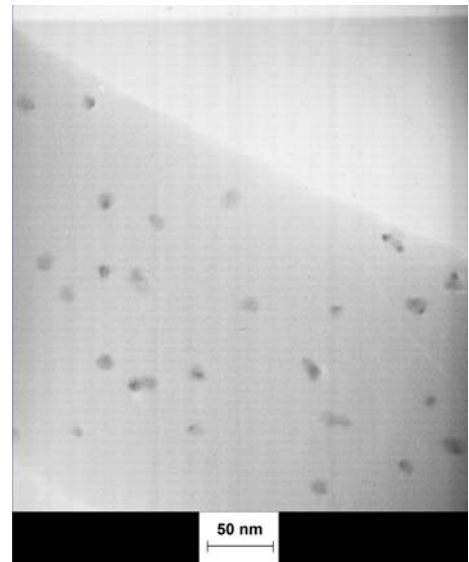
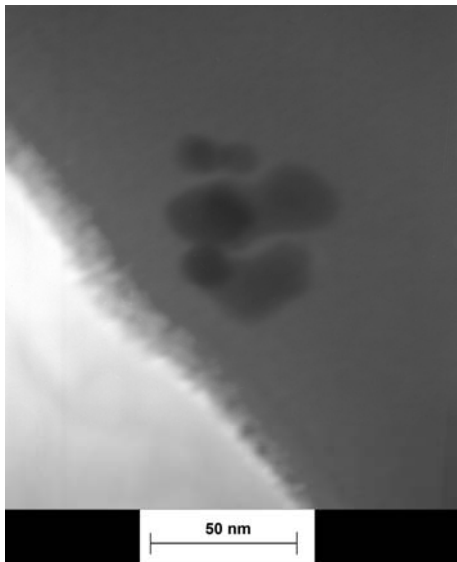


Figure 3.3-6 SEM pictures Electrospun P(AN-co-5AMPS)-5%Pd, reduced nanoparticles



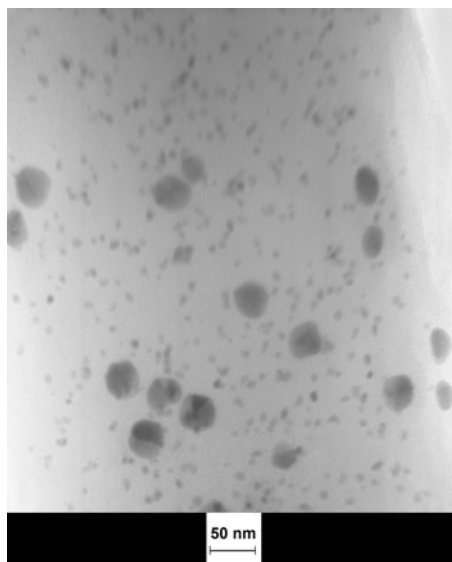
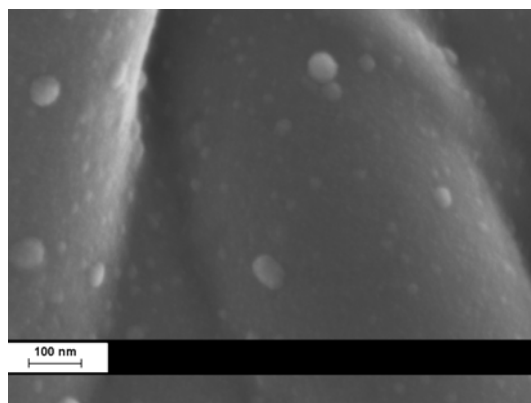
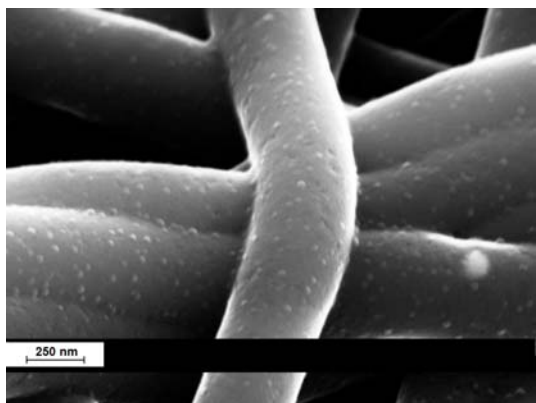


Figure 3.3-7 TEM pictures of P(AN-co-5%AMPS) at different Pd loadings a)0.5% b)1% c)5%

TEM analysis of P(AN-co-5%AMPS) copolymeric fibers at different Pd loading were shown at Figure 3.3-7. The lowest doped fibers showed a nanoparticle diameter of  $7.7 \pm 2.6$  nm but the particles were agglomerated. As the metal concentration increased to 1%, we saw a uniform distribution of nanoparticles on the order of  $10.7 \pm 2.3$  nm. The increase in metal concentration to 5% resulted in bimodal distribution of  $7.7 \pm 1.3$  nm and  $32.2 \pm 3$  nm particles. The small domain of nanoparticles showed us the nanoparticle distribution increased with metal loading. The increase in the concentration of the Pd within the polymeric fibers led the nanoparticles to distribute uniformly at the surface and also the electrostatic interaction with the polymer backbone resulted in bigger particles within the fibers due to the blocky-copolymer nature of the polymers as in the case for AA and VPA.



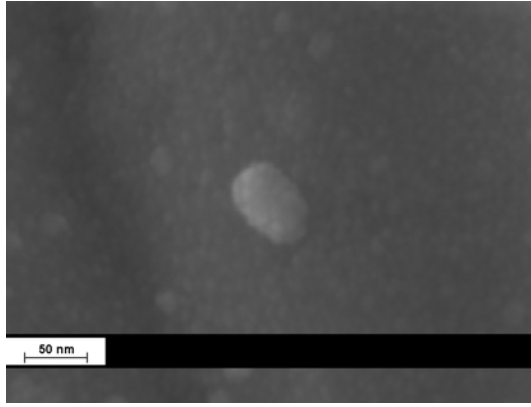


Figure 3.3-8 SEM pictures for Carbonized P(AN-co-5%AMPS)-5%Pd electrospun fibers at 600°C, different magnifications

Carbonized samples of electrospun fibers for P(AN-co-5%AMPS)-5%Pd at 600°C showed a uniform distribution of nanoparticles (Figure 3.3-8). But with the increase in temperature agglomeration of particles could not be prevented. The resulting distribution via SEM analysis showed a  $36.3 \pm 7.2$  nm particle size. Though a bimodal particle size distribution was observed for virgin untreated samples, a one dimensional increase in particle size was encountered due to the sintering of nanoparticles on high temperatures.

Coarsening is a process that occurs due to the difference in free energy between curved surfaces. In a system of dispersed particles having a range of sizes in a medium, if there is a appreciable solubility or vapor pressure the smaller particles dissolve and the larger particles grow<sup>135</sup>. The relation is given as Thompson-Freundlich equation:

$$\text{Equation 3.3-1} \quad c = c_0 \exp\left[\frac{\gamma V_m}{RT} \left(\frac{1}{r_1} + \frac{1}{r_2}\right)\right]$$

Where  $c$  is the solubility,  $c_0$  the equilibrium solubility,  $\gamma$  surface energy (reversible work),  $V_m$  the molar volume,  $r$  is the particle diameter.

The thermodynamic driving force of sintering is the reduction of the total interfacial energy. However, in terms of kinetics, the differences in bulk pressure, vapor pressure and vacancy concentration due to interface curvature induce material transport. The diffusion mechanism is related to the movement of atoms under a difference in vacancy concentration. Atom movement itself may be interpreted physically in two

ways: namely, atom movement as a result of vacancy diffusion under a difference (gradient) in vacancy concentration and movement of the atoms themselves under a difference (gradient) in stress.

In terms of vacancy movement, the vacancy flux,  $J_{vac}$ , is expressed as

$$\text{Equation 3.3-2} \quad J_{vac} = -\frac{D_v C_{v,\infty} V_m'}{RT} (\Delta P) \frac{1}{L}$$

Where  $D_v$  is the vacancy diffusion coefficient,  $C_v$  the vacancy concentration per unit volume,  $C_{v,\infty}$  the equilibrium vacancy concentration in the material with a flat surface, and  $L$  the diffusion distance. In terms of atom movement, the atom flux  $J_{atom}$  is expressed as

$$\text{Equation 3.3-3} \quad J_{atom} = -C_a B_a \nabla(\mu_a - \mu_v)$$

Where  $C_a$  is the atom concentration per unit volume,  $B_a$  the atom mobility,  $\mu_a$  the chemical potential of the atom and  $\mu_v$  the chemical potential of the vacancy

### 3.4 Poly(acrylonitrile-co-n-vinyl pyrrolidinone), P(AN-co-VPYR)

Previously synthesized polymers were all tend to template the nanoparticle production within the polymeric fibers. Generated nanoparticles were seen within the polymer surface on the order of different nanometer scales. As P(AN-co-20%AA) fibers provided Pd metal particles up to  $96\pm 8.3$  nm, we could reduce the particle size to  $87\pm 9.4$  nm with VPA copolymers. FT-IR spectrum of electrospun P(AN-co-VPA) copolymers showed shift of phosphonic acid group stretching bands which were thought to be due to the electrostatic interaction with Pd metal nanoparticles. The increased thermal properties of VPA copolymers with respect to AA copolymers also implied to use these fibers on high temperature applications, but the melting behavior of fibers on stabilization cycles during the heat treatments prohibited their use. As we moved towards we obtained at least sub 10nm particles with AMPS copolymers. TEM pictures revealed particles on 7nm range but increasing with Pd concentration. Heat treatment also boosted the particle size from a 2 dimensional distribution of  $7.7\pm 1.3$  nm and  $32.2\pm 3$  nm to a 1 dimensional  $36.3\pm 7.2$  nm on  $600^{\circ}\text{C}$ .

The search for a polymer, which could enhance the particle synthesis on nanometer scale by preventing agglomeration and providing uniformity, had been a continuing issue. Literature studies showed PVP was used for inhibiting agglomeration and control of nanoparticle size<sup>35-37</sup>.

This section of this thesis shows the function of Poly(acrylonitrile-co-n-vinyl pyrrolidinone) copolymer for the use of nanoparticle synthesis. Starting from the polymer characterization, electrospinning and nanoparticle characterization were discussed in detail.

Cyclic voltammetry showed the feasibility of the use of nanoparticles for fuel cell applications on aim of the improvement of the catalyst utilization and lowering the catalyst loading by uniformly distribution of metal nanoparticles on carbonized nanofibers.

### 3.4.1 Polymer Characterization

Copolymer	Comonomer in feed (% mol)	Comonomer in polymer backbone (% mol)	Reactivity ratio ( $r_1/r_2$ )	Yield (%)
P(AN-co-VPYR)	2.5	5	AN/VPYR	48.7
	5.5	10	=	51.6
	13	20	0.46/0.06	66.4

Table 3.4-1 Synthesis of Poly(AN-co-AMPS)

Poly(AN-co-VPYR) copolymer was synthesized by solution polymerization of AN with VPYR in DMF solvent at 80°C for 24h. 5, 10 and 20 mole % VPYR containing reactions were run. AIBN was used as addition polymerization initiator at a concentration of 0.1 mol % relative to total mol number of AN and AA. The product was precipitated at methanol and the yield changed from 66.4% to 48.7% (Table 3.4-1). The monomer feed in VPYR was selected according to the reactivity ratios calculated from NMR characterization results of the prior syntheses.

#### 3.4.1.1 FT-IR characterization

Previously FT-IR analyses showed if there was an electrostatic interaction of polymer with metal ion, it could be noticed from the change in the absorption frequencies of the interacting groups within the side chain. For VPYR copolymers Figure 3.4-1 demonstrated the change in the stretching frequency of the  $-C=O-$  carbonyl group at the side chain of VPYR copolymer. After  $PdCl_2$  addition the band at  $1673\text{ cm}^{-1}$  shifted to  $1667\text{ cm}^{-1}$  and after reduction of salt to metallic Pd the peak restored to  $1670\text{ cm}^{-1}$ . The case was almost the same for  $PtCl_2$  (Figure 3.4-2). With the increase in metal concentration within the polymer, carbonyl band shifted from  $1673\text{ cm}^{-1}$  to  $1659\text{ cm}^{-1}$ . As the metal concentration increased to 20%, carbonyl band broadened and shifted to smaller wavenumbers for reduced metallic fibers.

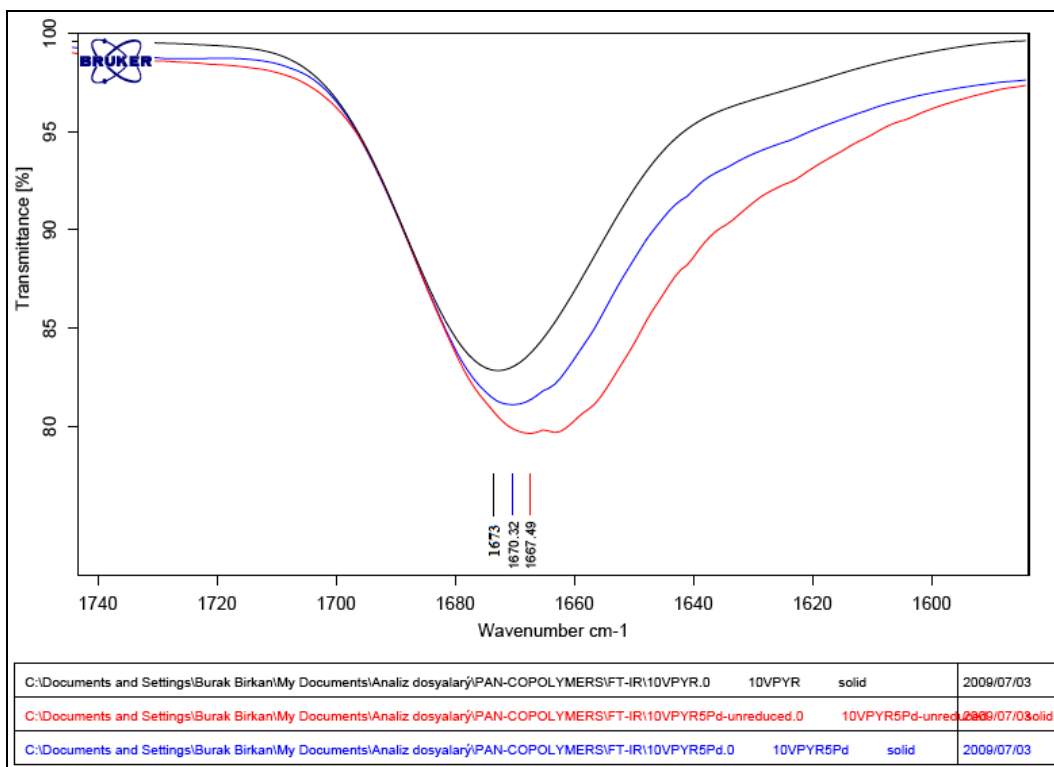


Figure 3.4-1. FT-IR spectrums of P(AN-co-10%VPYR)-5%Pd, before and after reduction of PdCl<sub>2</sub>

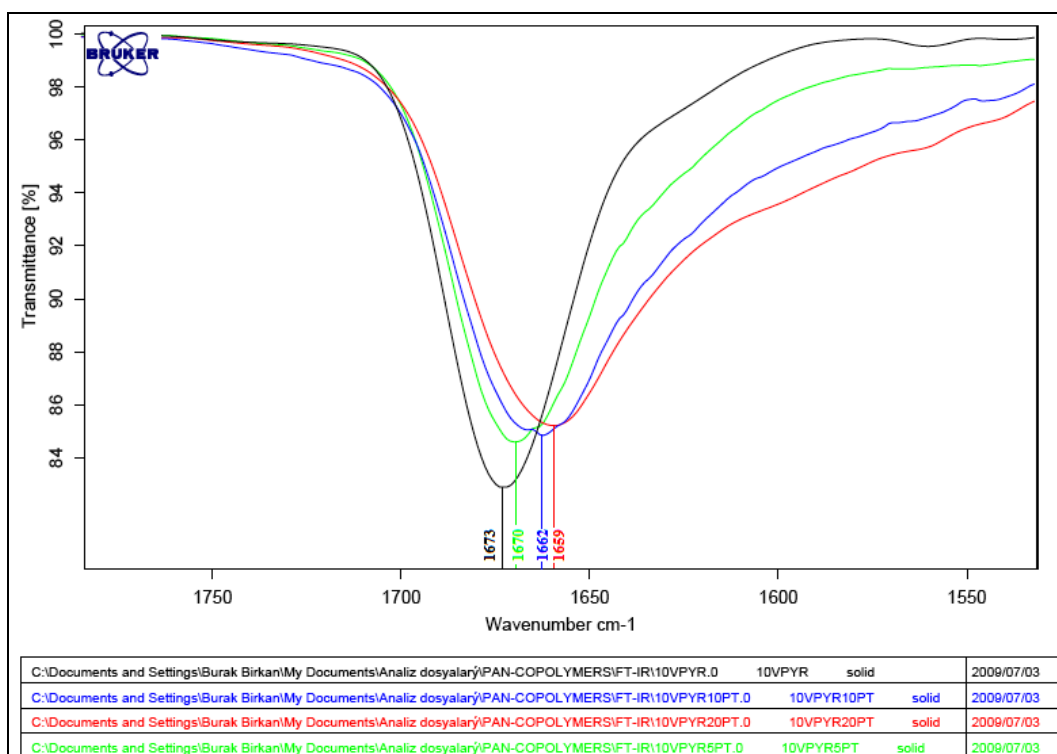


Figure 3.4-2 FT-IR spectrums of P(AN-co-10%VPYR)-Pt, increasing Pt concentration

### 3.4.1.2 NMR characterization

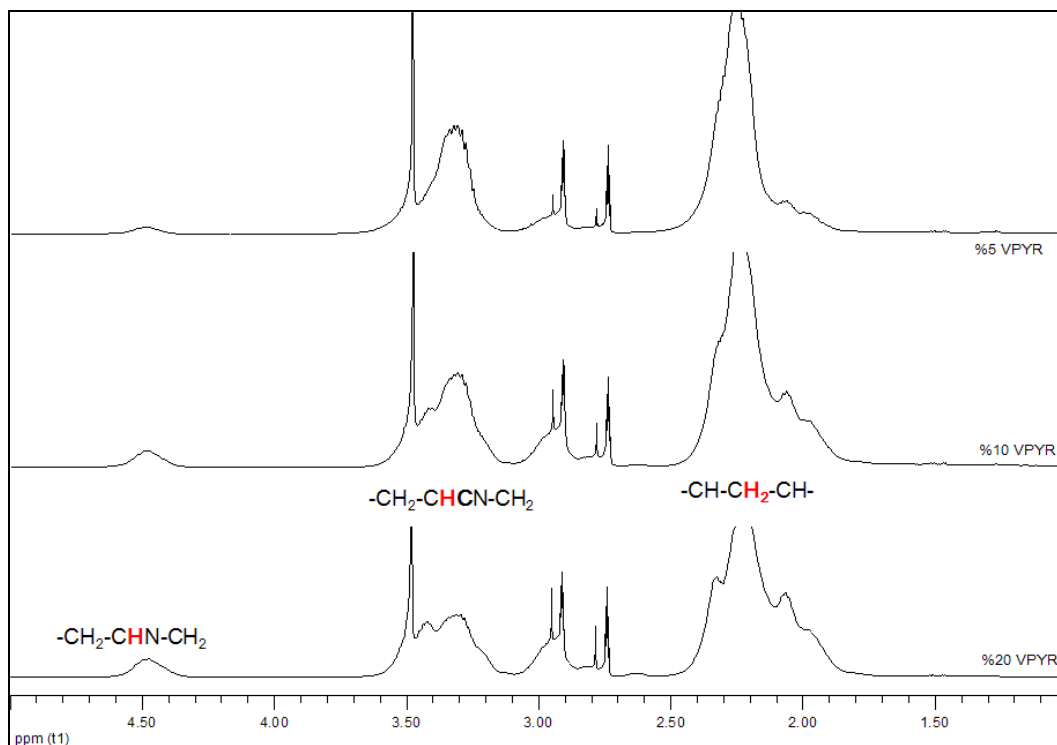


Figure 3.4-3. <sup>1</sup>H NMR spectrums of P(AN-co-VPYR) at different VPYR concentrations from 5%, 10% and 20% from top to bottom respectively

<sup>1</sup>H NMR spectrum was fully representative that the reactions occurred successfully. The signals were assigned as shown in Figure 3.4-3. The characteristic proton peaks for P(AN-co-VPYR) in <sup>1</sup>H-NMR (recorded in DMSO-d<sub>6</sub>) were 4.50 ppm (-CH<sub>2</sub>-CH(N)-CH<sub>2</sub>-), 3.3 ppm (-CH<sub>2</sub>-CHCN-CH<sub>2</sub>-), 2.9 ppm (-N-CH<sub>2</sub>-CH<sub>2</sub>-), 2.2 ppm (-CHCH<sub>2</sub>-CH-). Reactivity ratios were in well agreement with Brar's work<sup>136</sup>. They determined the composition of the copolymers using NMR spectra by Kelen-Tudos method. The calculated reactivity ratios (0.46/0.06; AN/VPYR-Table 3.4-1) showed that the polymer structure was mainly a random copolymer.

### 3.4.1.3 Thermal Characterization

DSC analysis of VPYR copolymers showed an increase in glass transition temperatures  $T_g$  from 115.5°C to 121.5°C as the VPYR content within the polymer was increasing (Figure 3.4-4).

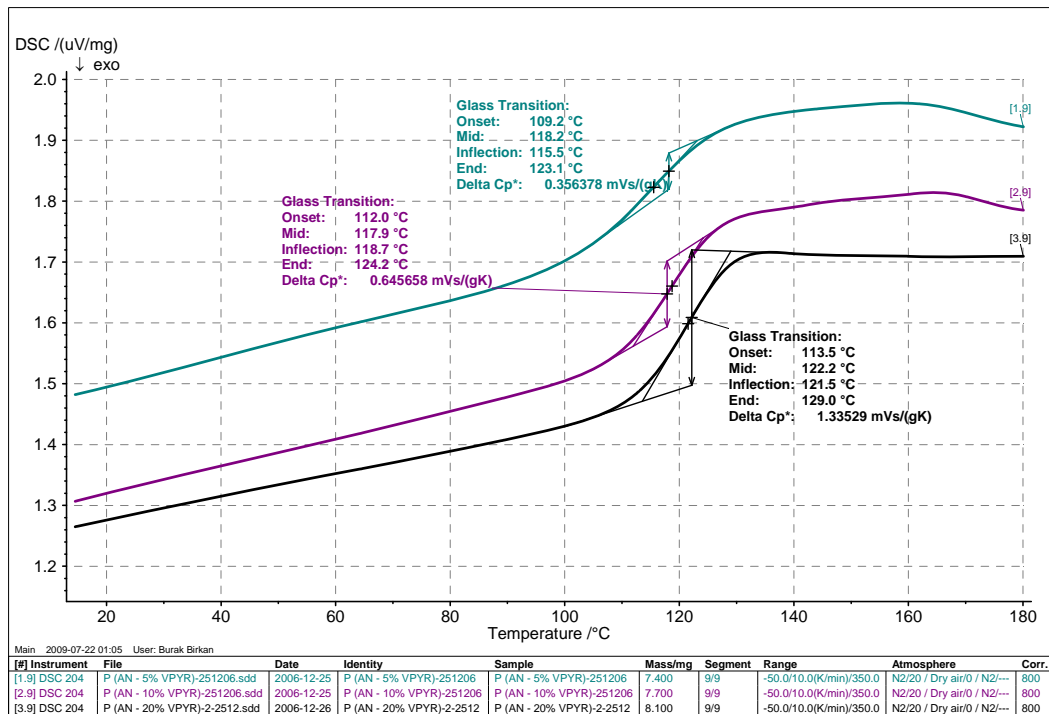


Figure 3.4-4 DSC analysis of P(AN-co-VPYR) at different VPYR concentrations

The detailed thermal analysis of electrospun fibers prior reducing the metal salt and also after metallization of fibers was also performed. Table 3.4-2 showed that after spinning of polymer solutions  $T_g$  values showed a decrease with respect to 10% and 20%VPYR copolymers. For both Pd and Pt metal doped samples the same trend was observed. By increasing the metal concentration  $T_g$  values approached back to its initial values. The decrease in  $T_g$  suggested that there was an increase in the segmental mobility of the polymer chains within the nanofibers<sup>137, 138</sup>.

But after reducing the nanoparticles electrospun fibers  $T_g$  values showed a sharp rise with increasing metal concentration. The metallized electrospun fibers became composite hardened and the produced metal nanoparticles hindered the flow of

polymeric fibers on top of each other and restrained mobility of polymer chains, therefore an increase in  $T_g$  was observed.

% Copolymer	Metal content	$T_g$ of VPYR copolymer (°C)	$T_g$ after spinning (°C)	$T_g$ after reducing (°C)
%10 VPYR	5%Pd	118.7	97.1	121.9
	10%Pd		110.1	124.5
	20%Pd		114.5	125.1
	5%Pt		111.3	125.5
	10%Pt		115.3	135.9
	20%Pt		118.3	141.5
%20 VPYR	5%Pd	121.5	101.7	126.5
	10%Pd		111.2	127.8
	20%Pd		115.5	130.2
	5%Pt		113.3	127.9
	10%Pt		115.9	137.3
	20%Pt		119.1	144.7

Table 3.4-2 Glass transition temperature analyses for VPYR copolymers

Thermogravimetric analysis of samples shows that P(AN-co-VPYR) copolymers were thermally stable up to 278°C. The delayed degradation temperature with increasing VPYR concentration enabled a perfect stabilization and carbonization mechanism for P(AN-co-VPYR) copolymers for the production of CNF's (Figure 3.4-5).

Stabilization process which was carried out in air (oxidative stabilization) constituted the first and very important operation of the conversion of the PAN fiber precursor to carbon fiber<sup>139-142</sup>. During stabilization, the precursor fiber was heated to a temperature in the range of RT-200°C. Because of the chemical reactions involved, cyclization, dehydrogenation, aromatization, oxidation and crosslinking might occur and as a result of the conversion of C≡N bonds to C=N bonds a fully aromatic cyclized

ladder type structure formed (Figure 3.4-6). This new structure was thermally stable. Also, it had been reported that during stabilization,  $-CH_2$  and  $-CN$  groups disappeared while  $C=C$ ,  $C=N$  and  $=C-H$  groups formed<sup>143</sup>.

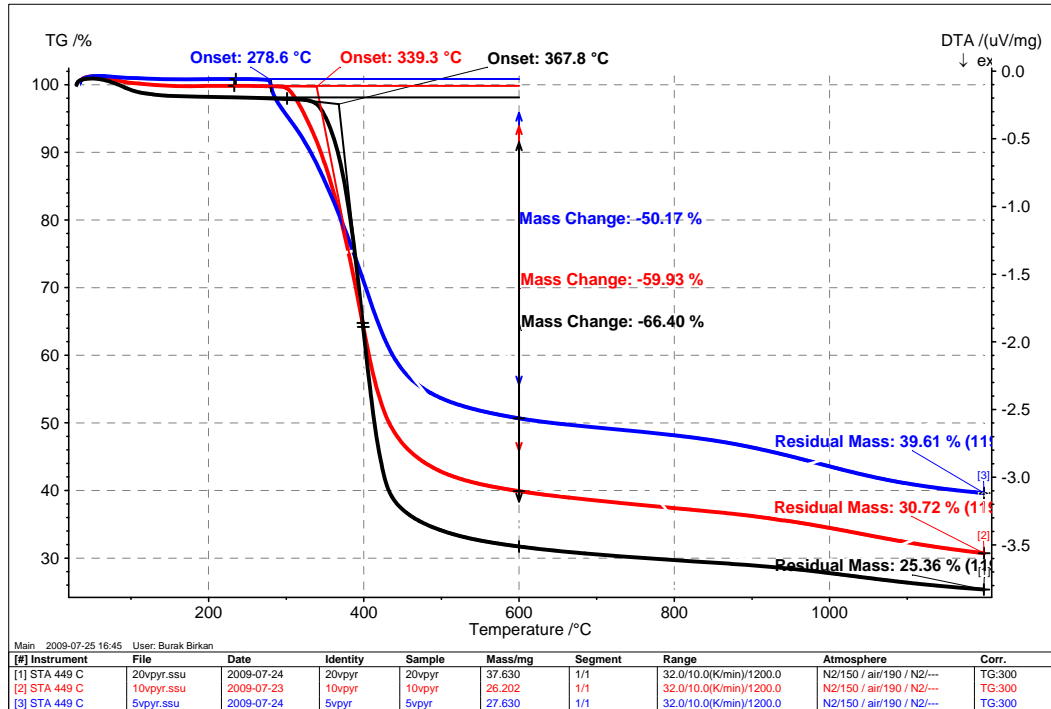


Figure 3.4-5. TGA analysis of P(AN-co-VPYR) at different VPYR concentrations from 5%, 10% and 20% from top to bottom respectively

At the same time the color of precursor fiber changes gradually and finally turned black when carbonized. Research showed that optimum stabilization conditions led to high modulus carbon fibers. Too low temperatures led to slow reactions and incomplete stabilization, whereas too high temperatures could fuse or even burn the fibers.

It was believed that during the early stages of carbonization at 500°C or lower, the stabilized nanofibers probably underwent further cyclization in the uncyclized portion, forming ladder structure, crosslinking, and some chain-scission reaction, while evolving hydrogen, water, carboxylic acids and other volatiles. When the temperature was between 500°C and 700°C, the carbon basal planes from the aromatized structure in the stabilized nanofibers began to form and increase in size. As these reactions and structure rearrangements occurred within the nanofibers, consolidation and densification occurred. When the temperature was over 700°C, condensation reactions between heterocyclic rings and the resulting evolving gases of HCN, N<sub>2</sub> etc., were dominant<sup>144</sup>.

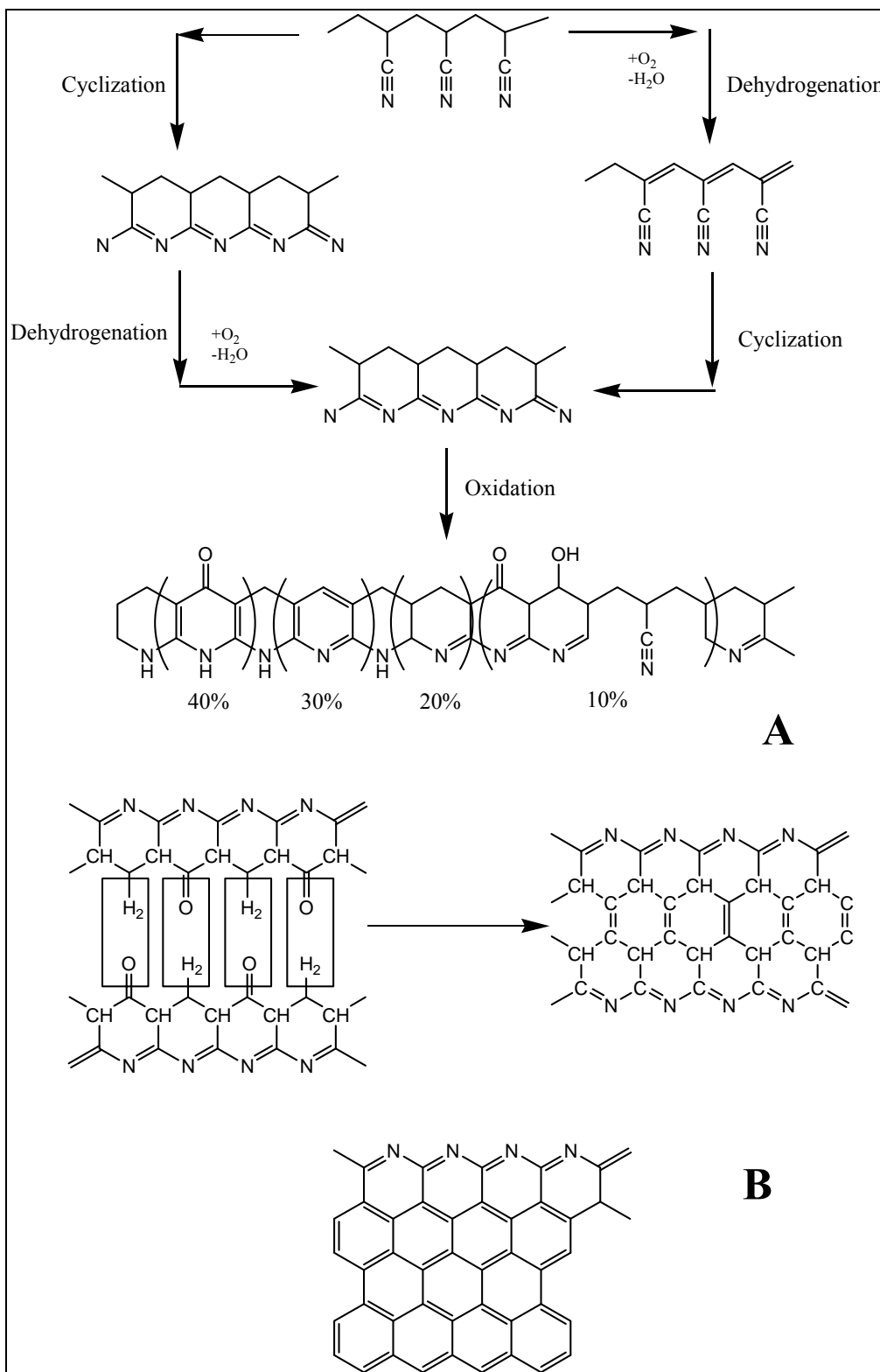


Figure 3.4-6. Diagram of the molecular changes occurring during the chemical process of stabilization and carbonization of PAN, (a) the stabilization step, which occurs between 180-300°C in air environment. (b) The carbonization step. Shown in (b) is the mechanism of intermolecular cross-linking between 600-1500°C through oxygen-containing groups, however, dehydrogenation is a possible mechanism as well<sup>145</sup>.

### 3.4.2 Electrospinning

During the electrospinning of P(AN-co-VPYR) polymer solutions were prepared to get maximum fiber density and minimum fiber diameter during the process. The spinning parameters were optimized via applied voltage, concentration of the solution and tip to metal collector distance. Throughout electrospinning process, different fiber diameters and morphologies were attained due to different solution viscosities, surface tensions and conductivities.

Fiber diameters of P(AN-co-VPYR) were illustrated in Table 3.4-3. In general, fiber diameters were changed via copolymer type and ratio, solution viscosity (concentration) and metal ratio. As the weight percentage of metal increased for the same concentration, the fiber diameter decreased. Higher metal salt concentration enhanced the solution conductivity (also viscosity) which led thinner fiber formation<sup>55</sup>. Xiongli Xu found that the average diameters of the ultra-fine gelatin fibers electrospun with increasing AgNO<sub>3</sub> wt% in the solution from 0.1% to 4%, decreased from 150 nm to 90 nm, respectively, which are dependent on the conductivity of the gelatin solutions<sup>90</sup>. Qian Zhang came up with the same result in ultra-fine polyimide (PI) fibers containing Ag nanoparticles. The average diameters of the PI fibers with different amounts of AgTFA, in which Ag were 0, 1, 2, and 7 wt.%, were 200, 190, 180, and 60 nm, respectively<sup>86</sup>.

Copolymer	%Functional monomer <sup>1</sup>	Metal	Metal % <sup>2</sup>	Polymer % <sup>3</sup>	Fiber diameter (nm)	
<b>P(AN-co-VPYR)</b>	5	Pd	0.5	20	238±41	
			1	20	505±110	
			5	20	853±137	
			10	12	451±113	
			20	10	358±73	
	10		0.5	20	185±21	
			1	20	210±19	
			5	20	302±54	
			10	15	199±32	
			20	12.4	143±42	
	20		0.5	20	269±42	
			1	18.8	145±21	
			5	20	451±97	
			10	15	183±30	
			20	15	209±51	
	5		Pt	5	15	412±26
				10	15	352±44
				20	15	284±73
	10			5	13.5	222±21
				10	15	330±36
				20	15	204±24
	20			5	13.5	205±27
				10	15	187±34
				20	15	177±29

Table 3.4-3 Electrospun P(AN-co-VPYR) polymer fiber diameter. 1: Functional monomer in polymer backbone 2: Metal weight percentage with respect to polymer weight in electrospinning solution 3: Polymer weight percentage in electrospinning solution.

Depending on polymer solution concentrations, average fiber diameters were obtained in different diameter from 150 nm to 850 nm (Figure 3.4-7). It was confirmed that the change in fiber diameter is related to the solution concentration<sup>146</sup>. However, lower solution concentration, in other words, lower solution viscosity, led the formation of beads<sup>53</sup>. In order to get smooth connected fiber, bead formation was undesired in this research so, the polymer solution concentration was controlled in the range of 12 to 20 % weight percentage.

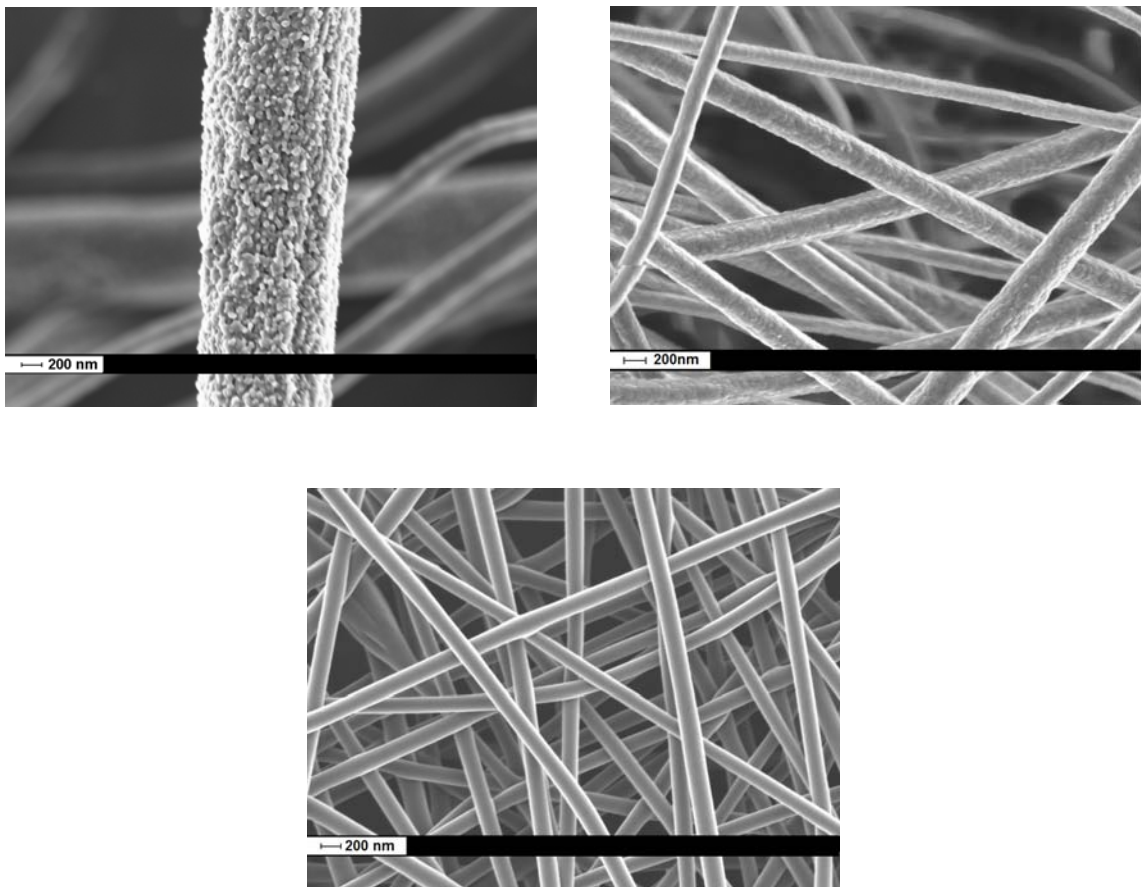


Figure 3.4-7. SEM pictures for P(AN-co-5%VPYR), different solution concentrations, 20%, 15% and 12% respectively.

### 3.4.3 Reduction of metal salts

Two strong reducing agent, hydrazine and sodium borohydride were compared as mentioned in section 2.5 for reducing metal salts electrospun with polymers. XRD and EDX analysis showed that metal precursors could be successfully reduced into metallic forms and no excess metal salt remained after carbonization cycles. If same concentrations were used, smaller metal crystalline sizes could be obtained by using dilute hydrazine as a reducing agent. In Figure 3.4-8 XRD spectrum of P(AN-co-5%VPYR)- 5%-Pt was depicted for evaluation of the reducing agent effect. Wider peaks indicated smaller diameter particles and the crystalline size of the particles were measured quantitatively by Debye-Scherrer formula as described before in section 2.7.1.

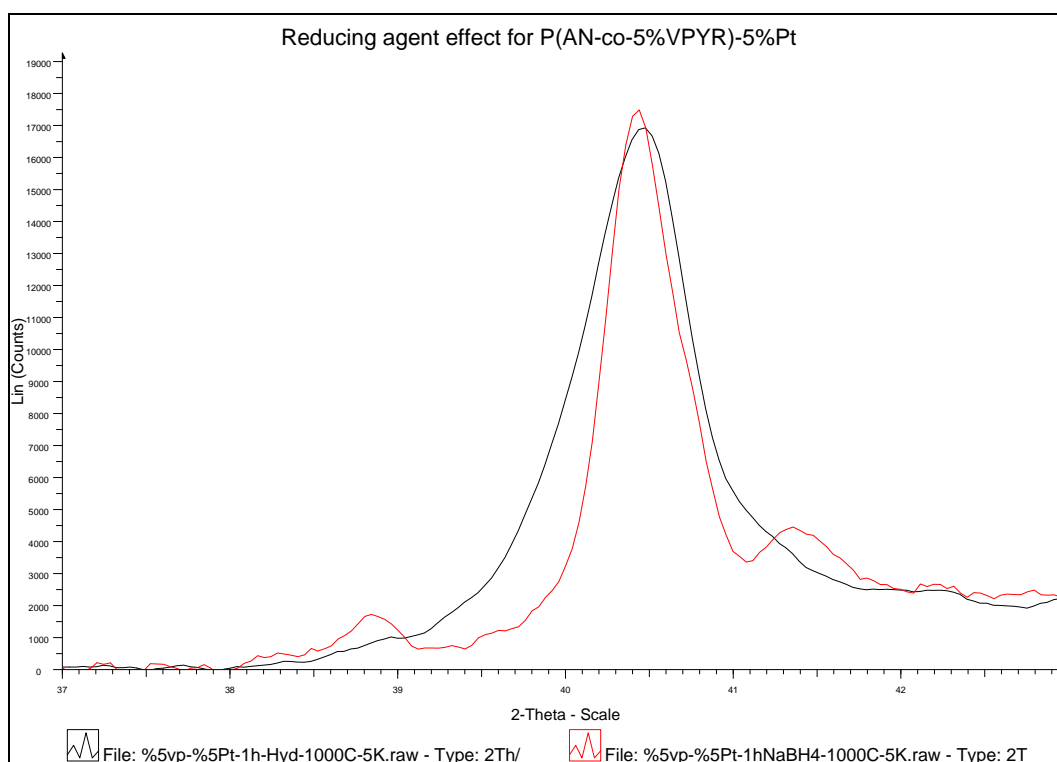


Figure 3.4-8 XRD analysis for P(AN-co-5%VPYR)-5%Pd, different reducing agents

Comparisons of the reduction agents were tabulated in Table 3.4-4 for polymers P(AN-co-5%VPYR)- 5%-Pd and P(AN-co-5%VPYR)-5%-Pt. It could be seen that by using hydrazine as a reducing agent smaller nanoparticles could be obtained rather than NaBH<sub>4</sub>. Moreover, concentrated reducing agent solutions enlarged the nanoparticle crystalline size. Therefore, dilute hydrazine solutions were used in all reducing reactions for Pd and Pt.

Metal	Reducing agent	Time (h)	Concentration	Fwhm ( $\theta$ )	Nanoparticle crystal size (nm)
Pd	Hydrazine	1h	Concentrated	0.325°	26.01 nm
			Dilute	0.379°	22.31 nm
	NaBH <sub>4</sub>			0.327°	25.85 nm
Pt	Hydrazine	1h	Dilute	0.721°	11.72 nm
		24h		0.625°	13.53 nm
	NaBH <sub>4</sub>	1h		0.457°	18.49 nm

Table 3.4-4. XRD spectrum analyses for different reducing agents

### 3.4.4 Nanoparticle characterization

Polymer	Temperature (°C)	Heating rate (°C)	Isothermal (min)	Fiber diameter (nm)	Average particle size (nm)
P(AN-co-%5-VPYR), 5%Pd	600	0.1	30	390	5.1±0.8 38.8±11.5
	600	1	30	450	4.8±1.1 32.7±6.07
	600	1	-	475	4.7±0.8 28.6±4.9
	600	5	-	540	<4 21.2±3.2
	1200	1	30	415	36.6±10.2
	1200	1	-	420	24.7±5.0
	1200	10	-	430	17.1±5.1

Table 3.4-5 Heat treatment effect on particle size for P(AN-co-%5-VPYR), 5%Pd

In section 3.3.2 it was stated that the heat treated P(AN-co-5%AMPS)-5% nanoparticles were agglomerating with heat treatment. Therefore a detailed investigation of the heat treatment cycle on different temperatures with changing heating rates and isothermal times were needed for better understanding the thermal behavior of nanoparticles.

Sintering was the main reason for the agglomeration of metal nanoparticles within the fiber support. Reduction of the active surface area was provoked via agglomeration and coalescence of small metal crystallites into larger ones with lower surface-to-volume ratios. Two different but quite general pictures had been proposed for sintering of supported metal catalysts, i.e. the atomic migration and the crystallite migration models (Figure 3.4-9). In the first case, sintering occurred via escape of metal atoms from a crystallite, transport of these atoms across the surface of the support (or in the gas phase), and subsequent capture of the migrating atoms on collision with another metal crystallite. Since larger crystallites were more stable (the metal-metal bond energies were often greater than the metal-support interaction), small crystallites diminished in size and the larger ones increased. The second model visualized sintering to occur via migration of the crystallites along the surface of the support, followed by the collision and coalescence of two crystallites<sup>147</sup>.

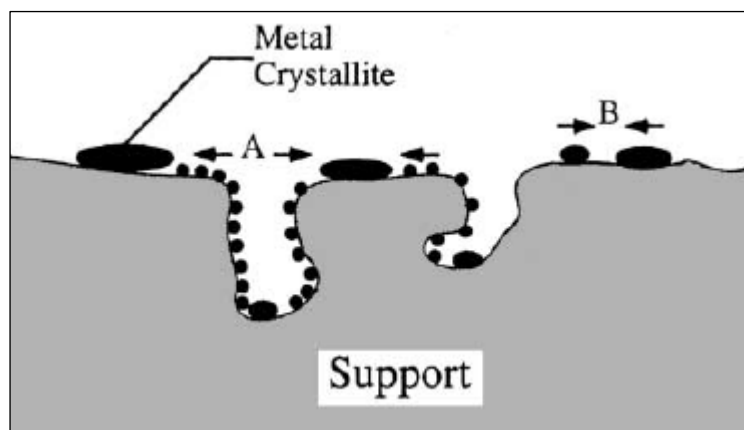


Figure 3.4-9. Two conceptual models for crystallite growth due to sintering by A) atomic migration or B) crystallite migration (courtesy of Barthalomew<sup>148</sup>)

From Table 3.4-5 we could see that by increase in carbonization temperature, particle sizes increased and SEM analysis showed that on the expense of smaller crystals larger nanoparticles were nucleating on the surface (Figure 3.4-10, Figure

3.4-11 and Figure 3.4-12). Similarly, the enlargement of the particle sizes by the change from two dimensional distributions to one dimensional distribution could also be seen.

For different heating rates, we could say that the nucleation mechanisms for nanoparticles within the fibers were faster at increased temperatures. If carbonizations were processed at higher temperatures particle sizes almost double for a tenfold change in heating rate, whereas at lower temperatures smaller particle diffusion was limited and only a change in bigger dimensioned particles was seen. With the increase in isothermal waiting time particle sizes were also increasing.

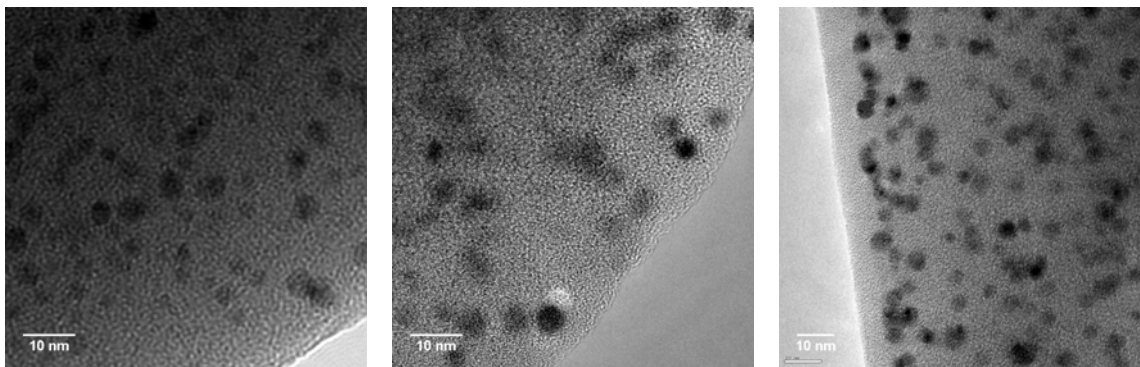


Figure 3.4-10 P(AN-co-5-VPYR)-5Pd-heating treatment effects-TEM analyses a) 600°C-0,1°C/min-30min (5.1 nm average particle size) b) 600°C -1°C /min-30min (4.8 nm average particle size) c) 600°C -1°C /min (4.7 nm average particle size)

If we look at the fiber diameters we saw almost the same behaviors with nanoparticles. With increase in temperature and decrease in heating rate, fibers shrunk due the degradation of polymers within the cyclization and carbonization mechanism.

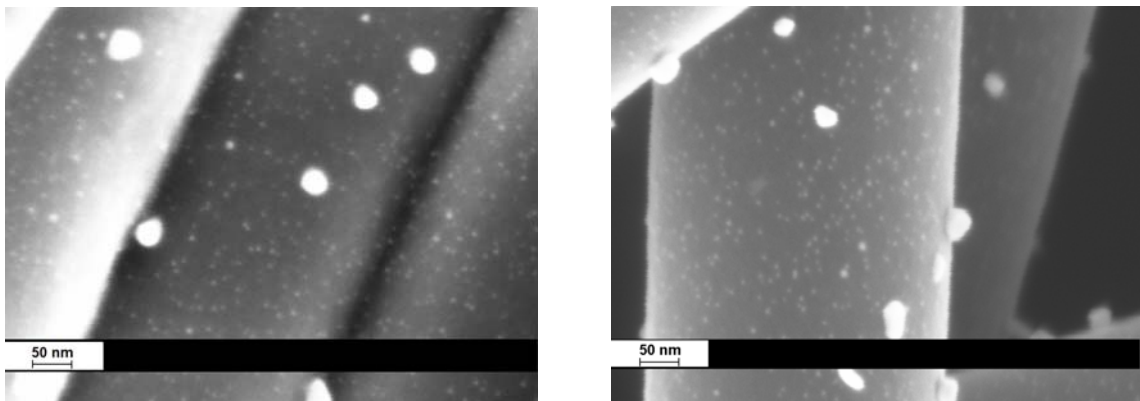


Figure 3.4-11. SEM pictures of P(AN-co-5-VPYR)-5Pd, carbonized at a)600°C -1°C /min b) 600°C -1°C /min-30min

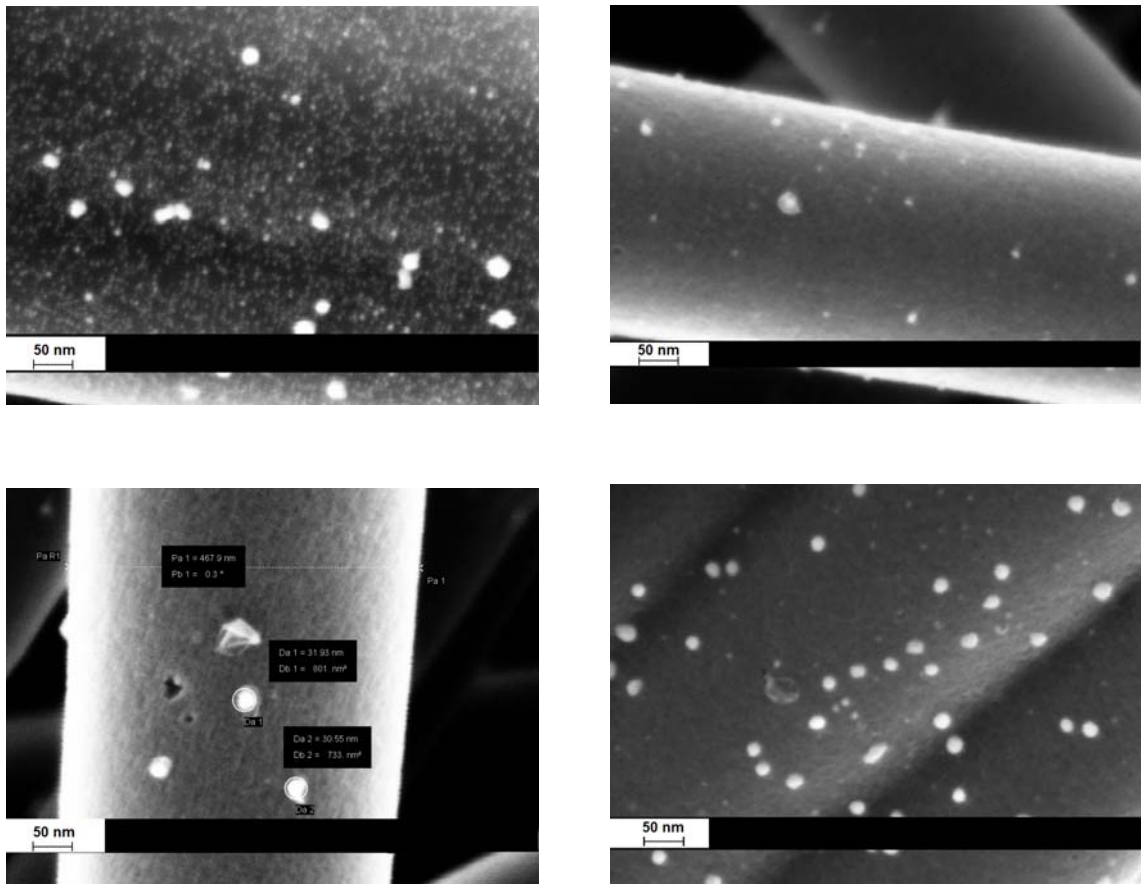


Figure 3.4-12 SEM pictures of P(AN-co-5%VPYR)-5%Pd, carbonized at a) 600°C -5°C /min b)1200°C -1°C /min c) 1200°C -1°C /min-30min d) 1200°C -10°C /min

Table 3.4-6 showed a detailed SEM analysis result for different VPYR copolymer doped with Pd and Pt and heated to 600°C at different heating rates. For a representative measurement during the SEM analysis, an average of 100 particles per sample was taken into account by using image processing programs. SEM analysis showed that there was an increase in particle sizes as metal concentration within the fiber increases. We could say that for Pd nanoparticles, a rise in metal concentration led to an enlargement in particles sizes. The sintering mechanism did not change since the bimodal distribution still persisted. But the increase in the bigger domained particles was more obvious since the probability of nucleating nanoparticles was higher if we considered a steady state diffusion mechanism. According to Fick's first law of diffusion (Equation 3.4-1) an increase in concentration that meant the mass, increased the diffusion flux, meaning an increase in nucleating mechanism might lead to a bigger particle growth.

$$\text{Equation 3.4-1} \quad J = \frac{1}{A} \frac{dM}{dt} = -D \frac{dC}{dt}$$

where J is the diffusion flux (kg/m<sup>2</sup>-s), M is the mass, A is the area and C is the concentration and D is called the diffusion coefficient.

VPYR Monomer (%)	Metal	Metal (%)	Fiber diameter (nm)	Heating rate (°C)	Average particle size (nm)
5	Pd	5	540±59	5	<4 21.2±3.2
		10	451±113		6.2±0.9 24.1±6.1
		20	358±73		6.3±1.0 28.6±4.9
		10	302±54		7.4
20	Pd	5	451±97	5	<4 29.3±2.9
5		412±26	<4		
5	Pt	10	222±21	20	6.4±0.7 4.3±0.6
		20	205±27	5	7.9±0.6
				20	5.1±0.6

Table 3.4-6. SEM analysis results for P(AN-co-VPYR) electrospun nanoparticles

If SEM analyses results were investigated, we saw that there was a discrepancy with XRD results in Table 3.4-7. By the visual analysis of samples actually the particle

sizes were tabulated during SEM analyses. But XRD analysis results showed the crystalline size of particles. The discrepancy was that for samples with smaller particles and having a dimensional distribution, XRD results deviated and overestimated the values since the resolution of Debye-Scherrer formula for particles below 4-5 nm was limited<sup>149, 150</sup> due to the overlapping of peaks and although less in number, agglomerated nanoparticles may dominate in accumulated average particle size. The case for bigger particles was vice-versa. Since bigger particles might built up by smaller crystals, this time XRD might have underestimated results. Although having these difficulties in commenting on the results, the easy use of, ability of collecting reproducible results through a nondestructive analysis method, XRD was still a powerful technique on the characterization of nanoparticles.

%Polymer	Temperature (°C)	Heating rate (°C)	Crystal size (nm)					
			Weight % of Pd			Weight % of Pt		
			5%	10%	20%	5%	10%	20%
%5VPYR	600	5	5.6	7.2	10.0	6.9	10.9	13.2
		40	5.2	5.6	9.8	6.1	9.7	9.8
	1000	5	18.9	31.1	33.8	11.0	18.7	28.5
		40	13.8	20.4	24.3	10.7	14.3	17.6
%10VPYR	600	5	7.4	7.7	10.4	8.8	12.8	16.7
		40	5.6	7.0	8.7	8.2	11.5	11.4
	1000	5	22.2	27.9	35.6	13.7	21.5	29.3
		40	16.6	23.3	25.2	12.1	17.6	19.8
%20VPYR	600	5	7.4	8.4	10.3	10.7	13.6	19.7
		40	6.6	7.8	8.9	6.4	13.1	17.8
	1000	5	26.6	31.0	37.7	17.3	24.4	30.5
		40	16.8	23.9	32.0	15.5	18.6	26.3

Table 3.4-7 XRD analysis results for heat treated VPYR copolymer

Table 3.4-7 represented the detailed analysis of crystalline sizes for different VPYR containing copolymers. Copolymers were electrospun with different metal

concentrations and heat treated at two selected temperatures by two different heating rates.

Previous results in sections 3.1, 3.2 and 3.3 showed us by increasing metal concentration within the polymer solution resulting crystalline size increase. For both Pd and Pt cases at different VPYR copolymers, an increase in metal concentration from 5% to 20% enlarged crystalline sizes (Figure 3.4-13). At higher metal concentrations, nanoparticles became irregular and non-spherical which was attributed to the massive metal migration and aggregation. The migration and aggregation of nanoparticles were driven largely by the instability of metal atoms due to their high surface free energy. Their aggregation would produce thermodynamically stable particles with bigger sizes.

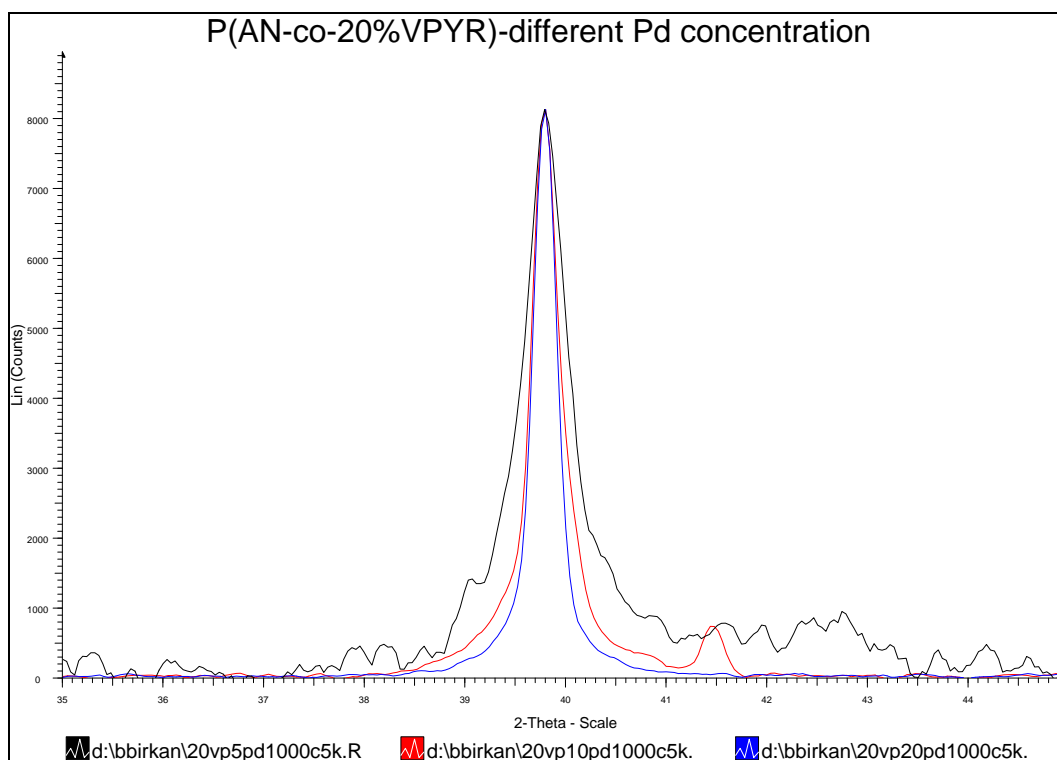


Figure 3.4-13 XRD spectrum of P(AN-co-VPYR)-5%Pt, different Pd content

By the rise in carbonization temperature, an increase in the crystalline sizes was observed. A shift of temperature from 600°C to 1000°C affected nanoparticles sizes differently. For Pd metal nanoparticles the change in size was dramatic with respect to Pt case (Figure 3.4-14 and Figure 3.4-15). Particles sizes almost tripled from sub 10 nm's whereas for Pt the growth rate was slower.

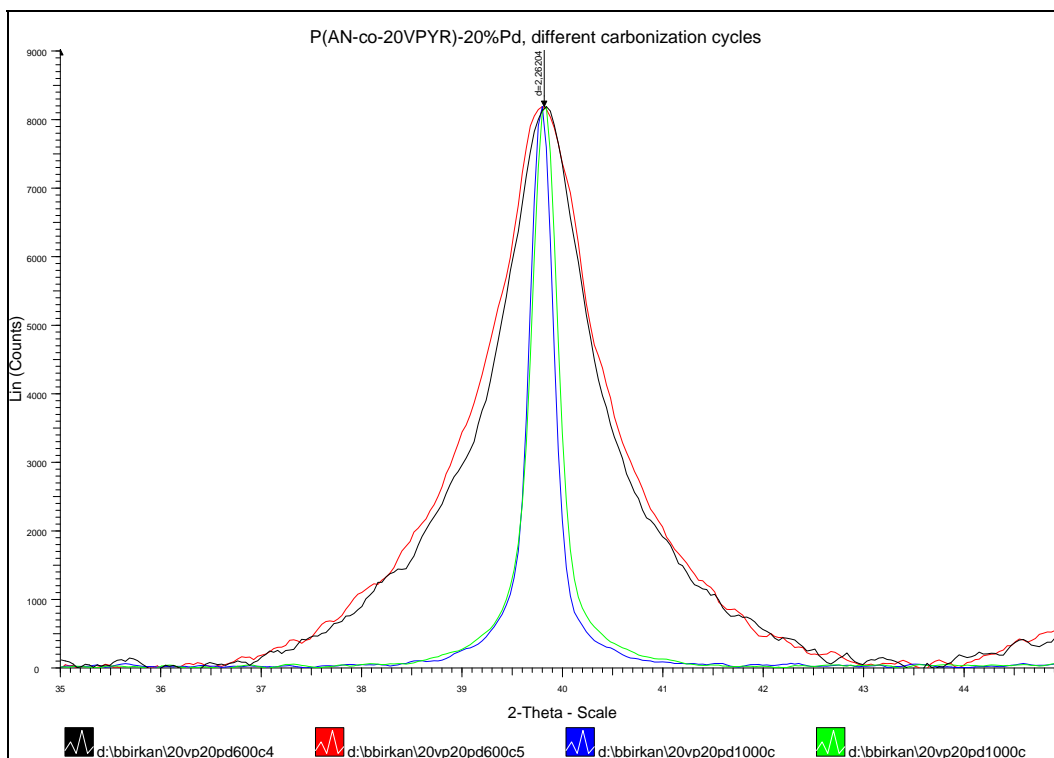


Figure 3.4-14 XRD spectrum of P(AN-co-20%VPYR)-20%Pd-effect of different carbonization cycles on crystalline size

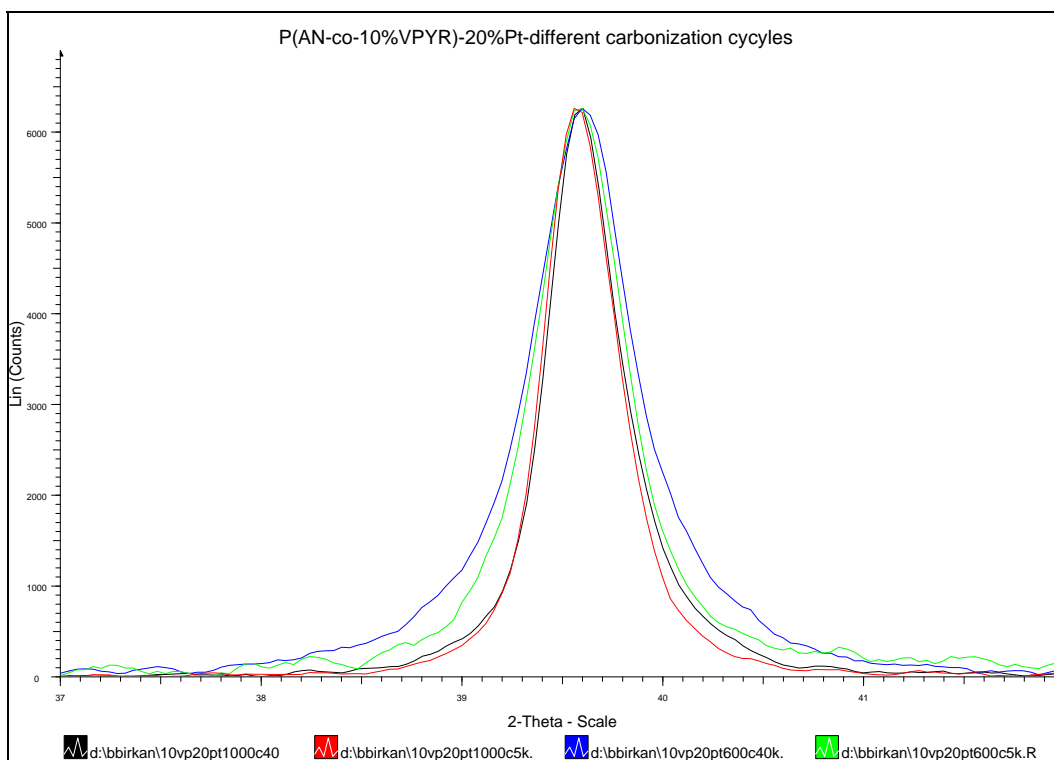


Figure 3.4-15 XRD spectrum of P(AN-co-10%VPYR)-20%Pt-effect of different carbonization cycles on crystalline size

The increase in crystalline size could be explained by the higher diffusion constants at higher temperatures due to the decreased activation energy. Equation 3.4-2 stated that the diffusion coefficient was temperature dependent.

$$\text{Equation 3.4-2} \quad D = D_0 \exp\left(-\frac{Q_d}{RT}\right)$$

Where,  $D_0$  is a temperature independent preexponential ( $\text{m}^2/\text{s}$ ),  $Q_d$  is the activation energy for diffusion ( $\text{J/mol}$  or  $\text{eV/atom}$ ),  $R$  is the gas constant and  $T$  is the temperature

The difference between Pd and Pt cases resulted from their difference in melting points. The melting temperature for Pd is  $1552^\circ\text{C}$  and  $1772^\circ\text{C}$  for Pt. The activation energy was smaller and thus diffusion coefficient was larger in Pd nanoparticles rather than Pt nanoparticles due to lower melting point. Since the crystalline growth was a diffusion controlled process therefore a higher rate of increase in Pd particles size with increasing temperature was expectable.

One of the other main points in Table 3.4-7 was that, for the nanoparticles at low temperatures, at  $600^\circ\text{C}$ , Pt nanoparticles were larger than Pd nanoparticles. This situation could not be described by governing diffusion mechanism proposed at high temperatures. During the reduction step, the localization of Pd particles within the electrostatic interaction of polymer side chain thought to be more effective than the case for Pt particles, due to the better stabilization of interfacial energy. That meant that the surface energy of Pd atoms might had been more delocalized and thus smaller particles could be formed rather than those of Pt nanoparticles.

Blocky copolymer based polymeric fibers, synthesized at previous sections in this thesis, resulted in formation of larger nanoparticles with respect to random copolymer of P(AN-co-VPYR). The interaction between metal nanoparticles with polymer side chain was thought to be more effective in random copolymer nature of VPYR. FT-IR and XPS (X-ray Photoelectron Spectroscopy) results showed that the interaction of carbonyl group of VPYR was interacting with Pd and Pt nanoparticles<sup>110, 151-153</sup>. Carbonyl oxygen could donate its lone-pair electron from occupied 2p orbitals to empty s orbitals of metal ions to form  $\delta$ -bond, so the back-donation of electron density from occupied d orbitals of metal ions into the empty  $\pi^*$ -2p antibonding orbitals of carbonyl oxygen might led to the formation of  $\pi$ -bonds. The coordination between carbonyl group and metal ion would make P(AN-co-VPYR) an ideal carrier of metal atoms,

which provided an excellent precursor to synthesize in situ metal nanoparticles. Since metal ions were coordinated with side chains, nanoparticles could be prevented from aggregation in the process of reduction in hydrazine aqueous solution and dispersed very homogeneously in electrospun fiber. Furthermore, such a small size of metal nanoparticle prepared in P(AN-co-VPYR) nanofibers supports the idea that the coordination of metal ion with side chain might play an important role in particle size.

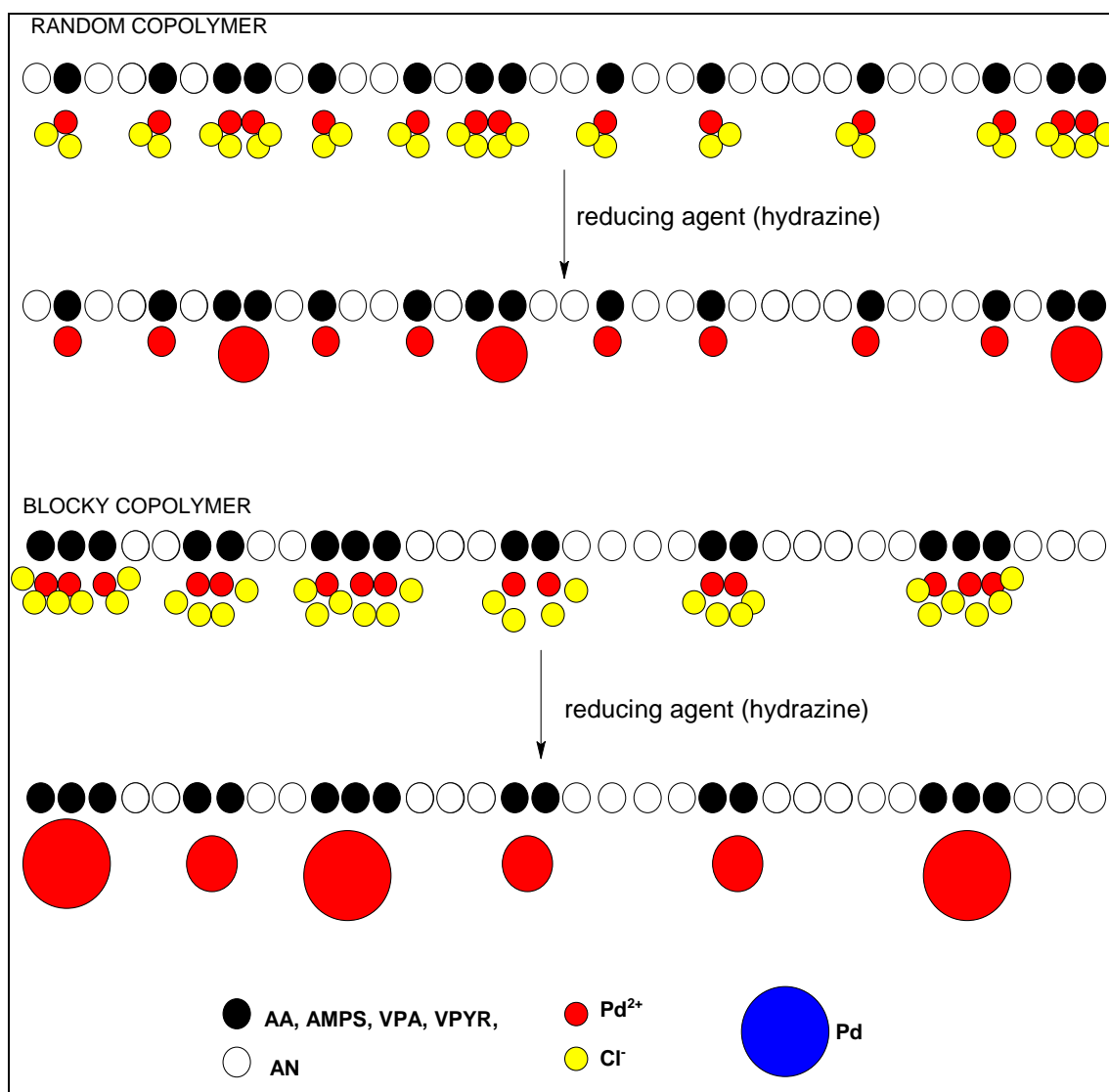


Figure 3.4-16 A schematic of nanoparticle synthesis on random and blocky copolymers

It was also seen that the increase in concentration of VPYR throughout the polymer, resulted in the formation of bigger nanoparticles. Like the case in blocky copolymers, as the interacting species, copolymer side chain and metal, were confined in a concentrated geometry the resulting mechanism led to agglomeration of

nanoparticles (Figure 3.4-16). Similar results were obtained in the literature. Li et al. showed that by increasing degree of sulfonation in SPEEK polymers silver particles tend to coarsen in size<sup>154</sup>.

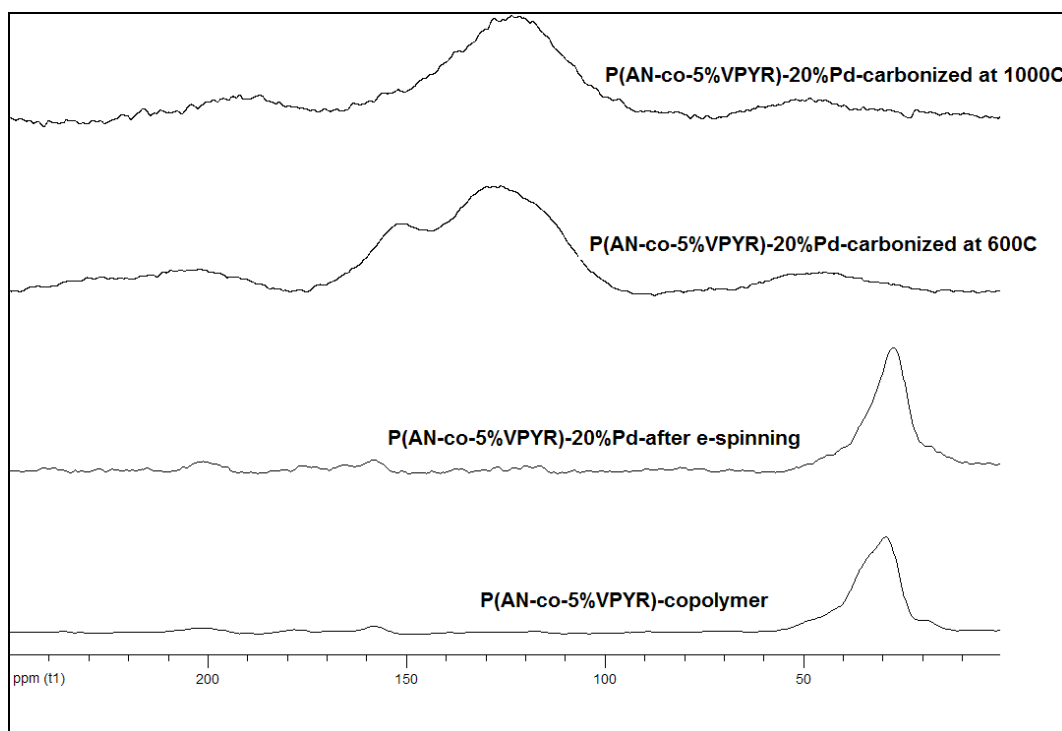


Figure 3.4-17 <sup>13</sup>C-NMR spectrums of P(AN-co-5%VPYR), copolymer, after e-spinning and carbonization at 600°C and 1000°C

For P(AN-co-AA), P(AN-co-VPA) and P(AN-co-AMPS), an increase of particle sizes could not be controlled due to fast loose of polymeric integrity through degradation. But for P(AN-co-VPYR) the delayed degradation temperature with increasing VPYR concentration enabled a perfect stabilization and carbonization mechanism for P(AN-co-VPYR) copolymers. As we examined the <sup>13</sup>C-NMR spectrums, we saw that with increasing temperature polymer structure changed from sp<sup>3</sup> hybridized carbons (27.1 ppm) at low temperatures to sp<sup>2</sup> hybridized carbons atoms at high temperatures (90-175 ppm) (Figure 3.4-17). At 600°C we saw that sp<sup>2</sup> hybridized carbon atoms of -C=C- (128 ppm) formed in lieu to formed pyrrole rings (151 ppm) by the cyclization of cyano groups of acrylonitrile at low temperatures. With the increase

of carbonization temperature from 600°C to 1000°C, polymeric structure shifted to a graphitic one where  $\text{-C=C-}$  bonds dominated (121 ppm).

Noble metals, both in zerovalent and in ionic states, was stated to be prone to form stable  $\pi$ -complexes with multiple  $\text{-C-C-}$  bonds of organic compounds<sup>155</sup>. The stability of the complexes was increased if the ligand contained electron acceptor groups in close to proximity of the  $\text{-C=C-}$  bond. As at low temperatures the ligation of metal atoms with carbonyl atoms were more effective with increasing carbonization temperature, this time the interaction of metal atoms with  $\text{-C=C-}$  bonds became viable for inhibiting particle coalescence. A  $\pi$ -complex might had been formed between an occupied 4d orbital of the metal atom and an unoccupied molecular  $\pi^*$ -orbital of  $\text{-C=C-}$  fragment. The prevention of sintering of nanoparticles could then be attributed to the formation of favored interaction with carbonaceous polymeric structure.

The confinement of nanoparticles within the polymeric matrix, restrained the diffusion of nanoparticles at high temperatures as being a suppressing blanket for the migration of atoms through the surface of fibers since part of the nanoparticles were adsorbed by the surface of polymeric fibers through hydrophobic steric interaction. Physical characteristics of polymeric fiber support namely porosity and specific surface area had been understood to play a key role in stabilizing active components of the catalysts in dispersed state<sup>156</sup>. They reflected topological properties of the fiber surface, namely the nature and quantity of traps (potential wells for atoms and metal particles), which might have behaved as sites of hindrances (potential barriers) for migration of these atoms and particles. An increase in the specific surface area and the micropore volume might have resulted, in a decrease in the size of supported metal particles. The most effective mechanical trapping of a metal particle at a micropore mouth could be achieved at a rather higher temperature as a result of metal flowing into the pore. Through the carbonization, metal nanoparticles could have dug small pits in the carbon support surface, which they might have been then trapped<sup>157, 158</sup>. With increasing temperature the degradation of polymer chain might have led to the weakening of chemical and physical interactions of metal atom with the polymer. The stabilized surface energy of the nanoparticle might be weakened on the fiber which in turn might led to the loss of the effect of delocalization energy and therefore the stabilization through sintering mechanisms could have been favored.

Among the other alternatives in literature, this thesis work showed the best results at advanced temperatures (Table 3.4-8). Particle sizes of 5 nm at 600°C and 13.8 nm at 1000°C were not within to reach by the literature work.

Nanoparticle/Support	Particle Size (nm)	Temperature (°C)	Reference
Pd/PAN	10	300	Kim et al. <sup>110</sup>
Pd/PAN	40	550	Chen et al. <sup>103</sup>
Pd/(Poly(styrene-co-acrylonitrile))	30-40	RT	Yu et al. <sup>104</sup>
Pd-Co/Carbon	8.9-13.8	300-700	Zhang et al. <sup>111</sup>
Pd/PAN	5, 15, 30, 50, 150	400, 600, 800, 1100	Lai et al. <sup>112</sup>
Pd/CNFs	73	1100	Huang et al. <sup>113</sup>
Pt/CNF	50-200	RT	Li et al. <sup>132</sup>
Pt/CNF	10-55	RT	Lin et al. <sup>133</sup>

Table 3.4-8 Literature examples for supported metal nanoparticles

Studies showed that the diffusion coefficients of metal atoms on carbon nanofibers were one order of magnitude lower than those of metal nanoparticles supported by graphite, which also meant that the catalyst nanoparticles in CNF were more stable to aggregation<sup>159, 160</sup>. The use of nanoparticles assisted CNF instead of metal doped carbons will be dominating in the future work.

### 3.4.5 Proof of concept: Catalyst nanoparticles for Fuel Cell Applications

There are mainly two problems related with electrodes in the PEMFC that should be overcome: The price of the electrode materials, and efficiency of the catalysts. Loadings of 0.1 to 0.4 mg Pt/cm<sup>2</sup> are typically found in PEMFC electrodes but it is still around 100\$/kW, so it is not economically superior. In addition, the oxygen reduction reaction at the cathode is primarily the cause of the cell voltage losses, catalyst utilization become crucial part at MEA. This carbon matrix has poor structural, electrical and thermal properties compared to PAN-precured carbon fibers<sup>161</sup>, therefore, more active, better structured and at the same time cheaper catalyst supporter systems are required. Electrospun Pt or Pd nanoparticles including carbon nanofibers have strong potential to solve many of these challenges.

Throughout this thesis, it was shown that the control of the size and distribution of nanoparticles was viable with applied methodology. This section was an example for the use of synthesized nanoparticles on fuel cell applications as catalyst nanoparticles generated on carbonized polymer nanofibers.

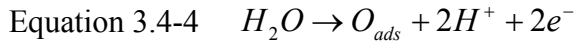
#### 3.4.5.1 Electrochemical Analysis of Pt including fibers

The electroactivity of the nanoparticles was determined both qualitatively and quantitatively by cyclic voltammetry. Cyclic voltammograms of all electrospun fibers that including nano Pt, Pd particles were recorded in 0.5M H<sub>2</sub>SO<sub>4</sub> with various scan rate at room temperature and N<sub>2</sub> atmosphere.

The scanning was started from -0.25 V (SCE) and ended at 1 V (SCE) which is the commonly used range for fuel cell catalysts researches. Typical cyclic voltammogram of Pt catalysts was shown in Figure 3.4-18. The first peak was at -0.2V (SCE), corresponded hydrogen desorption (Equation 3.4-3).



Sweeping to, a higher voltage, oxide formation (of PtO) was encountered. This peak could be represented with the following chemical reaction:



The oxide formation region could be divided into two peaks that are often distinguishable. At around 0.5 V SCE, the following reaction occurred:

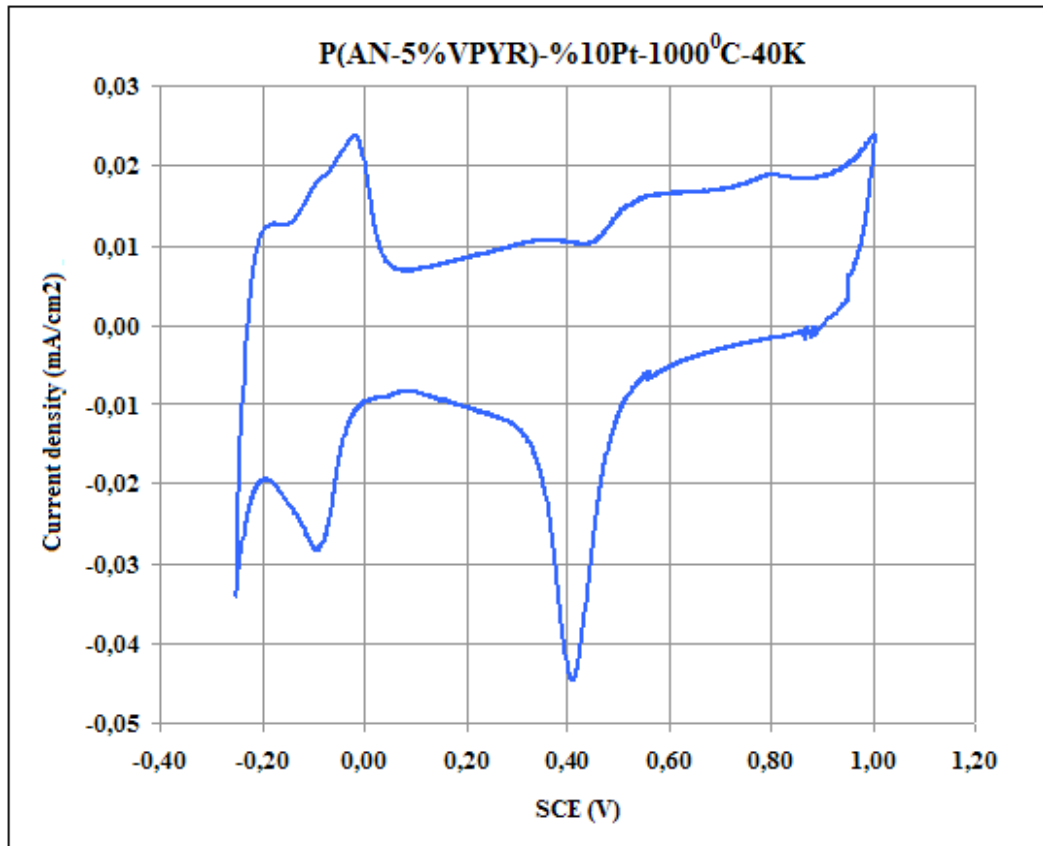
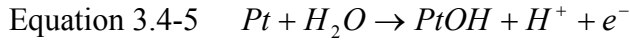
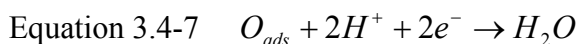


Figure 3.4-18. Cyclic voltammogram of P(AN-co-5%VPYR)-10%Pt-1000°C-40°C

A second small bump was seen around 0.8 V SCE. The second peak in the oxide formation region corresponded to the following reaction:



The voltage sweep then reached its set maximum of 1.0V and reversed direction. At around 0.45 V SCE in Figure 3.4-18, the oxide reduction region was reached. Here, PdO was reduced and the following general reaction occurred:



At oxide 0.45 V SCE where the reduction peak occurred, both reactions in Equation 3.4-5 and Equation 3.4-6 occurred in reverse.

Finally, the cathodic hydrogen region peaks occurred at the same potential as the hydrogen desorption peaks from the reaction in Equation 3.4-3. The hydrogen adsorption reaction was:



The shape of the cyclic voltammogram was the same as the polycrystalline platinum<sup>35, 162</sup>. Hydrogen adsorption-desorption peaks were clearly seen in the voltammogram at the potentials between -0.2-0.05 V (SCE). Qualitatively, the voltammogram showed the catalytic activity. For quantitative measurement, usually the charge under the hydrogen adsorption peak was used to calculate electrochemically active surface area (Equation 3.4-9)<sup>35</sup>. In some case, CO oxidation also is used in order to determine the active area<sup>163</sup>

$$\text{Equation 3.4-9} \quad \text{Electroactive Surface Area} = \text{ESA} = \frac{Q}{(Q_{Pt} \times m_{Pt})}$$

where, Q is the hydrogen adsorption charge obtained from CV,  $Q_{Pt}$ : Charge for monolayer hydrogen adsorption on Pt (210  $\mu\text{C}/\text{cm}^2$ ) [60],  $m_{Pt}$ : Pt amount that used in CV analysis

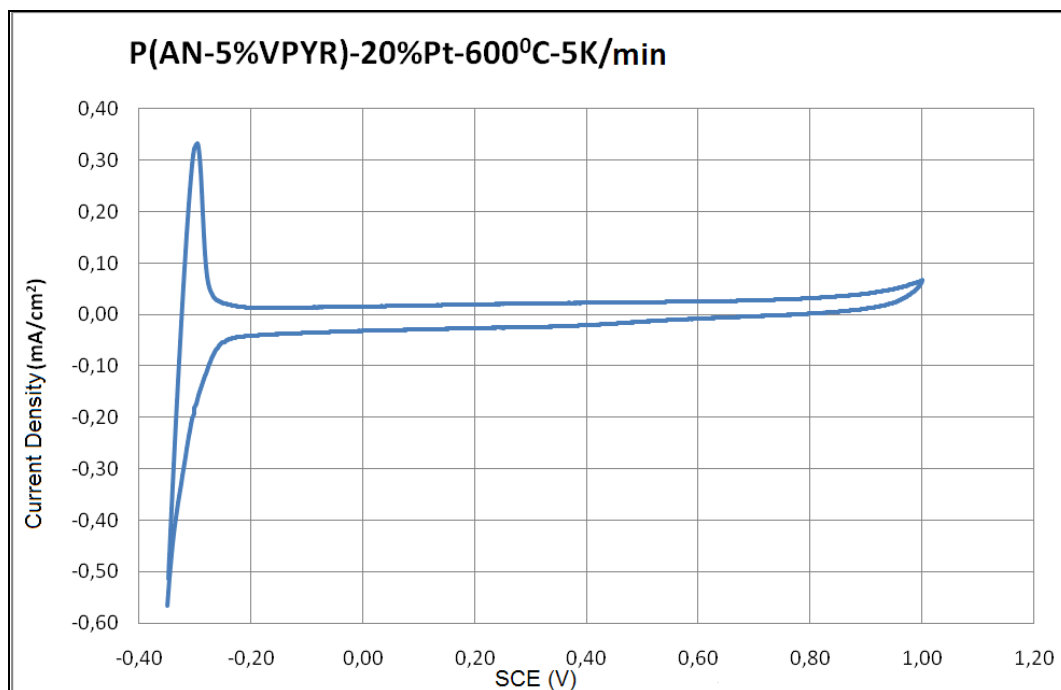


Figure 3.4-19 Cyclic voltammogram of P(AN-co-5%VPYR)-20%Pt-600°C-5°C

The shape of the cyclic voltammogram in Figure 3.4-19 was alike hydrogen oxidation peak was observed at -0.2V. Peak was associated with the weak bond of hydrogen in (111) Pt crystal direction.

Platin Amount	Carbonization cycle	Electroactive Surface Area	Average Particle Size from SEM
%5Pt	1200°C -5°C/min	21.4 m <sup>2</sup> /g	10.1 nm
%10Pt	1000°C -40°C/min	31 m <sup>2</sup> /g	5.2 nm
%20Pt	600°C -5°C/min	34.6 m <sup>2</sup> /g	3.6 nm
%20Pt	1000°C -40°C/min	36 m <sup>2</sup> /g	9.4 nm

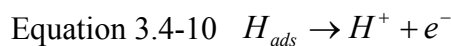
Table 3.4-9 Summary of electrochemical results for Pt including fibers

Highest electroactivity value 34.6 m<sup>2</sup>/g was achieved by 20% Pt including P(AN-5%VPYR) that was carbonized at 600° C-40°C/min. The electroactive surface area of commercial Pt catalyst used in a PEMFC is around 70 m<sup>2</sup>/g<sup>164</sup>. Commercial Pt particle

sizes did not exceed 4 nm<sup>165</sup>. As the size of the platinum particles increased relative to the optimum particle size, the fraction of platinum atoms on the particle surface decreased and thus the number of sites available for surface reactions also decreased. This resulted in a reduction in specific catalytic activity (activity per unit mass of catalyst). Due to agglomeration of Pt nanoparticles, the achieved electroactive surface area was respectively lower. Furthermore, nanoparticles embedded within the fibers could not show electroactivity. It was possible platinum particles deposit into pores in the carbon host and these pores were not wetted by electrolyte during analysis. This would render the platinum in the pores inactive. However, the electroactive surface area calculation was not only tool to qualify the catalysts. In order to evaluate the real performance of the nanocatalysts, real condition fuel cell testing was crucial.

#### 3.4.5.2 Electrochemical Analysis of Pd including fibers

The peaks at Figure 3.4-20 corresponded to the electrochemical activity. For a positive sweep voltage starting from -0.25V (SCE) moving higher potential, the first peak after -0.2V(SCE) was the hydrogen desorption peak (Equation 3.4-10)



If the surface of the electrode was very smooth multiple peaks could be distinguished for desorption of monolayer. While sweeping higher voltage oxide formation of PdO was encountered at around 0.39 V(SCE) (Equation 3.4-11).



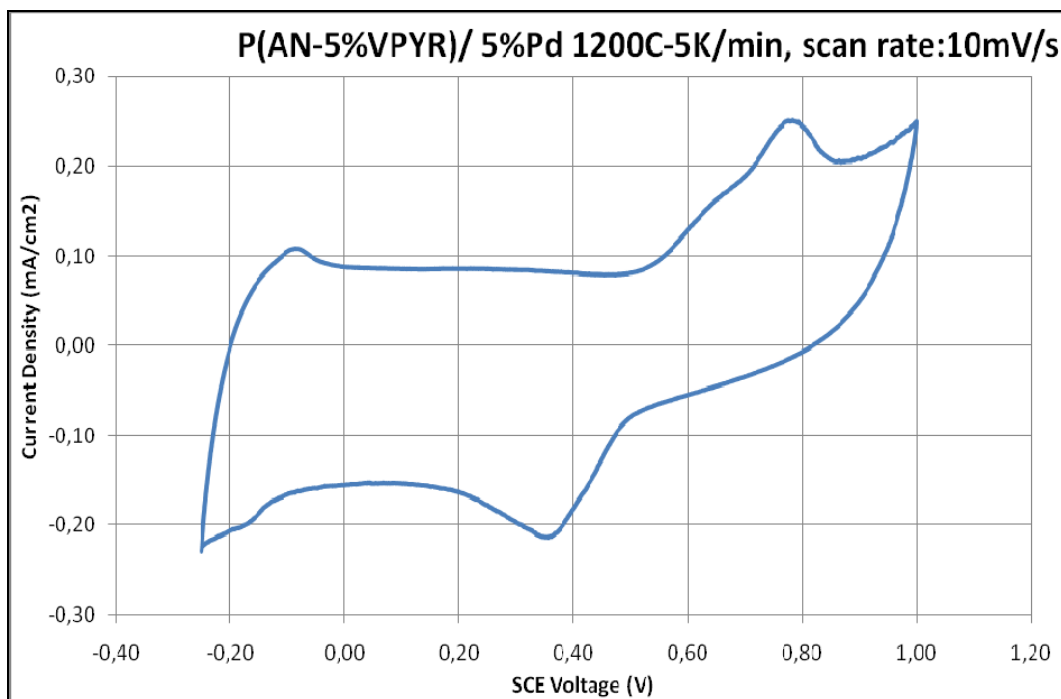
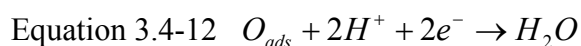
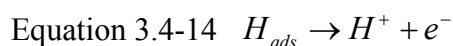


Figure 3.4-20. Cyclic voltammogram of P(AN-co-5%VPYR)-5%Pd-1200°C-5°C

At around 0.75V (SCE) oxide reduction region was reached after reverse sweeping was started (Equation 3.4-12). Here PdO was reduced and the second reaction was reversed (Equation 3.4-13).



Finally cathodic hydrogen - adsorption peaks occurred at -0.1V (SCE) (Equation 3.4-14).



Different heating rates and heating temperature gave different voltammograms. If the Pd concentration increased the current density dramatically became greater. It was obvious that, as the Pd content per cm<sup>2</sup> area was higher on changing from 5% to 20% with respect to polymer weight, more electro active sites were available; as a result,

more current can be obtained (Figure 3.4-21.) Also, the carbonization rate of the carbon fiber based Pd nanoparticles was directly related with the obtained current. Rapid carbonization prevented agglomeration of Pd particles as low currents for the samples heated to 600°C at a rate between 0.1°C /min to 5°C /min were seen. Figure 3.4-22 confirmed this fact.

Electroactive surface area can be calculated via either hydrogen adsorption or oxide reduction<sup>166</sup> peak at the cyclic voltammogram for Pd nanocatalysts. In this study, the oxide reduction peaks were investigated. Because, for Pd catalysts hydrogen molecules were not only adsorbed but also absorbed. Electrochemical activity resulted for Pd catalysts were shown in Table 3.4-10.

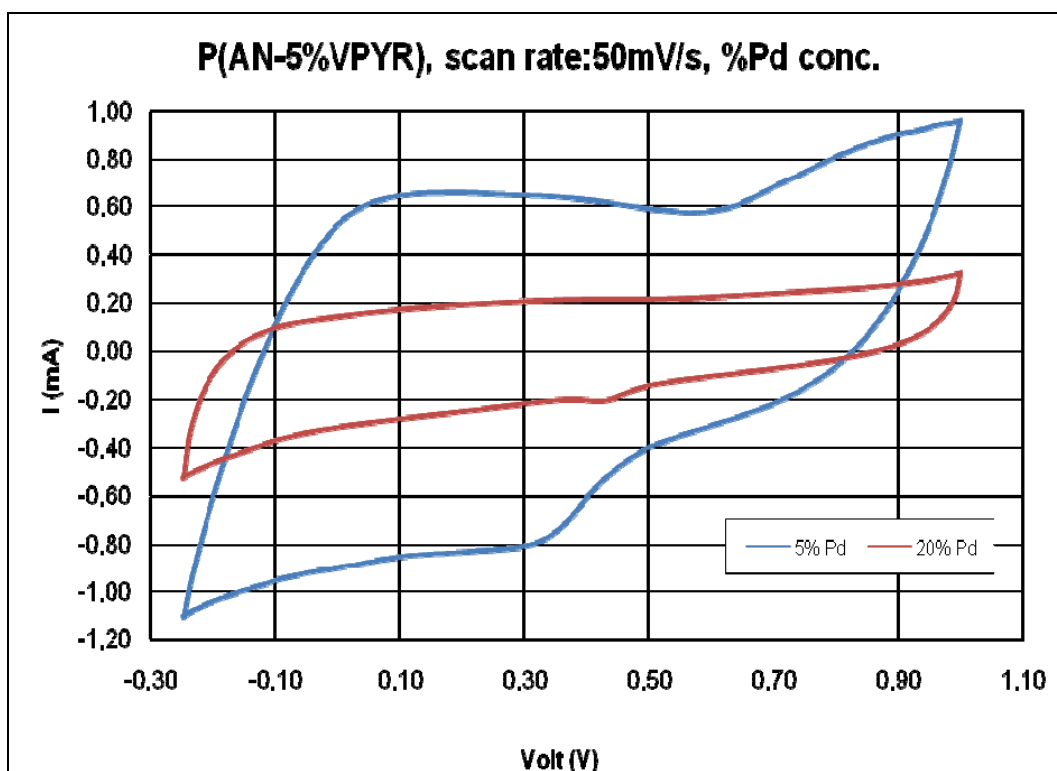


Figure 3.4-21 Cyclic voltammogram of P(AN-co-5%VPYR), different Pd% concentration

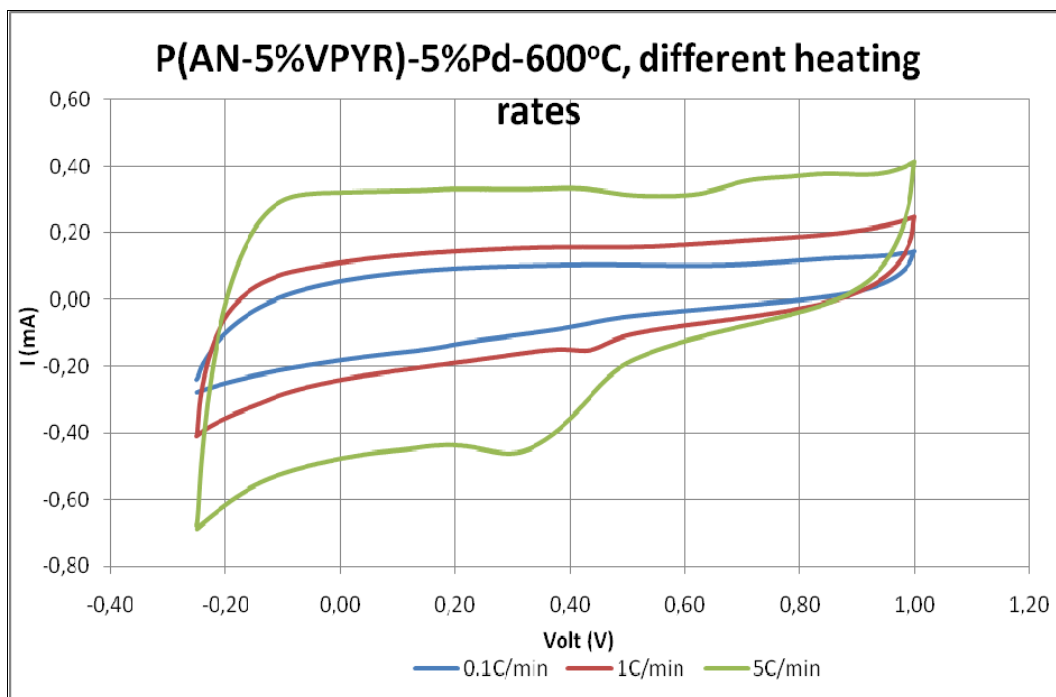


Figure 3.4-22 Cyclic voltammogram of P(AN-co-5%VPYR)-5%Pd, different heating rates

Palladium Amount	Charge ( $\mu\text{C}/\text{cm}^2$ )	Electroactive Surface Area( $\text{m}^2/\text{g}$ )	Average particle size from SEM (nm)
%5Pd	1287 $\mu\text{C}/\text{cm}^2$	22.37 $\text{m}^2/\text{g}$	<4; 28; 6 $\pm$ 4.9
%10 Pd	5507 $\mu\text{C}/\text{cm}^2$	12 $\text{m}^2/\text{g}$	6.2 $\pm$ 0.9; 14.9 $\pm$ 1.8
%20 Pd	1260 $\mu\text{C}/\text{cm}^2$	5.48 $\text{m}^2/\text{g}$	6.3 $\pm$ 1.0; 19.2 $\pm$ 3.2

Table 3.4-10 Summary of electrochemical results for Pd including fibers

Lower activity values were obtained from Pd including carbon nanofibers comparing Pt including carbon fibers. Indeed, Pt nanocatalysts are more active than Pd nanocatalysts. Pt catalysts or Pt-M binary catalysts were used currently in a PEMFC <sup>167</sup>.

## **CHAPTER 4**

### **4 CONCLUSION and FUTURE WORK**

The precise control of particle size and the distribution of nanoparticles was the heart of this thesis. The aim of this work was to suggest an alternative way for synthesizing nanoparticles through the electrospinning process. By maneuvering the macromolecular architecture of chosen polymers, we mediated to the controlled synthesis of nanoparticles.

Electrospinning parameters were discussed in detail throughout this thesis. The change of polymer concentration and solution conductivity affected resulting fiber diameters. As polymer concentration increased so did the fiber diameters and addition of extra metal salts into polymer solutions favored in the formation of more uniform and thinner fibers.

By appropriately choosing reduction solvent and heat treating cycles, enhanced control of nanoparticle sizes at different reduction mediums and temperatures was achievable on different processing conditions.

From the beginning of this work it was shown that choosing an appropriate polymer template would determine the size and distribution of nanoparticles. Synthesized blocky-copolymers of acrylonitrile with acrylic acid, vinyl phosphonic acid 2-acrylamido-2-methylpropane sulfonic acid yielded agglomerated nanoparticles. The

change of polymer architecture to a random structure poly(acrylonitrile-co-n-vinylpyrrolidinone), the size of nanoparticles could be reduced to several nanometers. Effective control of macromolecular design by altering the copolymer structure enabled the size tuning for nanoparticle crystals.

Another success of this thesis lies in the confinement of nanoparticles in sub 10nm's with uniform distributions throughout the fiber structures even at elevated temperatures. Rather than other literature findings, nanoparticles could be generated even at order of 2-5 nm at 600°C, and 10-17 nm at 1000°C, which were the smallest among the similar researches.

The catalytic activities of metal nanoparticles on carbon nanofibers showed an electroactive active surface area of 34.6 m<sup>2</sup>/g for Pt and 22.4 m<sup>2</sup>/g for Pd. These results confirmed the viability of use of metalized nanoparticles on carbon nanofibers as catalysts for fuel cell applications.

These results proved the concept of this research that by selectively choosing the processing conditions and the production techniques, generation of nanoparticles in uniform and smaller dimensions was possible.

## **CHAPTER 5**

### **5 FUTURE PLANS and SUGGESTED ACTIONS**

The results of this work suggest that by appropriately chosen polymer morphology and architecture, nanoparticles can be generated at different sizes. For a future work different polymerization techniques e.g. living anionic polymerization or controlled radical polymerization, can be used for synthesizing alternative structures. By choosing different copolymers the interaction between metal nanoparticles with polymer side chain can be investigated more in detail. A XPS study for the investigation of the interaction between polymer backbone and metal nanoparticle will be effective.

For the reduction of nanoparticles different methods can also be applied. The change in the reduction mechanism will favorably affect the resulting particle size and morphology.

For characterization of nanoparticles, XRD was used for determining crystalline sizes after heat treatment cycles and the comments were given on the obtained spectrum results. If an in-situ observation can be made during the heating step, the growth mechanism of the nanoparticles can be more distinctively evaluated and the kinetics and governing factors behind this mechanism can be revealed.

Catalytic activities of synthesized nanoparticles were investigated for PEM fuel cell reactions. Methanol or formic acid based electrochemical investigations should also be made, including real fuel cell operations.

## CHAPTER 6

### 6 REFERENCES

1. Che, G. L.; Lakshmi, B. B.; Fisher, E. R.; Martin, C. R., Carbon nanotubule membranes for electrochemical energy storage and production. *Nature* **1998**, *393* (6683), 346-349.
2. Joo, S. H.; Choi, S. J.; Oh, I.; Kwak, J.; Liu, Z.; Terasaki, O.; Ryoo, R., Ordered nanoporous arrays of carbon supporting high dispersions of platinum nanoparticles. *Nature* **2001**, *412* (6843), 169-172.
3. Planeix, J. M.; Coustel, N.; Coq, B.; Brotons, V.; Kumbhar, P. S.; Dutartre, R.; Geneste, P.; Bernier, P.; Ajayan, P. M., Application of carbon nanotubes as supports in heterogenous catalysis. *J Am Chem Soc* **1994**, *116* (17), 7935-7936.
4. Li, W. Z.; Liang, C. H.; Qiu, J. S.; Zhou, W. J.; Han, H. M.; Wei, Z. B.; Sun, G. Q.; Xin, Q., Carbon nanotubes as support for cathode catalyst of a direct methanol fuel cell. *Carbon* **2002**, *40* (5), 791-794.
5. Zamudio, A.; Elias, A. L.; Rodriguez-Manzo, J. A.; Lopez-Urias, F.; Rodriguez-Gattorno, G.; Lupo, F.; Ruhle, M.; Smith, D. J.; Terrones, H.; Diaz, D.; Terrones, M., Efficient anchoring of silver nanoparticles on N-doped carbon nanotubes. *Small* **2006**, *2* (3), 346-350.
6. Guo, D. J.; Li, H. L., Electrochemical synthesis of Pd nanoparticles on functional MWNT surfaces. *Electrochem Commun* **2004**, *6* (10), 999-1003.
7. Tessonier, J. P.; Pesant, L.; Ehret, G.; Ledoux, M. J.; Pham-Huu, C., Pd nanoparticles introduced inside multi-walled carbon nanotubes for selective hydrogenation of cinnamaldehyde into hydrocinnamaldehyde. *Appl Catal a-Gen* **2005**, *288* (1-2), 203-210.

8. Toebe, M. L.; Prinsloo, F. F.; Bitter, J. H.; van Dillen, A. J.; de Jong, K. P., Influence of oxygen-containing surface groups on the activity and selectivity of carbon nanofiber-supported ruthenium catalysts in the hydrogenation of cinnamaldehyde. *J Catal* **2003**, *214* (1), 78-87.
9. Bessel, C. A.; Laubernds, K.; Rodriguez, N. M.; Baker, R. T. K., Graphite nanofibers as an electrode for fuel cell applications. *Journal of Physical Chemistry B* **2001**, *105* (6), 1115-1118.
10. Kong, J.; Franklin, N. R.; Zhou, C. W.; Chapline, M. G.; Peng, S.; Cho, K. J.; Dai, H. J., Nanotube molecular wires as chemical sensors. *Science* **2000**, *287* (5453), 622-625.
11. Ozaki, J.; Ohizumi, W.; Oya, A.; Illan-Gomez, M. J.; Roman-Martinez, M. C.; Linares-Solano, A., Comparison of hydrogen adsorption abilities of platinum-loaded carbon fibers prepared using two different methods. *Carbon* **2000**, *38* (5), 778-780.
12. Ozaki, J.; Ohizumi, W.; Endo, N.; Oya, A.; Yoshida, S.; Iizuka, T.; Roman-Martinez, M. C.; Linares-Solano, A., Preparation of platinum loaded carbon fiber by using a polymer blend. *Carbon* **1997**, *35* (10-11), 1676-1677.
13. Toebe, M. L.; van Dillen, J. A.; de Jong, Y. P., Synthesis of supported palladium catalysts. *J Mol Catal a-Chem* **2001**, *173* (1-2), 75-98.
14. Wildgoose, G. G.; Banks, C. E.; Compton, R. G., Metal nanoparticles and related materials supported on carbon nanotubes: Methods and applications. *Small* **2006**, *2* (2), 182-193.
15. Feynmann, R. P. There's Plenty of Room at the Bottom. <http://www.zyvex.com/nanotech/feynman.html>.
16. Taniguchi, N. In *On the Basic Concept of 'Nano-Technology*, Proc. Intl. Conf. Prod., London, British Society of Precision Engineering: London, 1974.
17. Drexler, K. E., *Engines of Creation: The Coming Era of Nanotechnology*. Anchor Books: New York, 1986.
18. Jefferson, D. A., The surface activity of ultrafine particles. *Philos. Trans. R. Soc. Lond. Ser. A-Math. Phys. Eng. Sci.* **2000**, *358* (1775), 2683-2692.
19. Haruta, A., When gold is not noble: Catalysis by nanoparticles. *Chemical Record* **2003**, *3* (2), 75-87.
20. Wang, J. S.; Matyjaszewski, K., Controlled Living Radical Polymerization - Atom-Transfer Radical Polymerization In The Presence Of Transition-Metal Complexes. *J Am Chem Soc* **1995**, *117* (20), 5614-5615.
21. Matyjaszewski, K. In *Macromolecular engineering by controlled/living ionic and radical polymerizations*, Warsaw, Poland, Jul 09-14; Warsaw, Poland, 2000; pp 51-67.

22. Hawker, C. J.; Bosman, A. W.; Harth, E., New polymer synthesis by nitroxide mediated living radical polymerizations. *Chemical Reviews* **2001**, *101* (12), 3661-3688.
23. Moad, G.; Mayadunne, R. T. A.; Rizzardo, E.; Skidmore, M.; Thang, S. H. In *Synthesis of novel architectures by radical polymerization with reversible addition fragmentation chain transfer (RAFT polymerization)*, Oaxaca, Mexico, Dec 03-07; Oaxaca, Mexico, 2001; pp 1-12.
24. Schmid, G., *Nanoparticles*. Wiley-Interscience: New York, 2004.
25. Nalwa, H., *Handbook of nanostructured materials and nanotechnology*. Academic Press: New York, 2000.
26. Liu, T. B.; Burger, C.; Chu, B., Nanofabrication in polymer matrices. *Progress in Polymer Science* **2003**, *28* (1), 5-26.
27. Cao, G., *Nanostructures and nanomaterials: synthesis, properties and applications*. Imperial College Press: London, 2004.
28. Zhang, Q.; Archer, L. A., Poly(ethylene oxide)/silica nanocomposites: Structure and rheology. *Langmuir* **2002**, *18* (26), 10435-10442.
29. Schmidt, G.; Malwitz, M. M., Properties of polymer-nanoparticle composites. *Current Opinion in Colloid & Interface Science* **2003**, *8* (1), 103-108.
30. Li, Y.; El-Sayed, M. A., The effect of stabilizers on the catalytic activity and stability of Pd colloidal nanoparticles in the Suzuki reactions in aqueous solution. *J Phys Chem B* **2001**, *105* (37), 8938-8943.
31. Mayer, A. B. R.; Mark, J. E., Transition metal nanoparticles protected by amphiphilic block copolymers as tailored catalyst systems. *Colloid and Polymer Science* **1997**, *275* (4), 333-340.
32. Sun, Y. G.; Mayers, B.; Herricks, T.; Xia, Y. N., Polyol synthesis of uniform silver nanowires: A plausible growth mechanism and the supporting evidence. *Nano Letters* **2003**, *3* (7), 955-960.
33. Teranishi, T.; Hosoe, M.; Tanaka, T.; Miyake, M., Size control of monodispersed Pt nanoparticles and their 2D organization by electrophoretic deposition. *J Phys Chem B* **1999**, *103* (19), 3818-3827.
34. Teranishi, T.; Kurita, R.; Miyake, M., Shape control of Pt nanoparticles. *Journal of Inorganic and Organometallic Polymers* **2000**, *10* (3), 145-156.
35. Chen, M.; Xing, Y. C., Polymer-mediated synthesis of highly dispersed Pt nanoparticles on carbon black. *Langmuir* **2005**, *21* (20), 9334-9338.
36. Wang, H. S.; Qiao, X. L.; Chen, J. G.; Wang, X. J.; Ding, S. Y., Mechanisms of PVP in the preparation of silver nanoparticles. *Materials Chemistry and Physics* **2005**, *94* (2-3), 449-453.

37. Narayanan, R.; El-Sayed, M. A., Effect of catalysis on the stability of metallic nanoparticles: Suzuki reaction catalyzed by PVP-palladium nanoparticles. *J Am Chem Soc* **2003**, *125* (27), 8340-8347.
38. Formhals, A. Method and apparatus for spinning, US2160962 (A), 1939.
39. Formhals, A. Artificial thread and method of producing same, US2187306 (A), 1940.
40. Formhals, A. Production of artificial fibers from fiber forming liquids , US2323025 (A), 1943.
41. Formhals, A. Method and apparatus for spinning, US2349950 (A), 1944.
42. Taylor, G. I. In *Electrically driven jets*, Proc. Roy. Soc, 1969; pp 453-475.
43. Baumgarten, P. K., Electrostatic spinning of acrylic microfibers *Journal of Colloid and Interface Science* **1971**, *36* (1).
44. Larrondo, L.; Manley, R. S. J., Electrostatic Fiber Spinning From Polymer Melts .3. Electrostatic Deformation Of A Pendant Drop Of Polymer Melt. *Journal of Polymer Science Part B-Polymer Physics* **1981**, *19* (6), 933-940.
45. Larrondo, L.; Manley, R. S. J., Electrostatic Fiber Spinning From Polymer Melts .2. Examination Of The Flow Field In An Electrically Driven Jet. *Journal of Polymer Science Part B-Polymer Physics* **1981**, *19* (6), 921-932.
46. Larrondo, L.; Manley, R. S. J., Electrostatic Fiber Spinning From Polymer Melts .1. Experimental-Observations On Fiber Formation And Properties. *Journal of Polymer Science Part B-Polymer Physics* **1981**, *19* (6), 909-920.
47. Zhang, R. Y.; Ma, P. X., Porous poly(L-lactic acid)/apatite composites created by biomimetic process. *Journal of Biomedical Materials Research* **1999**, *45* (4), 285-293.
48. Ma, P. X.; Zhang, R. Y., Synthetic nano-scale fibrous extracellular matrix. *Journal of Biomedical Materials Research* **1999**, *46* (1), 60-72.
49. Huang, Z. M.; Zhang, Y. Z.; Kotaki, M.; Ramakrishna, S., A review on polymer nanofibers by electrospinning and their applications in nanocomposites. *Composites Science and Technology* **2003**, *63* (15), 2223-2253.
50. Frenot, A.; Chronakis, I. S., Polymer nanofibers assembled by electrospinning. *Current Opinion in Colloid & Interface Science* **2003**, *8* (1), 64-75.
51. Li, D.; Ouyang, G.; McCann, J. T.; Xia, Y. N., Collecting electrospun nanofibers with patterned electrodes. *Nano Letters* **2005**, *5* (5), 913-916.
52. Fridrikh, S. V.; Yu, J. H.; Brenner, M. P.; Rutledge, G. C., Controlling the fiber diameter during electrospinning. *Physical Review Letters* **2003**, *90* (14).

53. Fong, H.; Chun, I.; Reneker, D. H. In *Beaded nanofibers formed during electrospinning*, 1999; pp 4585-4592.
54. Gupta, P.; Wilkes, G. L., Some investigations on the fiber formation by utilizing a side-by-side bicomponent electrospinning approach. *Polymer* **2003**, *44* (20), 6353-6359.
55. Deitzel, J. M.; Kleinmeyer, J.; Harris, D.; Tan, N. C. B., The effect of processing variables on the morphology of electrospun nanofibers and textiles. *Polymer* **2001**, *42* (1), 261-272.
56. Demir, M. M.; Yilgor, I.; Yilgor, E.; Erman, B., Electrospinning of polyurethane fibers. *Polymer* **2002**, *43* (11), 3303-3309.
57. Hsu, C. M.; Shivkumar, S., Nano-sized beads and porous fiber constructs of poly(epsilon-caprolactone) produced by electrospinning. *Journal of Materials Science* **2004**, *39* (9), 3003-3013.
58. Ramakrishna, S.; Fujihara, K.; Teo, W. E.; Yong, T.; Ma, Z. W.; Ramaseshan, R., Electrospun nanofibers: solving global issues. *Materials Today* **2006**, *9* (3), 40-50.
59. Zong, X. H.; Kim, K.; Fang, D. F.; Ran, S. F.; Hsiao, B. S.; Chu, B., Structure and process relationship of electrospun bioabsorbable nanofiber membranes. *Polymer* **2002**, *43* (16), 4403-4412.
60. Seo, J. M.; Arumugam, G. K.; Khan, S.; Heiden, P. A., Comparison of the Effects of an Ionic Liquid and Triethylbenzylammonium Chloride on the Properties of Electrospun Fibers, 1-Poly(lactic acid). *Macromolecular Materials and Engineering* **2009**, *294* (1), 35-44.
61. Kim, Y. J., Effect of Ionic Salts on the Structure of Electrospun Gelatin Nanofibers. *Polymer-Korea* **2008**, *32* (5), 409-414.
62. Fallahi, D.; Rafizadeh, M.; Mohammadi, N.; Vahidi, B., Effect of LiCl and non-ionic surfactant on morphology of polystyrene electrospun nanofibers. *E-Polymers* **2008**.
63. Marras, S. I.; Kladi, K. P.; Tsvintzelis, L.; Zuburtikudis, I.; Panayiotou, C., Biodegradable polymer nanocomposites: The role of nanoclays on the thermomechanical characteristics and the electrospun fibrous structure. *Acta Biomaterialia* **2008**, *4* (3), 756-765.
64. Megelski, S.; Stephens, J. S.; Chase, D. B.; Rabolt, J. F., Micro- and nanostructured surface morphology on electrospun polymer fibers. *Macromolecules* **2002**, *35* (22), 8456-8466.
65. Lee, J. S.; Choi, K. H.; Do Ghim, H.; Kim, S. S.; Chun, D. H.; Kim, H. Y.; Lyoo, W. S., Role of molecular weight of atactic poly(vinyl alcohol) (PVA) in the structure and properties of PVA nanofabric prepared by electrospinning. *Journal of Applied Polymer Science* **2004**, *93* (4), 1638-1646.

66. Zhao, S. L.; Wu, X. H.; Wang, L. G.; Huang, Y., Electrospinning of ethylcyanoethyl cellulose/tetrahydrofuran solutions. *Journal of Applied Polymer Science* **2004**, *91* (1), 242-246.
67. De Vrieze, S.; Van Camp, T.; Nelvig, A.; Hagstrom, B.; Westbroek, P.; De Clerck, K., The effect of temperature and humidity on electrospinning. *Journal of Materials Science* **2009**, *44* (5), 1357-1362.
68. Tan, S.; Huang, X.; Wu, B., Some fascinating phenomena in electrospinning processes and applications of electrospun nanofibers. *Polymer International* **2007**, *56* (11), 1330-1339.
69. Qin, X. H.; Wang, S. Y., Electrospun nanofibers from crosslinked poly(vinyl alcohol) and its filtration efficiency. *Journal of Applied Polymer Science* **2008**, *109* (2), 951-956.
70. Lee, S.; Obendorf, S. K., Developing protective textile materials as barriers to liquid penetration using melt-electrospinning. *Journal of Applied Polymer Science* **2006**, *102* (4), 3430-3437.
71. Kim, C.; Park, S. H.; Lee, W. J.; Yang, K. S. In *Characteristics of supercapacitor electrodes of PBI-based carbon nanofiber web prepared by electrospinning*, 2004; pp 877-881.
72. Kim, C.; Yang, K. S.; Lee, W. J., The use of carbon nanofiber electrodes prepared by electrospinning for electrochemical supercapacitors. *Electrochemical and Solid State Letters* **2004**, *7* (11), A397-A399.
73. Kim, C.; Yang, K. S., Electrochemical properties of carbon nanofiber web as an electrode for supercapacitor prepared by electrospinning. *Applied Physics Letters* **2003**, *83* (6), 1216-1218.
74. Liu, F. J.; Huang, L. M.; Wen, T. C.; Gopalan, A., Large-area network of polyaniline nanowires supported platinum nanocatalysts for methanol oxidation. *Synthetic Metals* **2007**, *157* (16-17), 651-658.
75. Kheirmand, M.; Gharibi, H.; Mirzaie, R. A.; Faraji, M.; Zhiani, M., Study of the synergism effect of a binary carbon system in the nanostructure of the gas diffusion electrode (GDE) of a proton exchange membrane fuel cell. *Journal of Power Sources* **2007**, *169* (2), 327-333.
76. Kim, H. W.; Song, J. H.; Kim, H. E., Nanoriber generation of gelatin-hydroxyapatite biomimetics for guided tissue regeneration. *Advanced Functional Materials* **2005**, *15* (12), 1988-1994.
77. Khil, M. S.; Bhattarai, S. R.; Kim, H. Y.; Kim, S. Z.; Lee, K. H., Novel fabricated matrix via electrospinning for tissue engineering. *Journal of Biomedical Materials Research Part B-Applied Biomaterials* **2005**, *72B* (1), 117-124.

78. Katti, D. S.; Robinson, K. W.; Ko, F. K.; Laurencin, C. T., Bioresorbable nanofiber-based systems for wound healing and drug delivery: Optimization of fabrication parameters. *Journal of Biomedical Materials Research Part B-Applied Biomaterials* **2004**, *70B* (2), 286-296.
79. Doshi, J.; Reneker, D. H. In *Electrospinning Process And Applications Of Electrospun Fibers*, Toronto, Canada, Oct 03-08; Elsevier Science Bv: Toronto, Canada, 1993; pp 151-160.
80. Drew, C.; Liu, X.; Ziegler, D.; Wang, X. Y.; Bruno, F. F.; Whitten, J.; Samuelson, L. A.; Kumar, J., Metal oxide-coated polymer nanofibers. *Nano Letters* **2003**, *3* (2), 143-147.
81. Yang, Q. B.; Li, D. M.; Hong, Y. L.; Li, Z. Y.; Wang, C.; Qiu, S. L.; Wei, Y., Preparation and characterization of a pan nanofibre containing Ag nanoparticles via electrospinning. *Synthetic Metals* **2003**, *137* (1-3), 973-974.
82. Hou, H. Q.; Reneker, D. H., Carbon nanotubes on carbon nanofibers: A novel structure based on electrospun polymer nanofibers. *Advanced Materials* **2004**, *16* (1), 69-+.
83. Melaiye, A.; Sun, Z. H.; Hindi, K.; Milsted, A.; Ely, D.; Reneker, D. H.; Tessier, C. A.; Youngs, W. J., Silver(I)-imidazole cyclophane gem-diol complexes encapsulated by electrospun tectophilic nanofibers: Formation of nanosilver particles and antimicrobial activity. *J Am Chem Soc* **2005**, *127* (7), 2285-2291.
84. Demir, M. M.; Gulgun, M. A.; Menciloglu, Y. Z.; Erman, B.; Abramchuk, S. S.; Makhaeva, E. E.; Khokhlov, A. R.; Matveeva, V. G.; Sulman, M. G., Palladium nanoparticles by electrospinning from poly(acrylonitrile-co-acrylic acid)-PdCl<sub>2</sub> solutions. Relations between preparation conditions, particle size, and catalytic activity. *Macromolecules* **2004**, *37* (5), 1787-1792
85. Li, Z. Y.; Huang, H. M.; Shang, T. C.; Yang, F.; Zheng, W.; Wang, C.; Manohar, S. K., Facile synthesis of single-crystal and controllable sized silver nanoparticles on the surfaces of polyacrylonitrile nanofibres. *Nanotechnology* **2006**, *17* (3), 917-920.
86. Zhang, Q.; Wu, D. H.; Qi, S. L.; Wu, Z. P.; Yang, X. P.; Jin, R. G., Preparation of ultra-fine polyimide fibers containing silver nanoparticles via in situ technique. *Materials Letters* **2007**, *61* (19-20), 4027-4030.
87. Roso, M.; Sundarajan, S.; Pliszka, D.; Ramakrishna, S.; Modesti, M., Multifunctional membranes based on spinning technologies: the synergy of nanofibers and nanoparticles. *Nanotechnology* **2008**, *19* (28).
88. Luong, N. D.; Lee, Y.; Nam, J. D., Highly-loaded silver nanoparticles in ultrafine cellulose acetate nanofibrillar aerogel. *European Polymer Journal* **2008**, *44* (10), 3116-3121.
89. Son, W. K.; Youk, J. H.; Park, W. H., Antimicrobial cellulose acetate nanofibers containing silver nanoparticles. *Carbohydrate Polymers* **2006**, *65* (4), 430-434.

90. Xu, X. L.; Zhou, M. H., Antimicrobial gelatin nanofibers containing silver nanoparticles. *Fibers and Polymers* **2008**, *9* (6), 685-690.
91. Lee, H. K.; Jeong, E. H.; Baek, C. K.; Youk, J. H., One-step preparation of ultrafine poly(acrylonitrile) fibers containing silver nanoparticles. *Materials Letters* **2005**, *59* (23), 2977-2980.
92. Wang, Y. Z.; Li, Y. X.; Sun, G.; Zhang, G. L.; Liu, H.; Du, J. S.; Yang, S. A.; Bai, J.; Yang, Q. B., Fabrication of Au/PVP by electrospinning nanofiber composites by electrospinning. *Journal of Applied Polymer Science* **2007**, *105* (6), 3618-3622.
93. Xu, X.; Yang, Q.; Wang, Y.; Yu, H.; Chen, X.; Jing, X., Biodegradable electrospun poly(l-lactide) fibers containing antibacterial silver nanoparticles. *European Polymer Journal* **2006**, *42* (9), 2081-2087.
94. Hong, K. H., Preparation and properties of electrospun poly (vinyl alcohol)/silver fiber web as wound dressings. *Polymer Engineering and Science* **2007**, *47* (1), 43-49.
95. Min, K. D.; Youk, A. H.; Kwark, Y. J.; Park, W. H., Preparation of inorganic silica nanofibers containing silver nanoparticles. *Fibers and Polymers* **2007**, *8* (6), 591-600.
96. Kim, G. M.; Wutzler, A.; Radusch, H. J.; Michler, G. H.; Simon, P.; Sperling, R. A.; Parak, W. J., One-dimensional arrangement of gold nanoparticles by electrospinning. *Chemistry of Materials* **2005**, *17* (20), 4949-4957.
97. Kalra, V.; Lee, J.; Lee, J. H.; Lee, S. G.; Marquez, M.; Wiesner, U.; Joo, Y. L., Controlling Nanoparticle Location via Confined Assembly in Electrospun Block Copolymer Nanofibers. *Small* **2008**, *4* (11), 2067-2073.
98. Sundarrajan, S.; Ramakrishna, S., Fabrication of nanocomposite membranes from nanofibers and nanoparticles for protection against chemical warfare stimulants. *Journal of Materials Science* **2007**, *42* (20), 8400-8407.
99. Oh, G. Y.; Ju, Y. W.; Jung, H. R.; Lee, W. J., Preparation of the novel manganese-embedded PAN-based activated carbon nanofibers by electrospinning and their toluene adsorption. *Journal of Analytical and Applied Pyrolysis* **2008**, *81* (2), 211-217.
100. Ji, L. W.; Zhang, X. W., Manganese oxide nanoparticle-loaded porous carbon nanofibers as anode materials for high-performance lithium-ion batteries. *Electrochem Commun* **2009**, *11* (4), 795-798.
101. Lu, X. F.; Zhao, Y. Y.; Wang, C., Fabrication of PbS nanoparticles in polymer-fiber matrices by electrospinning. *Advanced Materials* **2005**, *17* (20), 2485-+.
102. Peirano, F.; Vincent, T.; Quignard, F.; Robitzer, M.; Guibal, E., Palladium supported on chitosan hollow fiber for nitrotoluene hydrogenation. *Journal of Membrane Science* **2009**, *329* (1-2), 30-45.

103. Chen, L. P.; Hong, S. G.; Zhou, X. P.; Zhou, Z. P.; Hou, H. Q., Novel Pd-carrying composite carbon nanofibers based on polyacrylonitrile as a catalyst for Sonogashira coupling reaction. *Catalysis Communications* **2008**, *9* (13), 2221-2225.
104. Yu, J. X.; Liu, T. Q., Preparation of a Fibrous Catalyst Containing Palladium Nanoparticles and Its Application in Hydrogenation of Olefins. *Polymer Composites* **2008**, *29* (12), 1346-1349.
105. Santhosh, P.; Manesh, K. M.; Uthayakumar, S.; Komathi, S.; Gopalan, A. I.; Lee, K. P., Fabrication of enzymatic glucose biosensor based on palladium nanoparticles dispersed onto poly(3,4-ethylenedioxythiophene) nanofibers. *Bioelectrochemistry* **2009**, *75* (1), 61-66.
106. Roy, P. S.; Bagchi, J.; Bhattacharya, S. K., Size-controlled synthesis and characterization of polyvinyl alcohol coated palladium nanoparticles. *Transition Metal Chemistry* **2009**, *34* (4), 447-453.
107. Xuyen, N. T.; Jeong, H. K.; Kim, G.; So, K. P.; An, K. H.; Lee, Y. H., Hydrolysis-induced immobilization of Pt(acac)<sub>2</sub> on polyimide-based carbon nanofiber mat and formation of Pt nanoparticles. *J Mater Chem* **2009**, *19* (9), 1283-1288.
108. Formo, E.; Lee, E.; Campbell, D.; Xia, Y. N., Functionalization of electrospun TiO<sub>2</sub> nanofibers with Pt nanoparticles and nanowires for catalytic applications. *Nano Letters* **2008**, *8* (2), 668-672.
109. Wang, H. Y.; Lu, X. F.; Zhao, Y. Y.; Wang, C., Preparation and characterization of ZnS : Cu/PVA composite nanofibers via electrospinning. *Materials Letters* **2006**, *60* (20), 2480-2484.
110. Kim, C.; Kim, Y. A.; Kim, J. H.; Kataoka, M.; Endo, M., Self-assembled palladium nanoparticles on carbon nanofibers. *Nanotechnology* **2008**, *19* (14).
111. Zhang, L.; Lee, K.; Zhang, J., The effect of heat treatment on nanoparticle size and ORR activity for carbon-supported Pd-Co alloy electrocatalysts. *Electrochimica Acta* **2007**, *52* (9), 3088-3094.
112. Lai, C.; Guo, Q. H.; Wu, X. F.; Reneker, D. H.; Hou, H., Growth of carbon nanostructures on carbonized electrospun nanofibers with palladium nanoparticles. *Nanotechnology* **2008**, *19* (19).
113. Huang, J. S.; Wang, D. W.; Hou, H. Q.; You, T. Y., Electrospun palladium nanoparticle-loaded carbon nanofibers and their electrocatalytic activities towards hydrogen peroxide and NADH. *Advanced Functional Materials* **2008**, *18* (3), 441-448.
114. Costamagna, P.; Srinivasan, S., Quantum jumps in the PEMFC science and technology from the 1960s to the year 2000 Part I. Fundamental scientific aspects. *J Power Sources* **2001**, *102* (1-2), 242-252.
115. Mehta, V.; Cooper, J. S., Review and analysis of PEM fuel cell design and manufacturing. *J Power Sources* **2003**, *114* (1), 32-53.

116. Whittingham, M. S.; Savinell, R. F.; Zawodzinski, T., Introduction: Batteries and fuel cells. *Chemical Reviews* **2004**, *104* (10), 4243-4244.
117. Weiner, S. A., Fuel cell stationary power business development. *J Power Sources* **1998**, *71* (1-2), 61-64.
118. Lloyd, A. C., The California fuel cell partnership: an avenue to clean air. *J Power Sources* **2000**, *86* (1-2), 57-60.
119. GM starts road testing of HydroGen4 in Berlin, Equinox in Japan. *Fuel Cells Bulletin* **2009**, *2009* (1), 2-2.
120. Frenette, G.; Forthoffer, D., Economic & commercial viability of hydrogen fuel cell vehicles from an automotive manufacturer perspective. *Int J Hydrogen Energ* **2009**, *34* (9), 3578-3588.
121. Ford's FCV fleet program extended after positive results. *Fuel Cells Bulletin* **2008**, *2008* (10), 4-4.
122. Bowers, B. J.; Zhao, J. L.; Ruffo, M.; Khan, R.; Dattatraya, D.; Dushman, N.; Beziat, J.-C.; Boudjemaa, F., Onboard fuel processor for PEM fuel cell vehicles. *Int J Hydrogen Energ* *32* (10-11), 1437-1442.
123. New Toyota FCHV-adv with enhanced stack, range. *Fuel Cells Bulletin* **2008**, *2008* (6), 1-1.
124. Litster, S.; McLean, G., PEM fuel cell electrodes. *J Power Sources* **2004**, *130* (1-2), 61-76.
125. Acres, G. J. K.; Frost, J. C.; Hards, G. A.; Potter, R. J.; Ralph, T. R.; Thompsett, D.; Burstein, G. T.; Hutchings, G. J., Electrocatalysts for fuel cells. *Catal Today* **1997**, *38* (4), 393-400.
126. Haug, A. T.; White, R. E.; Weidner, J. W.; Huang, W.; Shi, S.; Rana, N.; Grunow, S.; Stoner, T. C.; Kaloyeros, A. E., Using sputter deposition to increase CO tolerance in a proton-exchange membrane fuel cell. *J Electrochem Soc* **2002**, *149* (7), A868-A872.
127. Haug, A. T.; White, R. E.; Weidner, J. W.; Huang, W.; Shi, S.; Stoner, T.; Rana, N., Increasing proton exchange membrane fuel cell catalyst effectiveness through sputter deposition. *J Electrochem Soc* **2002**, *149* (3), A280-A287.
128. He, Z.; Chen, J.; Liu, D.; Tang, H.; Deng, W.; Kuang, Y., Deposition and electrocatalytic properties of platinum nanoparticles on carbon nanotubes for methanol electrooxidation. *Materials Chemistry and Physics* **2004**, *85* (2-3), 396-401.
129. Wang, M. Y.; Chen, J. H.; Fan, Z.; Tang, H.; Deng, G. H.; He, D. L.; Kuang, Y. F., Ethanol electro-oxidation with Pt and Pt-Ru catalysts supported on carbon nanotubes. *Carbon* **2004**, *42* (15), 3257-3260.

130. Male, K. B.; Hrapovic, S.; Liu, Y.; Wang, D.; Luong, J. H. T., Electrochemical detection of carbohydrates using copper nanoparticles and carbon nanotubes. *Analytica Chimica Acta* **2004**, *516* (1-2), 35-41.
131. Rodriguez, N. M.; Chambers, A.; Baker, R. T. K., Catalytic Engineering Of Carbon Nanostructures. *Langmuir* **1995**, *11* (10), 3862-3866.
132. Li, M.; Han, G.; Yang, B., Fabrication of the catalytic electrodes for methanol oxidation on electrospinning-derived carbon fibrous mats. *Electrochem Commun* **2008**, *10* (6), 880-883.
133. Lin, Z.; Ji, L.; Zhang, X., Electrodeposition of platinum nanoparticles onto carbon nanofibers for electrocatalytic oxidation of methanol. *Mater Lett In Press, Uncorrected Proof*.
134. Moghadam, S. S.; Bahrami, S. H., Copolymerization of acrylonitrile-acrylic acid in DMF-water mixture. *Iranian Polymer Journal* **2005**, *14* (12), 1032-1041.
135. Kwon, O. J.; Yoon, D. N., CLOSURE OF ISOLATED PORES IN LIQUID-PHASE SINTERING OF W-NI. *International Journal of Powder Metallurgy* **1981**, *17* (2), 127-&.
136. Brar, A. S.; Kumar, R., Sequence determination of N-vinyl-2-pyrrolidone/acrylonitrile copolymers by NMR spectroscopy. *European Polymer Journal* **2001**, *37* (9), 1827-1835.
137. Carrizales, C.; Pelfrey, S.; Rincon, R.; Eubanks, T. M.; Kuang, A. X.; McClure, M. J.; Bowlin, G. L.; Macossay, J., Thermal and mechanical properties of electrospun PMMA, PVC, Nylon 6, and Nylon 6,6. *Polym Advan Technol* **2008**, *19* (2), 124-130.
138. Ji, Y.; Li, C.; Wang, G.; Koo, J.; Ge, S.; Li, B.; Jiang, J.; Herzberg, B.; Klein, T.; Chen, S.; Sokolov, J. C.; Rafailovich, M. H., Confinement-induced super strong PS/MWNT composite nanofibers. *Epl* **2008**, *84* (5), 6.
139. Zussman, E.; Chen, X.; Ding, W.; Calabri, L.; Dikin, D. A.; Quintana, J. P.; Ruoff, R. S., Mechanical and structural characterization of electrospun PAN-derived carbon nanofibers. *Carbon* **2005**, *43* (10), 2175-2185.
140. Zhou, Z.; Lai, C.; Zhang, L.; Qian, Y.; Hou, H.; Reneker, D. H.; Fong, H., Development of carbon nanofibers from aligned electrospun polyacrylonitrile nanofiber bundles and characterization of their microstructural, electrical, and mechanical properties. *Polymer* **2009**, *50* (13), 2999-3006.
141. Chun, I. S.; Reneker, D. H.; Fong, H.; Fang, X. Y.; Deitzel, J.; Tan, N. B.; Kearns, K., Carbon nanofibers from polyacrylonitrile and mesophase pitch *Journal of Advanced Materials* **1999**, *31* (4), 36.
142. Kim, C.; Park, S. H.; Cho, J. K.; Lee, D. Y.; Park, T. J.; Lee, W. J.; Yang, K. S., Raman spectroscopic evaluation of polyacrylonitrile-based carbon nanofibers prepared by electrospinning. *J Raman Spectrosc* **2004**, *35* (11), 928-933.

143. Esrafilzadeh, D.; Morshed, M.; Tavanai, H., An investigation on the stabilization of special polyacrylonitrile nanofibers as carbon or activated carbon nanofiber precursor. *Synthetic Metals* **2009**, *159* (3-4), 267-272.
144. Fong, H.; Reneker, D. H. In *Investigation of the formation of carbon and graphite nanofiber from mesophase pitch nanofiber precursor*, Reneker, D. H.; Fong, H., Eds. 2006; pp 285-299.
145. **Kurpiewski, J. P.** Electrospun Carbon Nanofiber Electrodes Decorated with Palladium Metal Nanoparticles: Fabrication and Characterization. MASSACHUSETTS INSTITUTE OF TECHNOLOGY, Boston, 2005.
146. Doshi, J.; Reneker, D. H., Electrospinning Process and Applications of Electrospun Fibers. *Journal of Electrostatics* **1995**, *35* (2-3), 151-160.
147. Forzatti, P.; Lietti, L., Catalyst deactivation. *Catal Today* **1999**, *52* (2-3), 165-181.
148. Bartholomew, C. H., Mechanisms of catalyst deactivation. *Appl Catal a-Gen* **2001**, *212* (1-2), 17-60.
149. Hall, B. D.; Zanchet, D.; Ugarte, D., Estimating nanoparticle size from diffraction measurements. *Journal of Applied Crystallography* **2000**, *33* (6), 1335.
150. Lee, J. W.; Stein, G. D., Structure change with size of argon clusters formed in laval nozzle beams. *The Journal of Physical Chemistry* **2002**, *91* (10), 2450-2457.
151. Hasik, M.; Wenda, E.; Paluszkiwicz, C.; Bernasik, A.; Camra, J., Poly(o-methoxyaniline)-palladium systems: effect of preparation conditions on physico-chemical properties. *Synthetic Met* **2004**, *143* (3), 341-350.
152. Drelinkiewicz, A.; Hasik, M., 2-Ethyl-9,10-anthraquinone hydrogenation over Pd/polymers: Effect of polymers-Pd(II) chlorocomplexes interactions. *Journal of Molecular Catalysis A: Chemical* **2001**, *177* (1), 149-164.
153. Christodoulakis, K.; Palioura, D.; Anastasiadis, S.; Vamvakaki, M., Metal Nanocrystals Embedded within Polymeric Nanostructures: Effect of Polymer-Metal Compound Interactions. *Topics in Catalysis*.
154. Li, X.; Hao, X.; Na, H., Preparation of nanosilver particles into sulfonated poly(ether ether ketone) (S-PEEK) nanostructures by electrospinning. *Mater Lett* **2007**, *61* (2), 421-426.
155. Herberhold, M., *Metal Pi-complexes: Complexes with Mono-Olefinic Ligands*. Elsevier: Amsterdam, 1974; Vol. 2.
156. Bett, J.; Kinoshita, K.; Routsis, K.; Stonehart, P., A comparison of gas-phase and electrochemical measurements for chemisorbed carbon monoxide and hydrogen on platinum crystallites. *J Catal* **1973**, *29* (1), 160-168.

157. Baker, R. T. K.; France, J. A.; Rouse, L.; Waite, R. J., Catalytic oxidation of graphite by platinum and palladium. *J Catal* **1976**, *41* (1), 22-29.
158. Martin, N.; Fuentes, S., Characterization of palladium-graphite samples after gasification with oxygen. *Carbon* **1988**, *26* (6), 795-799.
159. Morrow, B. H.; Striolo, A., Morphology and diffusion mechanism of platinum nanoparticles on carbon nanotube bundles. *Journal of Physical Chemistry C* **2007**, *111* (48), 17905-17913.
160. Morrow, B. H.; Striolo, A., Platinum nanoparticles on carbonaceous materials: the effect of support geometry on nanoparticle mobility, morphology, and melting. *Nanotechnology* **2008**, *19* (19).
161. Wang, C.; Waje, M.; Wang, X.; Tang, J. M.; Haddon, R. C.; Yan, Y. S., Proton exchange membrane fuel cells with carbon nanotube based electrodes. *Nano Lett* **2004**, *4* (2), 345-348.
162. Hamann C, V. W., Hamnett A, *Electrochemistry*. Wiley-VCH: New York, 1998.
163. Vidakovic, T.; Christov, M.; Sundmacher, K. In *The use of CO stripping for in situ fuel cell catalyst characterization*, Cracow, POLAND, May 28-Jun 01; Cracow, POLAND, 2006; pp 5606-5613.
164. Gamburgzev, S.; Appleby, A. J., Recent progress in performance improvement of the proton exchange membrane fuel cell (PEMFC). *J Power Sources* **2002**, *107* (1), 5-12.
165. Qi, Z. G.; Kaufman, A., Low Pt loading high performance cathodes for PEM fuel cells. *J Power Sources* **2003**, *113* (1), 37-43.
166. Pattabiraman, R., Electrochemical investigations on carbon supported palladium catalysts. *Appl Catal a-Gen* **1997**, *153* (1-2), 9-20.
167. Moreira, J.; del Angel, P.; Ocampo, A. L.; Sebastian, P. J.; Montoya, J. A.; Castellanos, R. H. In *Synthesis, characterization and application of a Pd/Vulcan and Pd/C catalyst in a PEM fuel cell*, Cancun, Mexico, Aug 25-29; Cancun, Mexico, 2002; pp 915-920.